Investigating Non-Equilibrium Phenomena In Spinor Antiferromagnetic Bose-Einstein Condensates

A Thesis
Presented to
The Academic Faculty

by

Anshuman Vinit

In Partial Fulfillment
of the Requirements for the Degree
Doctor of Philosophy in the
School of Physics

Georgia Institute of Technology
August 2016

Investigating Non-Equilibrium Phenomena In Spinor Antiferromagnetic Bose-Einstein Condensates

Approved by:

Dr. Chandra Raman
School of Physics
Georgia Institute of Technology, Chair

Dr. Jason Amini
Georgia Tech Research Institute
Georgia Institute of Technology

Dr. Michael Chapman
School of Physics
Georgia Institute of Technology

Dr. Phillip First
School of Physics
Georgia Institute of Technology

Dr. Rick Trebino
School of Physics
Georgia Institute of Technology

Date Approved: August 17, 2015

DEDICATION

To my parents:

Sandhya and Vinay Lal

ACKNOWLEDGEMENTS

There are many people who I would like to thank for making this thesis possible. This acknowledgement is a small token of my appreciation for their supports.

First, I would like to thank my thesis advisor Professor Chandra Raman for not only providing me with opportunity to work in his laboratory, but also for sharing his knowledge and advice. He has been inspirational and instrumental in completion of this work. Throughout, I have appreciated his exceptional patience, humility and willingness to let me experiment with my ideas.

I would like to thank Dr Eva Bookjans for introducing me to the sodium Bose-Einstein condensate experiment. I am grateful for encouragement and approachability in early years of my graduate studies.

Dr Carlo Samson was a great colleague who brought his valuable experience to our laboratory. I wish him great success in his upcoming career in research.

Undergraduates Srivathsa Sridhar and Joshua Raimist undertook important projects in the lab. They have a very bright future, and I wish them all the very best.

I would also like to express my thankfulness to all my friends and family, who have been part of this journey. Friends Chingiz Kabytayev, Balachandra Suri, Keenan Zhuo, Martin Anquez, Lin Li, Jeff Tithof, Yuntao Li, Bradley Elkus, Shreevant Tiwari, Anirban Patra, Hrishikesh Rao, Jagan Padbidri, Prantih Kumar, Rajat Ghosh, Doga Murat Kurkcuoglu, Ravi Pallantala made my time at Georgia Tech a unique and unforgettable experience.

The school of physics has been a wonderful place for me to have a frequent discussion with other physicists, and learn the cutting-edge physics. I enormously enjoyed discussions with Dr Chris Hamley, Dr Michael DePalatis, Dr Thai Hoang, Dr Chung-Yu Shih, LTC Corey S Gerving from Professor Chapman's laboratory.

Before joining graduate school, Professors Uwe Sterr and Vasant Natarajan introduced me to the joys of doing experiments with cold atoms. Their encouragement motivated me

to explore a new physics without being afraid of a failure. I am grateful for their unwavering support.

Finally, and most importantly, I would like to thank my parents and sister for their constant support, which made me what I am today. I owe them so much. Their support, encouragement, patience and endless love have kept me feeling constantly on track in my Phd course. Without their devotion and love, this thesis would not have been accomplished.

TABLE OF CONTENTS

LIST OF FIGURES

CHAPTER I

INTRODUCTION

Phase transitions are ubiquitous in nature: the crystallization of water into snowflakes, the emergence of superconductivity in cooled metals, lipid layer formation in biological membranes, alignment of electron spins inside a ferromagnet are all examples involving phase transitions. The interest in classical phase transitions dates back over 140 years, when it was first discovered that vapor and liquid phases of carbon dioxide become indistinguishable at a certain temperature and pressure (1). This physical point was named as a critical point. Since then, this phenomenon has been studied across a wide variety of systems. It is well established that classical phase transitions are driven by thermodynamic fluctuations (2). The onset of this phase transition signals a reorganization of particles within the system. After a century of research, it is fair to say that the classical phenomenon is now rather well understood, even if new interesting transitions, e.g. in soft condensed matter, continue to be found.

Recent research in past few decades has revealed a new type of phase transition called a quantum phase transition, which is driven by quantum fluctuations associated with Heisenberg's uncertainty principle. The uncertainty principle states that the more certainty there is of a particle's position, the more uncertain its velocity will be. Thus even when thermal motion ceases at absolute zero temperature, quantum matter cannot be fully stationary, as this would fix its position and velocity simultaneously. These quantum fluctuations are also called zero-point motion. Contrary to classical phase transitions, quantum phase transitions can only be accessed by varying a physical parameter - such as a microwave field, magnetic field or pressure - at absolute zero temperature.

The quantum phase transitions can describe many-body systems whose ground state can be tuned through a point of non-analyticity (2). These are enormously revealing many-body events in nature because of their singular behavior. A rapid passage through the

critical point can quickly nucleate spatial inhomogeneities that subsequently evolve slowly with time. Such behavior typifies physical systems of vastly different microscopic origins, for example, rapid cooling of the early Universe following inflation (3; 4; 5), the chiral symmetry breaking phase transition in heavy-ion collisions (6; 7), and sudden cooling of solid-state magnets below the Curie temperature (8). The nature of the pattern formation is of fundamental interest to discover its universal features (9; 10). For example, the temporal evolution of correlation functions can yield critical exponents of the phase transition (11). Quantum gases offer the possibility of realization of these phase transitions in the laboratory, as well as enabling exploration of the dynamical evolution of the system state by directly controlling the tuning parameters.

Near a phase transition, system properties change extremely rapidly, such that at the thermodynamic limit, the transition point becomes a mathematical singularity. Yet all systems are finite and heterogeneous, and therefore true singularity is always suppressed in some way in the real world. In the domain of superfluids, the spectacular lambda point of liquid helium is smeared out by the earth's gravitation, requiring precise theoretical and experimental comparisons to be performed in space (12). However, for quantum gases the problem is even more severe, as the density variations are intrinsic, and must be accounted for in order to achieve quantitative agreement with a statistical description of the system (13; 14). Measuring the detailed behavior near a phase transition is important for revealing critical phenomena and universality, both of which are actively sought by these systems.

Quantum phase transitions are especially amenable to discovery and observation using ultracold atoms. A simple description is that a transition contains two competing terms which may be tuned relative to each other, with the critical point in the parameter space lying in the region where both terms contribute significantly. A classic example is the superfluid-Mott insulator transition in an optical lattice, where the ratio of interaction strength to tunneling, U/J, determines the transition point. By tuning U relative to J, one approaches the critical point, where the system ground state changes discontinuously (see (2) for a pedagogical description). Both U and J, however, are inhomogeneously distributed in space, resulting in a shell structure of different phases [14] and broadening of the transition

point. Thus it is widely believed that all, or almost all, of the phase transitions encountered in ultracold atomic systems necessarily suffer from this same type of problem.

This thesis discusses a remarkable exception that occurs in a spinor Bose-Einstein condensate. The transition we examine is between polar and anti-ferromagnetic spin states in an antiferromagnetic spin-1 BEC. It is not smeared out by density inhomogeneities, as the critical point is completely independent of density. Rather, the energy difference between the two competing states, which in turn is controlled by external fields using the quadratic Zeeman effect, sets the phase boundary. As a first-order quantum phase transition, it offers a unique perspective, as intrinsic inhomogeneity does not smear out the singular behavior discussed earlier. The spinor condensates possess a vector order parameter with additional degrees of freedom relevant to this problem.

Investigations of spinor Bose-Einstein condensates began with pioneering MIT experiments with sodium condensates confined in optical traps (15). In their studies, they observed spin-mixing of initially excited spin states (16) and studied the formation and dynamical evolution of spin domains in large extended condensates (17; 18; 19). From the component miscibility properties observed, it was determined that F=1 23Na condensates exhibit anti-ferromagnetic ordering of spins in low magnetic fields and thus sodium has a positive sign for the spinor dynamical evolution (16). Further investigations were performed on Rubidium (Rb), where the condensate was quenched across the quantum phase transition and subsequent dynamical evolution was observed. Similar work was performed with f=2 87Rb by the Hamburg group (20; 21), and with F=1 23Na by NIST group (22). Using large 87 Rb condensates in a quasi 2-D extended system, the Berkeley group observed spontaneous symmetry breaking across the phase transition in measurements of the transverse magnetization (23).

1.1 Contributions of this thesis

In this thesis we examine a first order quantum phase transition associated with quadratic energy shift which is an essential parameter in spinor physics. The spin-dependent Hamiltonian of $F = 1$ system in a mean-field representation is described as

$$H_{sp} = \frac{c_2}{2} n(\mathbf{r}) \langle \hat{\mathbf{F}} \rangle^2 + p(\mathbf{r}) \langle \hat{F}_z \rangle + q \langle \hat{F}_z^2 \rangle$$

where F and F_z are the vector spin-1 operator and its z projection respectively, n is the particle density, c_2 is the spin-dependent interaction coefficient, p is linear Zeeman energy and q is the energy difference $(E_{+1} + E_{-1} - E_0)/2$, where E_i is the energy of the atomic level for the spin $m_F = i$ component of $F = 1$. The spin-dependent interaction coefficient c_2 arises from spin-changing collisions that can convert two $m_F = 0$ atoms into an $m_F = \pm 1$ pair and vice-versa. It determines the nature of the ground state - antiferromagnetic for $c_2 > 0$ or ferromagnetic for $c_2 < 0$. In the absence of significant dipolar interaction term, such as in ^{23}Na, the above Hamiltonian is constrained by conservation of net angular momentum. The quadratic energy shift q is usually a function of external magnetic field B through the second-order Zeeman effect. However, it can also be tuned through application of microwave dressing field. The dressing field derives from the ac stark phenomenon which can shift the energy spectrum of an atomic system due to an oscillating electric field. This phenomenon is exploited to uncover polar to antiferromagnetic quantum phase transition in ^{23}Na spinor system.

Even though the levels shift independently in the presence of magnetic field, the linear energy shift can get cancelled due to spin conservation. Thus q plays an important role and the combination of c_2 and q realizes a rich phase diagram of possibilities. Various quantum phases and dynamics have been observed for both $c_2 > 0$ and $c_2 < 0$.

For an antiferromagnetic spinor BEC constrained to have zero net magnetization, the ground state solution is a nematic order parameter ϕ. It varies smoothly with q for all values except q = 0, which divides the phase diagram into two regions. For q > 0 the ground state is a polar condensate consisting of a single component - the $m_F = 0$ spin projection that minimizes $\hbar \langle \hat{F}_z^2 \rangle$. For q < 0 the ground state maximizes the same quantity

through a superposition of two components $m_F = \pm 1$, a so-called antiferromagnetic phase. The symmetry properties of the ground state therefore change discontinuously, defining a first order phase boundary. Exactly at the phase transition point the many-body ground state is a condensate of boson pairs forming a spin singlet state, and possessing super-Poissonian spin fluctuations. Near this boundary the mean-field wavefunction ϕ undergoes collapse and revival dynamics triggered by quantum fluctuations. Controllably accessing q = 0 would restore the full S^2 symmetry of the nematic order parameter, which has unusual topological defects such as half-quantum vortices. However, experimentally this requires low magnetic fields where spinor condensates are susceptible to ambient magnetic field noise that can mask interaction-related phenomena. In this thesis, we investigate the dynamical instability of an F = 1, $m_F = 0$ antiferromagnetic sodium BEC that is rapidly quenched across the boundary from q > 0 to q <0. The quadratic energy shift q was tuned by an additional microwave dressing field that allowed us to access the q < 0 regime. Microwave dressing of ferromagnetic ^{87}Rb has been used to tune spin mixing dynamics into the resonant regime in optical lattices (24) , and for the study of spontaneous magnetization (25). Unlike ferromagnetic systems, in antiferromagnetic condensates one generally expects unmagnetized domains to form as a result of $m_F = \pm 1$ pair production. The F = 1 spin system is intrinsically stable and amenable to studies of long time scale dynamics in the transition region. In the present work we observed evolution times ranging from 30 ms to over 2 seconds.

We compare our predictions with Bogoliubov theory as well as numerical simulations, finding good agreement in some, though not in all cases. In particular, the theory provides strong evidence for the spatially localized state for which homogeneous density profiles plays an important role. It also quantitatively accounts for the magnitude of the instability rate, shedding light on discrepancies that are observed in our experiment.

A key feature of this work is inclusion of magnetic field inhomogeneities that smooth the phase transition. Once these were removed, we observed a dramatic sharpening of the transition point, which could then be resolved within a quadratic Zeeman shift of only 1-2 Hz. We find contrary to intuition and to earlier observations of equilibrium properties in

the positive q region (16), that the field gradient suppresses the tendency for the $m_F = 0$ condensate to phase separate into an $m_F = \pm 1$ mixture. This suppression can be explained, however, by analyzing the unstable eigenmodes that are populated by the quench and uncovering, theoretically, their dependence upon p.

A central theme of our work is the use of dynamics to probe the phase transition through instabilties generated by a rapid quench. Simply by changing the quench parameters, we are able to map out the phase boundary. We do not need to probe the ground state of the system or wait for the equilibrium, as many early works on spinor gases have done. This greatly simplifies the experimental protocol, as the dynamics may be observed in the 10-100 ms, rather than 1-10 second range. We show that the rapid variation of the instability near the transition point can allow for a precise determination of the location.

In this thesis, we start with the description of the experimental set-up and procedure (chapter 2). Then we present the spinor Hamiltonian, Bogoliubov solution and the phase diagram for F=1 ^{23}Na condensate in chapter 3. In chapter 4, we discuss our technique of using a microwave dressing field to access the antiferromagnetic quantum phase transition. In chapter 5, we discuss the non-equilibrium behavior where both nematic and magnetic spin waves were generated, following the quantum quench. We also characterize the spatiotemporal evolution through two particle correlations between atoms in each pair of spin states. In chapter 6, we present our work on inclusion of magnetic field gradient in the spinor Hamiltonian and the sharpening of quantum phase transition curve following this inclusion.

CHAPTER II

EXPERIMENTAL APPARATUS

Bose-Einstein condensates were first realized in 1995 (26; 27; 28; 29) by evaporative cooling of an atomic cloud in a magnetic trap. Since then, this method which involves usage of a Zeeman slower, a magneto-optic trap and a magnetic trap has been replicated the world over. Our experimental configuration has been described in greater detail in the thesis of Dr Devang Naik (30). We have created sodium Bose-Einstein condensates in a large-volume optically plugged magnetic quadrupole trap (31; 32). The optical plug is realized through focusing an intense, blue-detuned laser beam which repels atoms from the coil center where the Majorana loss is significant.

The magnetic trap is, however, inherently unsuitable for spinor physics studies, as the atomic spin is frozen inside the trap. In the case of F=1 ^{23}Na, the magnetic trap is selective towards the $m_F = -1$ state. This limitation of the magnetic trap is overcome by introduction of an additional further step, to transfer the atoms to an optical dipole potential. The trapping potential of the optical dipole traps, unlike the magnetic traps, does not rely on the internal spin state of the atoms and the traps are essentially spin-independent under appropriate conditions. Therefore, they have the capability to trap atoms or molecules that are not susceptive to magnetic trapping, and are also well suited for studying internal dynamics, including spinor dynamics.

Our experimental procedure is almost identical to the one used in previous ^{23}Na BEC experiments performed in our lab, with the addition of the optical dipole trap. Our experiment commences by loading a large magneto-optic trap (MOT) through a Zeeman slower. After the magneto-optic trap stage, atoms are transferred into a magnetic quadrupole trap, where compression and decompression cycles rapidly reduce the phase space density. The ultracold cloud is finally transferred to an ODT, where the BEC is realized using evaporative cooling. We prepared BECs with up to 5×10^6 sodium atoms with a peak atomic

density $n_0 = 5.4 \times 10^{14} cm^{-3}$. The axial trapping frequency of the trap is 8Hz and the radial frequency is approximately 600Hz, creating a quasi-1D Bose-Einstein condensate.

2.1 Experimental Schematic

Figure 2.1 shows the top view of the basic schematic of the experimental apparatus, with the direction of gravity pointing into the page. Sodium atoms are trapped inside an ultra-high vacuum (UHV) chamber, which is designed to provide large optical access. The chamber is surrounded by optics which are used to direct and focus the laser beams. Sodium atoms are trapped within an optical dipole potential, created using a 1064 nm infrared (IR) laser. Near-resonant laser light for the magneto-optical trap (MOT) is beamed through different ports that intersect with the dipole trapping laser. The MOT beam axis, which is perpendicular to the page, is not shown. Slowing light points towards the sodium atomic beam inside the Zeeman slower. Two imaging lasers probe the condensate - one along the same axis as condensate and the other along a transverse axis to the condensate, on the same axis as MOT.

The UHV chamber has Helmholtz coils wrapped directly around it across three axes. These coils cancel out the earths magnetic field and apply magnetic bias fields. There are also two sets of gradient coils - one set is used to control the axial magnetic gradient applied to the condensate and the other set, which is placed above and below the chamber (not shown), is used for the Stern-Gerlach gradient and the magneto-optic trap gradient. The purpose of the Stern-Gerlach gradient is to separate the three spin states of the sodium condensate during imaging.

An antenna is placed inside the chamber, which serves the dual purpose of emitting both RF and microwave radiation, as required for the experiment. The size of the chamber viewports is smaller than the wavelength of the microwave rays, thus preventing microwave radiation from leaking out of the chamber.

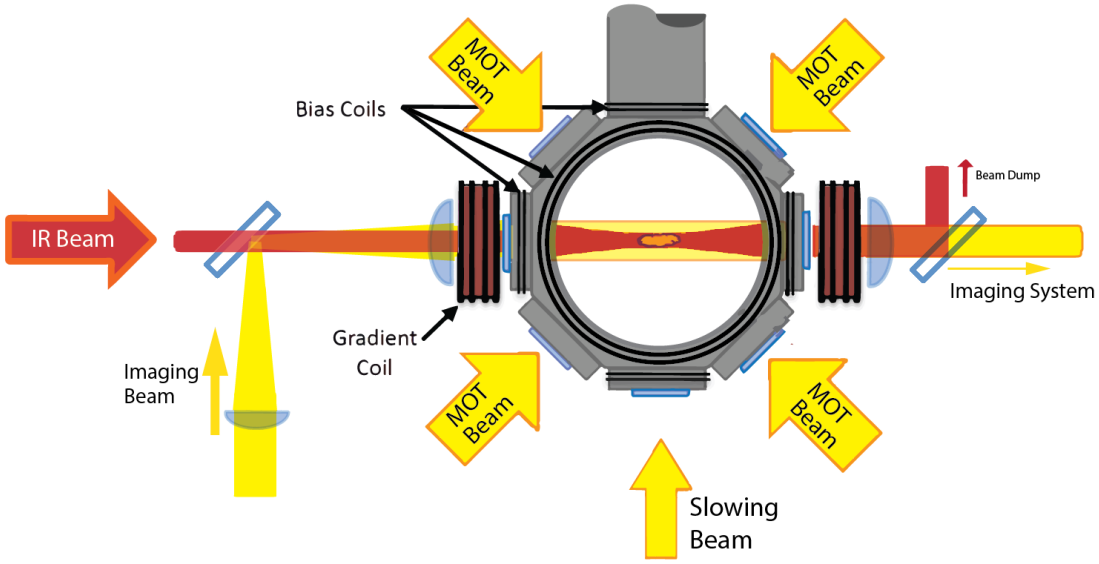

Figure 2.1: Schematic of the experimental set-up showing optical dipole trap, vacuum chamber and laser beams. 589 nm laser light is shown in yellow. 1064 nm infrared laser is shown in red. Atomic cloud is trapped at the focus of IR laser. Three pairs of bias coils are used to control magnetic field along three axes. A pair of gradient coil controls the axial magnetic field gradient. Axial image of the condensate is taken using the imaging system shown above.

2.2 Vacuum Chamber and Atom Source

The lifetime of a Bose-Einstein condensate is limited by its collisions with the background gas within the vacuum chamber. If atoms are depleted faster than the atomic cloud can rethermalize (i.e. atoms are lost before they can achieve the final Bose condensed state), then BEC cannot be reached. Therefore, in order to be able to produce a condensate, it is necessary to operate in an ultra-high vacuum environment to minimize collisions between the trapped atoms and the background gas. In this experiment, the pressure in the UHV chamber is maintained below 10^{-11} Torr, enabling a trap lifetime of 8 sec.

The source of the sodium atoms is an atomic beam oven. The oven consists of 50g of liquid sodium metal heated to 280°C. The vapor pressure of sodium atoms is 10^{-3} Torr. This chamber has a small 4 mm diameter aperture through which atoms effuse out into an atomic beam, with a most probable velocity of $v_p = 780ms^{-1}$.

The process is complicated by the fact that sodium atoms tend to stick to surfaces

colder than the surrounding region. Such clogging can prevent the formation of an atomic beam. This problem is overcome by keeping each section of the oven at a progressively higher temperature than the one before. This prevents sodium atoms from depositing in the path of atomic beam. The atomic oven is periodically loaded with 25g of ^{23}Na, which lasts about 500 experiment hours. Connected to the sodium oven is a high vacuum (HV) chamber maintained at a pressure of 10^{-8} torr. A gate valve and a differential pumping tube separate this from the ultra-high vacuum chamber where the atoms are trapped. The recent failure of this gate valve, owing to its end-of-life limitations, prompted us to install another gate valve in the vacuum chamber. The new gate valve (VatValve, 09136-UE01) was installed between the sodium oven and HV Chamber and protects the ultra-high vacuum section from pressure surges during occasional sodium oven changes.

2.3 Magneto-Optic Trap

Our experiments begin with loading sodium atoms from the Zeeman-slowed atomic beam into a standard magneto-optical trap (MOT). The MOT consists of three orthogonal pairs of counter-propagating circularly polarized laser beams and a pair of anti-Helmholtz coils (MOT coils). Figure 2.2 shows the detailed hyperfine structure of the sodium $3^2S_{1/2} \rightarrow 3^2P_{3/2}$ atomic transition. In order to achieve Doppler cooling, the cooling laser is detuned 15 MHz to the red of the $F = 2 \rightarrow F' = 3$ cyclic transition. However, there is a small but non-negligible probability of atoms getting off-resonantly excited to the $F' = 2$ state during this cooling transition, and decaying into the F=1 ground state. When this occurs, atoms in the F=1 state do not get trapped because they no longer interact with the cooling laser beams. In order to prevent this, a repump beam resonant with the $F = 1 \rightarrow F' = 2$ transition is applied. This laser light pumps any atoms in the F=1 state back into the cooling cycle, preventing a significant loss of atoms from the trap.

2.4 Lasers

The laser light used in the experiment was generated using a system composed of a laser diode, a Raman fiber amplifier, and second harmonic generation (SHG) modules. At

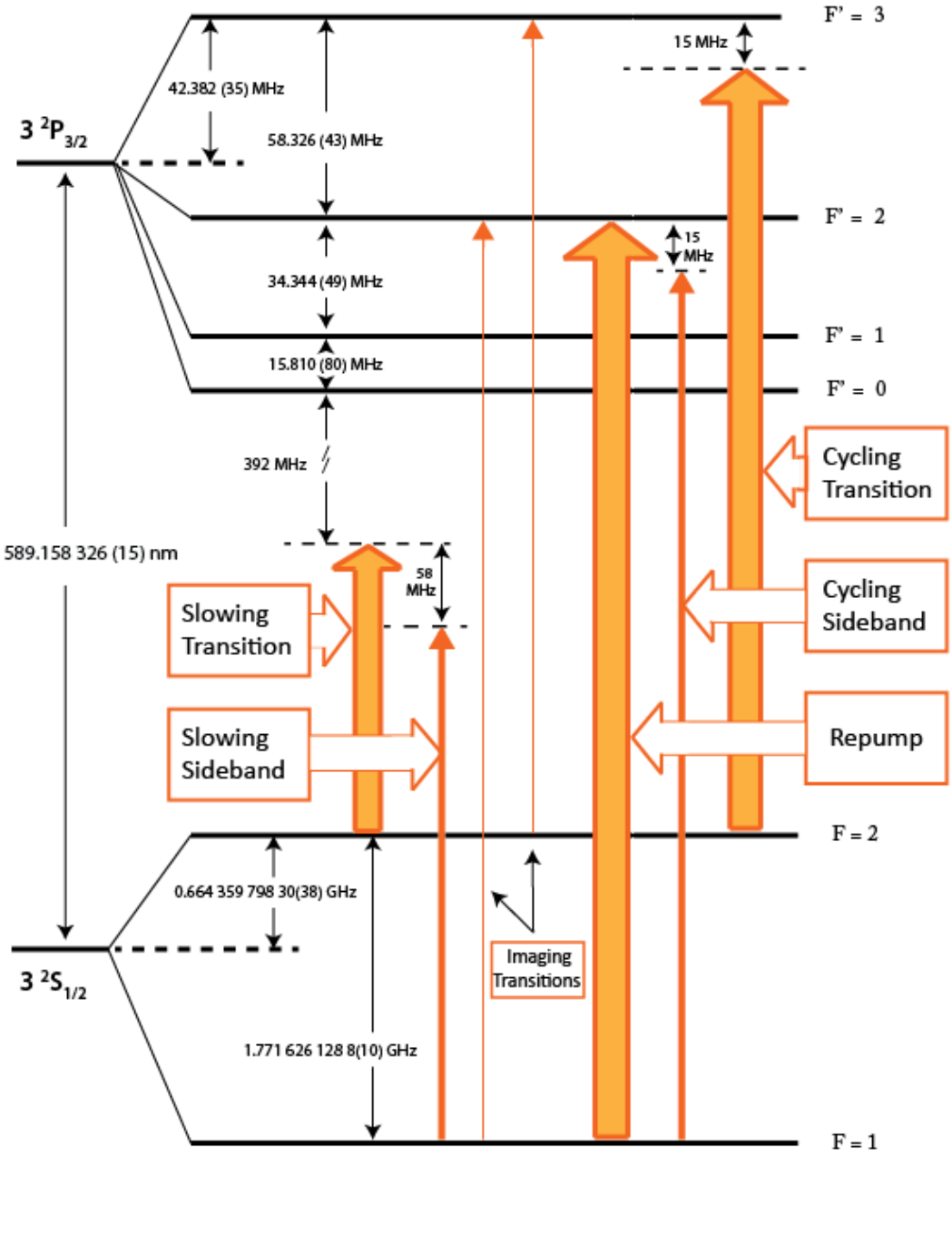

Figure 2.2: ^{23}Na D_2 transition hyperfine structure (33). The cycling transition and the cycling sideband are used to form the bright MOT. The cycling transition and the re-pump transition are used to form the dark SPOT MOT (34). The slowing transition and the slowing sideband are used for Doppler cooling sodium atomic beam in the Zeeman slower.

sodium's atomic transition wavelength of 589 nm, historically no semiconductor system was available. All ground breaking laser cooling experiments on the sodium atom since early 1970s relied on dye laser systems. In our laboratory, we used a dye laser system over the last decade. It was built by Coherent Inc and provided 1.3 W of laser light at 589 nm. A solid-state laser (Verdi V-10), emitting light at 532 nm, was used as a pump laser. However, a dye laser system is known to require daily calibration and frequent dye changes. Compared with a dye laser system, semiconductor laser systems are compact, reliable, inexpensive, and require less maintenance; as such it is preferred by researchers whenever it is available. Thus, the recent availability of laser diodes, Raman fiber amplifiers and second harmonic generation modules which enable laser light to be generated at sodium's wavelength of 589 nm is highly attractive for ultra-cold atom researchers. This laser system works by coupling 10 mW of seed laser beam emitted by a laser diode at wavelength of 1178 nm with 5 W of 1064 nm, pump laser beam generated by a ytterbium fiber laser to perform Raman fiber amplification. This output feeds into a second harmonic generating cavity which emits 2 W of laser light at 589 nm. The 1178 nm semiconductor diode system used in the experiment was sourced from Toptica Photonics [DL 100 Pro17321, Diode: LD-1200-0100-AR-1] and provides up to 85 mW of laser power. The linewidth is below 1 MHz and it features an integrated fiber dock through which the output is fiber coupled to a polarization maintaining fiber and sent to the RFA and SHG modules, which were provided by MPB Communications Inc [VRFA-P-1800-589-SF]. Both the Toptica and MPB systems are fairly turn-key and require little day-to-day tuning. The DL 100 Pro diode laser from Toptica features an array diode chip, a diffraction grating in Littrow configuration, beam-shaping optics, an integrated optical isolator and a fiber tuning dock. The DL 100 Pro system is fairly robust and is connected with Toptica's low-noise temperature and current controllers to ensure frequency stability and a mode-hop free tuning range of 30 GHz. In our experience, the only maintenance that this system has required is retuning of fiber dock every few months to ensure maximum output power.

For long-term frequency stability, the diode laser is locked to an atomic transition of ^{23}Na using frequency modulation (FM) spectroscopy on a saturated absorption signal.

Saturation spectroscopy setup and the resulting absorption and locking signals are shown in figure 2.3.

This non-linear spectroscopy technique uses a strong pump beam counter-propagating with a weak probe beam to counter the Doppler broadening of atomic absorption line. This method creates a narrow dip corresponding to each atomic transition in the Doppler broadened spectrum. This allows resolution of each atomic transition with significant accuracy. In addition to atomic transition peaks, this method also creates cross-over peaks which are halfway between each pair of atomic transitions. These cross-over peaks are usually larger in amplitude than the peaks of atomic transitions and can also be good locking points. Saturated-absorption spectroscopy is performed by modulating the laser wavelength with a small amplitude high-frequency signal. This is achieved in the semiconductor laser system by dithering the voltage across the diffraction grating of 1178 nm laser diode,with an ac signal of 156.25 kHz. In the dye laser system, the dithering signal is sent to the acousto-optic modulators(AOMs) shown in the figure 2.3. Near the atomic transition line, the FM causes a modulation of absorption signal, which gets detected by a photodiode. The first order term of the absorption signal is a DC term that corresponds to the absorption signal, and a term oscillating at the modulation frequency, the amplitude of which is proportional to the derivative of the absorption signal. The derivative of absorption signal is extracted by making a phase-sensitive detection relative to the modulating signal. The resulting error signal is fed to a lock-box that contains a proportional integral (PI) controller. For optimal frequency stability, the proportional output is fed back to the injection current of the diode for fast adjustments with a band width of up to 10 kHz, and the integrator output is fed back to the PZT to compensate for long-term drifts of the laser frequency. A schematic of the locking set-up is shown in figure 2.3.

An IR-Laser at 1064 nm is used to create the optical dipole trap used to trap the sodium atoms. The set-up for this IR laser is shown in figure 2.5. A 5 W laser from IPG Photonics (model: PYL-20-LP) is used to emit laser at the infrared wavelength. An AOM and a shutter are used as a switch. One of the telescopic lenses is mounted on a translation stage to enable a fine control of the location of the optical dipole trap. An imaging beam at 589

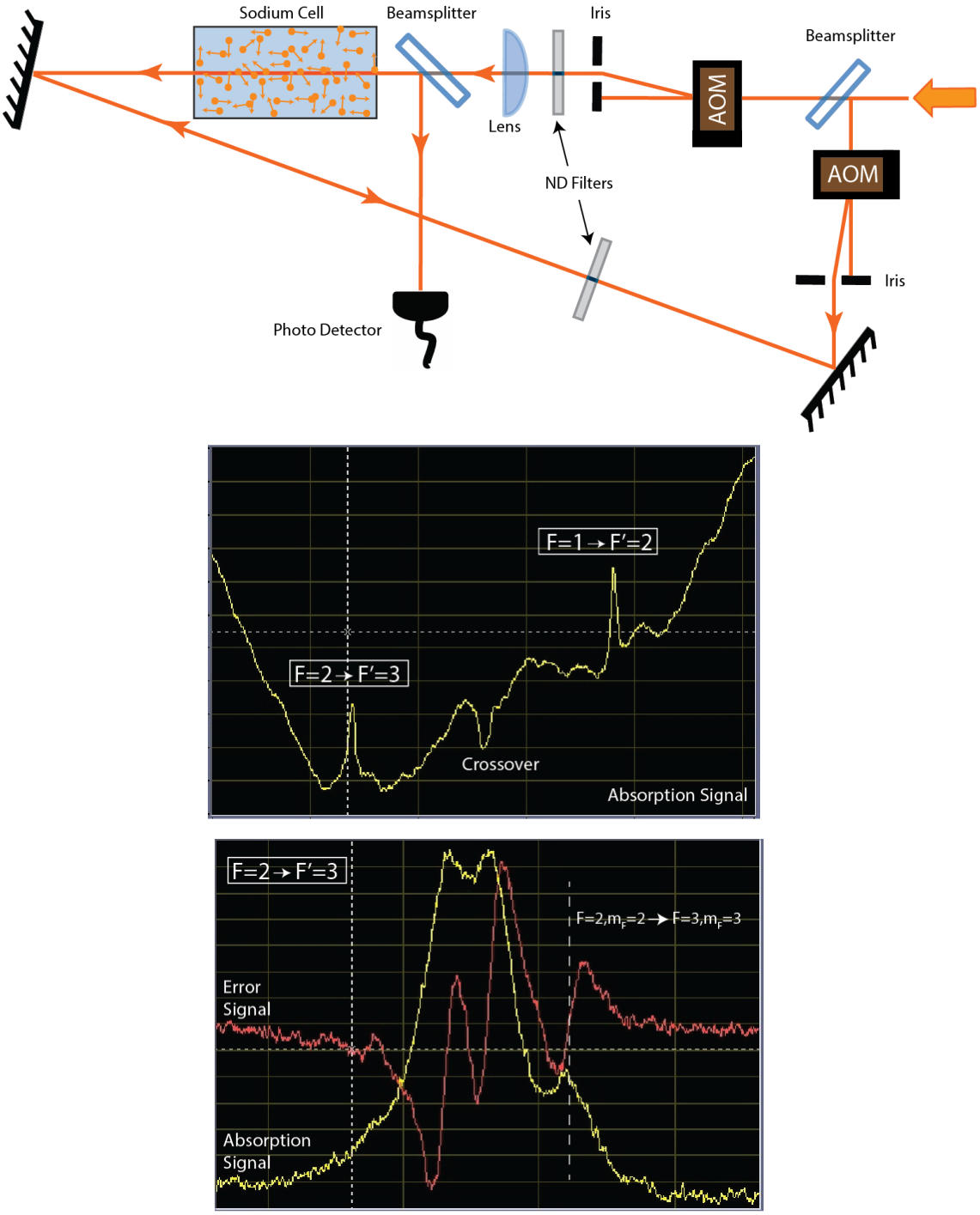

Figure 2.3: Saturation absorption spectroscopy set-up and spectra of the D_2 transitions. (a) A schematic of a typical saturation absorption spectroscopy set-up. (b) The spectra of the D_2 transitions of ^{23}Na. Crossover signal between the two signal (c) The saturated absorption (yellow line) and FM (red line) spectra of the $F = 2 \rightarrow F' = 3$ transition of ^{23}Na.

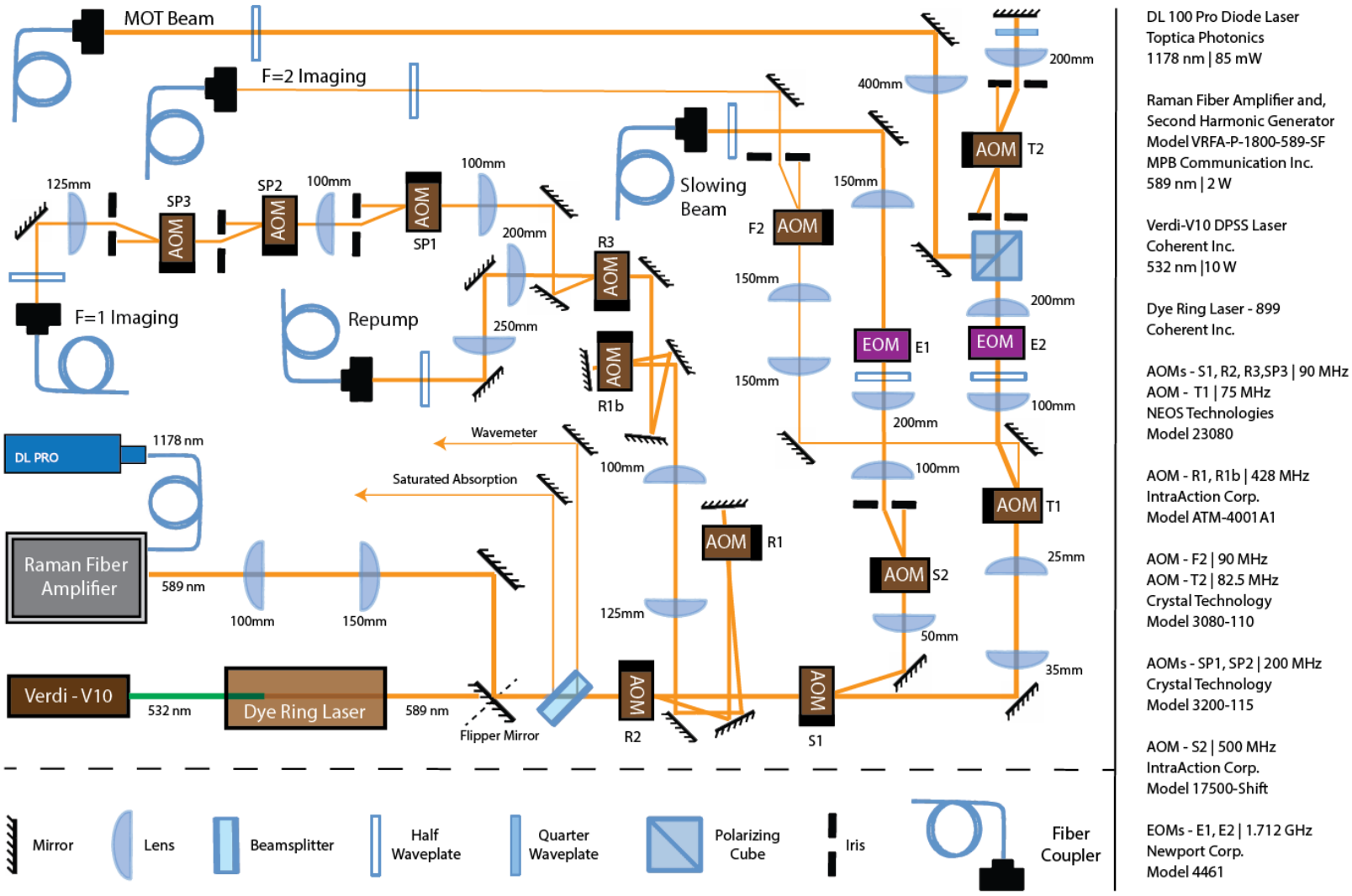

Figure 2.4: Schematic of the MOT laser set-up

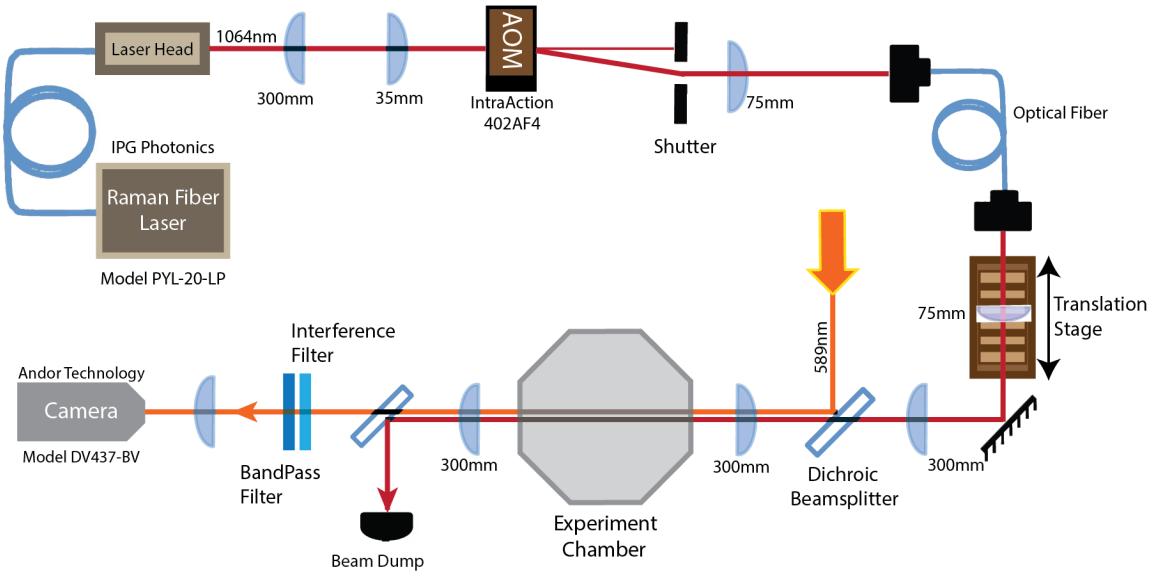

Figure 2.5: Schematic of the infrared optical setup

nm coincides with the IR laser and provides an axial image of the condensate. A dichroic beam splitter separates out the 1064 nm beam to enable acquisition of the final image.

2.5 Magnetic Coils

The magnetic field and field gradient were generated using three orthogonal pairs of Helmholtz coils (bias coils) and two pairs of anti-Helmholtz coils (gradient coils) respectively. The bias coils were used to cancel any ambient magnetic fields, such as the earth's field and any stray field generated by the laboratory equipment, and to apply an external magnetic field to the sodium condensate, as required during the experiment. These bias coils were made of copper wire, and were wrapped directly on to the vacuum chamber, in order to keep the experimental set-up compact and uncluttered. Due to this physical configuration, the bias coils were no longer in a perfect Helmholtz configuration. The gradient coils used for creating the MOT, were aligned in the direction of gravity. The second pair of gradient coils were aligned along the condensate axis and allowed control of the axial gradient as perceived by the quasi-1D BEC.

A magnetic field gradient was also used for Stern-Gerlach separation of the spinor condensate. When the IR laser dipole potential was turned off the condensate started falling under

the influence of gravity. During this period, the magnetic field gradient was pulsed on for a short duration, which separated the three Zeeman states physically, as the condensate fell under gravity. This Stern-Gerlach method permitted spatial separation of the spin populations and permitted studies of domain formation as well as measurement of individual spin populations.

The MOT gradient coils were made of copper refrigerator tubing, which were water cooled as they could get very hot ($\sim 100^oC$) when operated at full power without cooling. The coils were mounted as close to the chamber as possible and their inner diameters were configured to be larger than the respective viewports such that they did not reduce optical access to the chamber.

2.6 Microwave and RF Sources

The RF radiation was generated by a home made antenna placed inside the vacuum chamber. This antenna was a 2 loop circular coil of diameter 5.8 cm, consisting of copper wires. During evaporation, up to 7 W of RF power was broadcast through the antenna to the atoms. However, it was found that this antenna was potentially unsuitable for microwave radiation as it had unmatched impedance with the microwave circuit. This problem was solved by adding a stub to the microwave circuit, outside the vacuum chamber. A stub is a small reactive load that uses little or no power which is placed in parallel with the load in order to match the load impedance to the transmission line characteristic impedance. Its usage minimized the back-reflection of the microwave power and prevented over-heating and damage to the microwave circuitry as well as maximized the coupling the microwave antenna.

Figure 2.6 shows the dependence of the transmittance across a load on the length of stub placed parallel to the antenna. This simulation was done for an arbitrary microwave frequency. This plot demonstrates periodicity of the transmittance. It is clear that the maximum transmittance of 1 is possible only for very narrow range of stub length values. At these lengths, the impedance of the stub-antenna system perfectly matches the impedance of the transmission line, resulting in complete cancellation of the back-reflections.

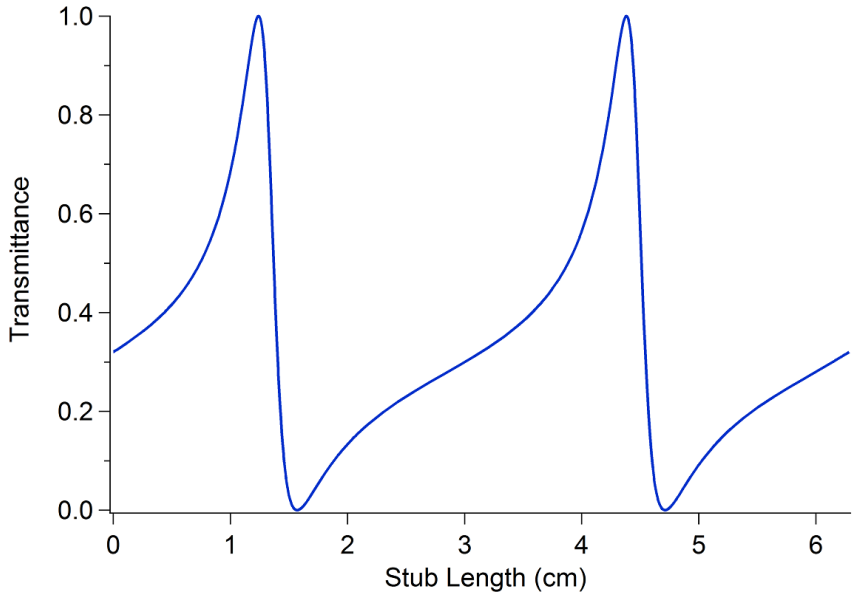

Figure 2.6: Figure showing trasmittance vs stub length for microwave power. Theoretical simulation was done to study the impedence matching for a microwave signal of arbitrary frequency

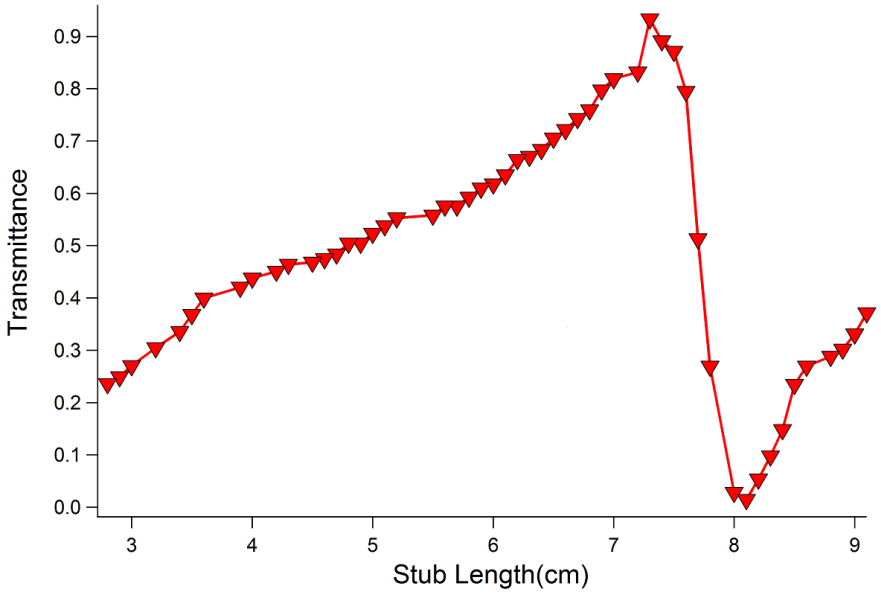

Figure 2.7: Figure showing transmittance achieved in the experiment by tuning the stub length.The stub length was kept close to its maximum transmittance value of 0.9.

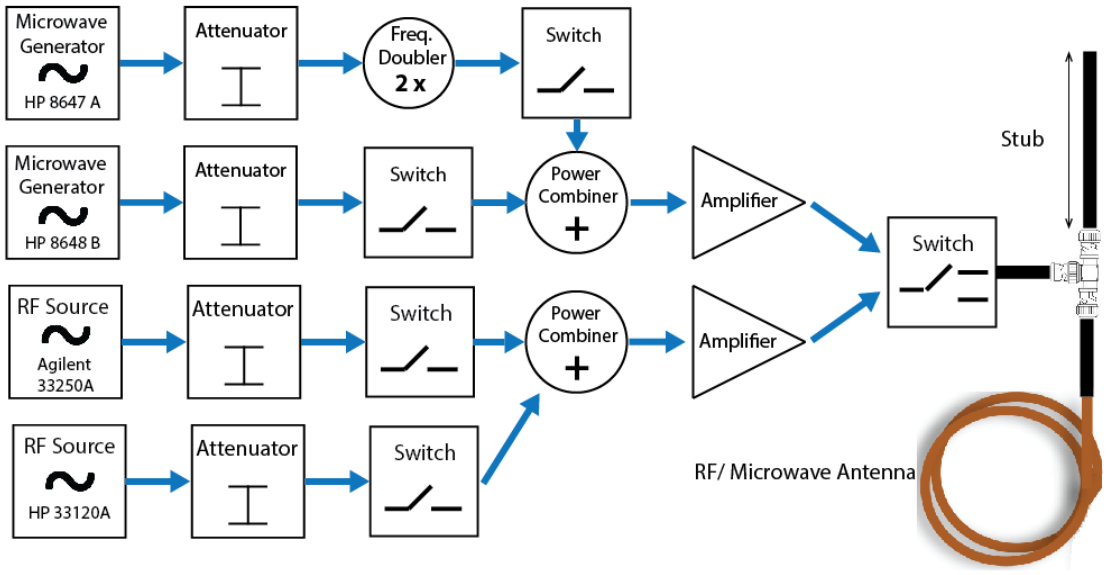

Figure 2.8: Schematic of the microwave set-up

Figure 2.7 shows the experimental transmittance observed across the load by varying the length of the stub. The microwave frequency is 1.771 GHz. This was measured by placing a circulator in the microwave circuit and measuring the back-reflections. The theoretical and experimental plots are qualitatively similar. The mismatch between the experiment and the theoretical plot arises due to different antenna impedence and microwave frequency values used in the two cases. In the experiment, we achieved over 90% transmittance, which allowed us to perform experiments which required a large amount of microwave power. Since our atoms are very close to the antenna, the microwave field appears as a near-field radiation source to the atoms.

The microwave radiation setup primarily consists of a frequency synthesizer (HP 8648B, 2 GHz), followed by an attenuator and an amplifier (Ophir RF, 5038BF) and a home made antenna. As it can take up to 500 ms to set the output of the frequency synthesizer using computer control, a second microwave source (HP8647A, 1 GHz) is used for the experiments where microwave radiation at two frequencies is required in rapid succession. The microwave radiation from the second source is doubled and passed through the Ophir Amplifier. In both cases, attenuators are used to provide protection. Selection between the two microwave sources is made using fast switches (Mini-Circuits ZYSWA-2-50DR) and a power combiner.

The RF radiation setup is similar to the microwave radiation setup. Agilent 33250A is the primary RF frequency generator and is used for RF-assisted evaporation. When a second RF source is required, a HP 33120 generator is used. Signals from both sources are sent to a power combiner followed by an amplifier (Delta RF, LA10-2-514-40).

2.7 Computer Control

Although much time has been spent describing the hardware required to make BECs, precisely timed electronic pulses are the key to the BEC apparatus. These pulses shift the frequency components of laser light (using acousto-optic and electro-optic modulators), open and close mechanical shutters, and turn on and off various MOSFET and IGBT switches for power supplies. It is through precise ordering and timing of these rather simple objects from which our BEC emerges.

Automation of this experimental sequence is performed using computer control by the National Instrument's PXI hardware and Aviv Keshet's Cicero software systems. The PXI hardware system has 16 analog output channels to control signals such as the bias and gradient coil currents, and the laser detuning and power. There are also 31 digital channels to control various RF and microwave switches, shutters and triggers for cameras and pulse generators. GPIB is used to update values for various microwave and RF generators. It is this complex control apparatus that allows flexibility and microsecond level precision across a variety of experiments that are performed.

To handle the timing, we inherited the cicero program developed by Aviv Keshet from MIT. This program utilizes the National Instrument DAQmx, VISA and 488.2 driver libraries in order to control the PXI equipment. A screenshot of the cicero software is shown in figure 2.10. The fairly intuitive user interface of cicero allows the user to set the digital output values at discrete time intervals of configurable duration (known as Words by the program). This software has two main applications for designing and running experimental control sequences. The first application, cicero, is a fairly intuitive user interface used for editing the sequences, which acts as a client to the second application - the server atticus. The atticus is the back-end (server) software which translates the sequences into output

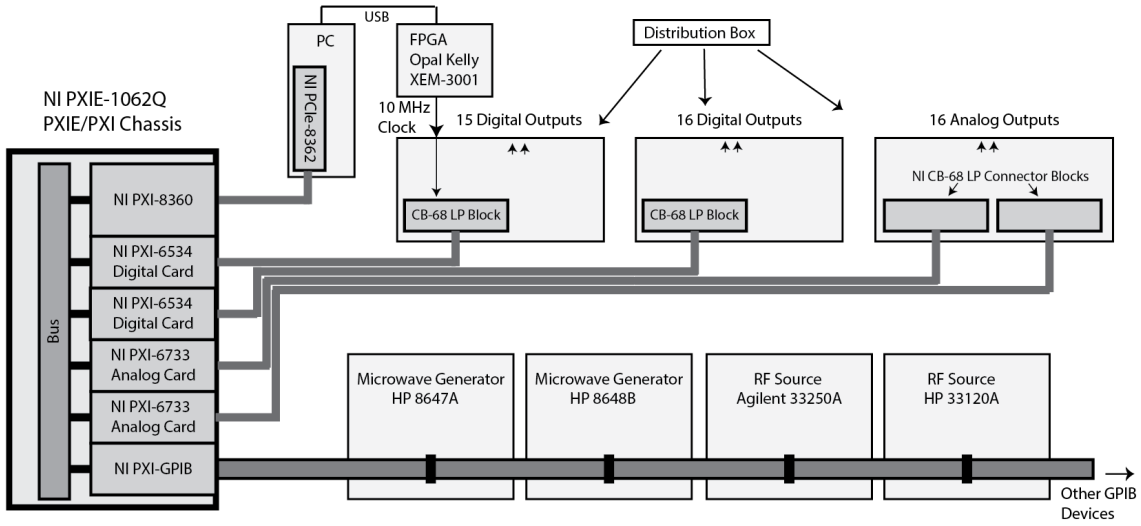

Figure 2.9: Layout of the Computer Control. On the left we have the PXI system provided by National Instruments.

buffers, and passes these output buffers to the output hardware. Full details of the software are available in this report (35). The timing is accurately controlled by a 10MHz clock signal provided by an FPGA (Opal Kelly XEM-3001). FPGA-based synthesis of the variable time-base facilitates much longer and higher resolution sequences. This method also has the advantage of completely freeing up the digital card, which was previously partially consumed by generation of the variable time-base. Each time an edge is received on the sample clock, the card processes the next sample in its buffer. These cards are capable of synthesizing their own sample clock at a wide range of fixed frequencies, by dividing down from an onboard master clock (usually running at 10MHz). NI cards on a single system share a common bus for communicating with other cards and sharing timing signals, in this case a PXI bus is used. The clock signal generated from the FPGA is loaded onto the PXI bus using one of the output connections of the PXI-6534 digital card. This connection is routed internally to the PFI channel on the card, where it gets loaded on the PXI bus and shared across all cards on the chassis.

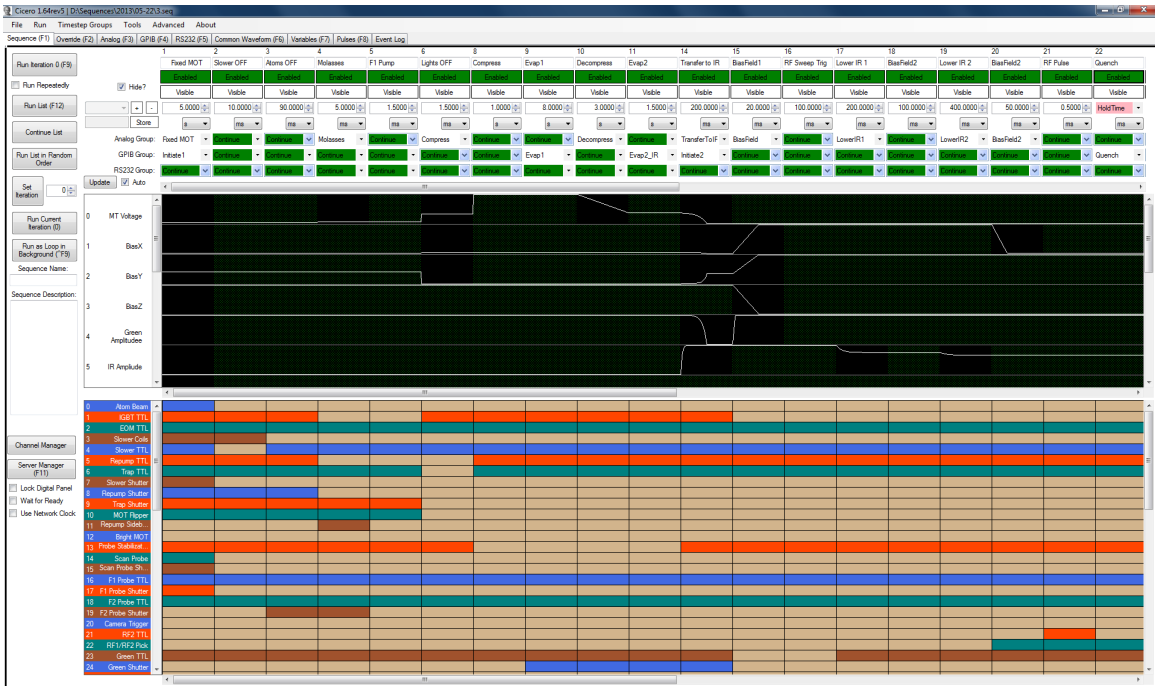

Figure 2.10: Screenshot of Cicero software

2.8 Imaging Setup

The imaging configuration used in the experiment is an absorptive imaging system with 2x magnification, as illustrated in figure 2.11 below. In this configuration, atoms are illuminated by a resonant laser beam and images of the shadow cast by the atoms are captured by a CCD camera.

The shadow propagates as a combination of modes taken from the initial probe beam. The final resolution of the imaging system depends on the number of modes that make it through the aperture of the first lens. Both the shadow modes and the probe beam are collimated by the first lens. The second lens re-collimates the probe beam to focus the shadow modes onto the CCD camera. The two lenses act together as a telescope for the probe beam and as an imaging lens for the shadow.

The image of the shadow of the atomic cloud is compared with a reference image of the probe light, taken without the atoms. This is used to determine the optical depth of the atomic cloud. The optical depth is indicative of the column density of the atoms. The number of atoms in the cloud is determined by calculating the sum of the column densities

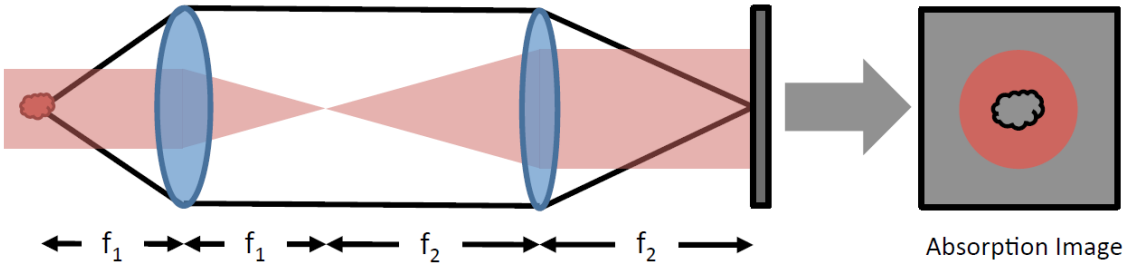

Figure 2.11: Schematic of imaging set-ups. (a) shows the imaging set-up used for the experiments described in chapter 5. The magnification can be changed by using different microscope objectives.

within the space.

Our imaging resolution achieved using the above setup was was 7.5 micron. This was determined by both the 6.6 micron camera pixel size and the blurring along the imaging axis due to the finite 300 micron radius of the expanded cloud. The latter imposed an effective resolution of 7.5 micron due to depth of focus considerations.

To get an accurate count of the number of atoms, it is crucial that the number of photons falling on the CCD camera be linearly dependent on the number of atoms in the cloud. This can be achieved only with lower atomic densities where the optical depth is less than two. This lower density is achieved through expansion of the atomic cloud as the atoms are allowed to fall under gravity (as described in an earlier section).

The absorptive imaging technique has a high spatial resolution because the atoms do not move much during the imaging process and only short pulses of light are needed. However, the use of laser light which has travelled through multiple optical elements usually results in some interference patterns which tend to affect the final image quality, particularly if the interference changes between the signal and reference shots.

Besides interference patterns, motion of the atoms introduces another source of error in our imaging system. In order to achieve a lower optical depth, the atomic cloud is allowed to fall under gravity. The atoms tend to recoil as they absorb the resonant photons. This heating of the atomic cloud due to the recoil-induced motion blurs the image signal and reduces the absorption signal by Doppler-shifting the atoms out of resonance.

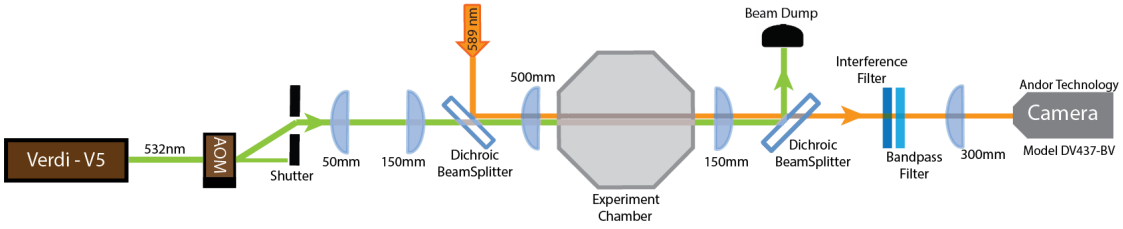

Figure 2.12: Schematic of the top imaging set-up. (a) shows the imaging set-up used for the experiments described in chapter 5. The magnification can be changed by using different microscope objectives.

In fact, the efficiency of absorption imaging is limited by the heating of the cloud. This limitation puts an upper bound on the probe time. For our experiment, we maintain the probe time below 100 microseconds.

The theoretical fundamental limit of detecting atoms using absorption imaging is set by the photon shot noise of the probe beam, or more precisely by the shot noise of the electrons that are counted by the camera as a result of the incident photons. In order to have shot noise limited absorption imaging, it is crucial to suppress the shot-to-shot variations in the probe beam intensity profile. Potential errors due to long term experimental drifts can be eliminated by taking the reference and the signal image in rapid succession. The time between the reference and signal is generally limited by the pixel readout of the camera. The first image has to be read by the camera before the second one can be taken. In this case, the time between images is around 200-300 ms. Experimental drift tends to have occurred between these two images, adding another source of imaging error.

The third source of error is the presence of diffracted rays in the system. Diffracted rays that are not collected by the imaging system will appear as false absorption signals. The magnitude of this effect depends on atomic density and therefore will vary across the cloud. As refraction is not uniform across the cloud, this affects both absolute and relative measurements of the atomic density across the cloud. In summary, dispersively dense atomic clouds will reduce the imaging resolution and can make it difficult to reliably determine the number of atoms.

CHAPTER III

SPIN-1 CONDENSATE THEORY

3.1 Introduction

Underlying the interesting dynamics of spinor BECs are the collisional interactions of the atoms. In a spinor BEC, the interplay between different atomic spin orientations results in a small spin dependence of the collisional interaction energy (36; 37). The spin dependence is small relative to the total interaction energy, and arises from the small difference in the s-wave scattering lengths of the allowed angular momentum channels (total spin F = 0, 2). This difference manifests itself as anti- or ferromagnetic properties for a spin-1 condensate, depending on the algebraic sign of the difference. The equilibrium state of the system is determined by the relative energies of the spinor energy and the per particle energy due to a finite magnetic field. For high magnetic fields the ground state is the $m_f = 0$ polar state, with the director aligned with the magnetic field. Lowering the magnetic field, the system undergoes a quantum phase transition where in the thermodynamic limit the ground state order parameter abruptly changes at a critical magnetic field and the sign of the spinor interaction energy determines the order parameter, ferromagnetic or anti-ferromagnetic for negative or positive spinor energy. For an anti-ferromagnet the critical field is q = 0.

3.2 Quantum Scattering

At the low densities of atomic gases, atomic interactions occur primarily due to two-body collisions. Even many-body systems can be well approximated through two-particle interactions. The binary collisions are characterized by a scattering matrix that relates outgoing asymptotic states with the incoming asymptotic state(38; 39). These states are products of atomic internal states and the orbital motion state. The orbital motion state can be specified in the spherical harmonic basis by the relative wave number k, and the quantum

numbers for the total orbital angular momentum L_{pair} and its projection on the quantization axis $m_{L,pair}$. The latter is used to specify the basis state of a spinor wavefunction. From energy conservation it is evident that the difference in kinetic energy of incoming and outgoing states in a binary collision, can result in changes in the internal spin state of the spinor system. For example, two spin zero atoms can collide and result in a spin +1 and a spin -1 atom with a different total internal energy. And, the difference in internal energy equates to change of the kinetic energy between the incoming and outgoing states. This is quantum spin mixing and forms the basis of dynamic studies performed in spinor systems.

However, the short-range potential can be more complicated as a large number of atomic phenomenon tend to affect this. For example, the short-range potential has contributions from individual interactions among all the constituent particles within the colliding atoms. This interaction also contains terms that mix the spin and orbital angular momenta of the colliding particles. Thus, in order to understand the quantum scattering due to the short-range potential, several approximations need to be made. The first assumption is that the incident collision energy is very low, and the the thermal de Broglie length of the relative motion of the atoms follows $\lambda_{dB} >> r_0$. This is the called the cold-collision approximation where only the lowest-order incident partial waves ($L_{pair,i} = 0$) is considered. Indeed, the lowest-order partial partial waves have lowest energy and this assumption is true under very cold systems. The contribution due to higher order partial waves is negligibly small for a cold gases and can be safely ignored.

The second assumption is the spinor gas collision which approximates that the short-range potential is rotationally invariant - such rotations affect both the internal spin degrees of freedom and also the orbital spatial degrees of freedom (36). This approximation is exact in the absence of any external source of rotational symmetry breaking such as applied magnetic fields, non-spherical trapping potentials, vector or tensor ac Stark shifts in the optical dipole force etc. However, in the real experiments this is rarely the case. Still, the spinor gas collision is accurate in the cases where the magnetic field strength is weak, and the system is in the normal Zeeman regime of the ground state hyperfine structure.

This approximation guarantees the conservation of the total angular momentum of the

colliding pair, which is the sum of the total orbital angular momentum L_{pair} and the internal angular momentum (nuclear and electronic) F_{pair}. By the cold-collision approximation, the total angular momentum of a colliding pair is F_{pair}. However, each source of angular momentum need not be separately conserved. For example, the dipolar relaxation can convert internal to orbital angular momentum. Only after all these approximations can we conclude that the collisions among spinor-gas atoms are characterized simply by the s-wave scattering lengths $a_{F;pair}$ between two particles in the collision channel F_{pair} (36; 37).

When two atoms with spin F approach each other, their spins ($|f_1 = f, m_{f1}\rangle$) and ($|f_2 = f, m_{f2}\rangle$) interact and temporarily couple to form the total hyperfine spin state $|F = m_F\rangle$. During the collision the two spins precess around the total spin $\vec{F} = \vec{f_1} + \vec{f_2}$ whose allowed values are $F = 2f, 2f-1, ..., 0$. As the spatial wavefunction of the two bosonic atoms is assumed to be symmetric, only the F=even scattering channels are permitted, while the F=odd channels are forbidden. After the collision, the two atoms decouple, and and break apart while the total angular momentum is conserved during the collision process. Hence, the two-body interaction potential can be understood as the sum of the contributions from the different spin F channels. For the spin-1 case, this is as given below

$$V_{int}(\vec{r}_1 - \vec{r}_2) = \delta(\vec{r}_1 - \vec{r}_2) \sum_{F=0}^{2} g_F \sum_{m_F=-F}^{F} |F, m_F\rangle\langle F, m_F| \tag{3.1}$$

where the coupling strength $g_F = \frac{4\pi\hbar^2}{M} a_F$, where a_F is the s-wave scattering length for the total spin-F channel, and M is the atomic mass. The closure and the symmetry requirement for the boson states that

$$\sum_{F=0}^{2} \sum_{m_F=-F}^{F} |F, m_F\rangle\langle F, m_F| = 1 \tag{3.2}$$

The s-wave scattering between two spin-1 bosons is characterized by the total spin of the two colliding bosons, 0 or 2, and we denote the corresponding scattering lengths by a_0 and a_2. The mean-field interaction energy can be written as $\int dr[c_0 n^2 + c_1 F^2]/2$, where the coefficients are given by

$$c_0 = \frac{4\pi\hbar^2}{M} \frac{a_0 + 2a_2}{3} \tag{3.3}$$

and

$$c_2 = \frac{4\pi\hbar^2}{M}\frac{a_2 - a_0}{3} \tag{3.4}$$

with M being the mass of the boson. The system is ferromagnetic if $c_2 < 0$, and antiferromagnetic is $c_2 > 0$. The density of particles is defined by

$$n = \sum_{m=-1}^{1} |\psi_m|^2 \tag{3.5}$$

and the components of the spin vector are given by $F_z = (F_+ + F_-)/2$, $F_y = (F_+ - F_-)/2i$ and

$$F_z = |\psi_1|^2 - |\psi_{-1}|^2 \tag{3.6}$$

with

$$F_+ = F_-^* = \sqrt{2}(\psi_1^*\psi_0 + \psi_0^*\psi_{-1}) \tag{3.7}$$

where ψ_m is the mean-field wave function for the magnetic sublevels m= $1, 0$, and -1. Since c_2 is negative for the spin-1 ^{87}Rb BEC, its ground state at a zero magnetic field is ferromagnetic.

The spin-dependent interaction c_2 couples the different Zeeman states, which leads to spinor dynamics, such as spin-mixing and spin domain formation. The sign of c_2 determines the ground state structure of the atoms. For $c_2 < 0$, the spin-dependent interaction potential is minimized for a maximum $\vec{f}_1.\vec{f}_2$. This is achieved when the spinors are all polarized in the same direction, and therefore an atom with $c_2 < 0$ is said to be ferromagnetic. In contrast, the ground state of an atom with $c_2 > 0$ requires the spinors to align in opposite directions. As a result, atoms with $c_2 > 0$ are said to be anti-ferromagnetic.

3.3 Quadratic Zeeman shift

The energy shift for the ground state manifold of the D transition is given by Breit-Rabi formula, which is valid both in low field and intermediate field case (40). This formula can be used to evaluate the small-field shift of the "clock transition" between the $m_F = 0$ sublevels of the two hyperfine ground states. These ground states do not have a first-order Zeeman shift. For alkali gases, the next-order term in the Zeeman shift by the Breit-Rabi

Hamiltonian. The quadratic energy shift is given by

$$\hat{H}_q = \mp \frac{(g_s \mu_B - g_I \mu_N)^2}{\Delta W (1+2I)^2} B_z^2 \hat{F}_z^2 = q \hat{F}_z^2$$

where $g_s = 2$ is the g-factor of the electron, $g_I \mu_N / \hbar$ is the nuclear gyromagnetic ratio, ΔW is the hyperfine energy splitting, B_z is the magnitude of the magnetic field, assumed to be oriented along z, and the hyperfine spin is $F = I \pm 1/2$.

A similar quadratic energy shift can also be obtained as an affect of oscillating electromagnetic field. For instance, a quadratic energy shift for the F = 1 spinor gas is obtained using the ac Zeeman effect from a microwave drive tuned near the $|F = 1; m_f = 0\rangle \rightarrow |F = 2; m_f = 0\rangle$ hyperfine transition(24). With this method, the sign of q can be varied by using either positive or negative detuning. Additionally, resonance linear polarized light will exert a quadratic shift the tensor portion of the ac Stark shift along the polarization axis. This optically induced shift can be spatially tailored at high resolution and rapidly adjusted using electro-optics. This shift gives a significant experimental handle on the ground state phase diagram of spinor Bose-Einstein condensates and on spin-mixing dynamics.

3.4 Spinor Hamiltonian

Gathering energy terms discussed in the previous sections, the total Hamiltonian of the spin-1 Bose gas is given by

$$\hat{H} = \int dr \sum_m \hat{\psi}_m^\dagger(r) \Big[-\frac{\hbar^2 \nabla^2}{2M} + U(r) \Big] \hat{\psi}_m(r) + \hat{H}_Z + \hat{V}_{int} \tag{3.8}$$

where U is the trapping potential, assumed to be scalar, and $\hat{H}_z$ describes the linear and quadratic magnetic field effects given by

$$\hat{H}_Z = \int dr \sum_{m_1 m_2} \hat{\psi}_{m_1}^\dagger(r) \Big[p \hat{F}_z + q \hat{F}_z^2 \Big]_{m_1, m_2} \hat{\psi}_{m_2}(r) \tag{3.9}$$

where we have assumed that the magnetic field is oriented uniformly along z, and that the quadratic Zeeman shift also selects the z axis.

In order to simplify the above Hamiltonian, we make the single-mode approximation that the wavefunctions ϕ_i $(i = 0, \pm)$ share the same spatial mode. This is valid when the

spin-dependent interaction is negligible compared to the density-dependent interaction i.e. $|c_2| \ll |c_0|$. In such a case we can decouple the spin and density dependent operators by making the approximation that $\hat{\psi}_m(r) = \phi(r)\hat{\psi}_m$, with $\phi(r)$ defining the spatial mode of the Bose-Einstein condensate. This approximation is clearly valid as long as the system's size is much smaller than the spin healing length ζ or, the energy cost of spatial variations in the spin state of the gas exceed any consequent reductions in the spin dependent energy. A condensate where the SMA is valid is consequently in the zero dimensional for the spin degrees of freedom. When the system's size is larger than ζ, the SMA may also be applied locally within the local density approximation. The ground states obtained under the SMA thus clarify how spin-dependent interactions can be locally minimized, even though the quantum gas has spin degrees of freedom.

Within the SMA, the spin-dependent part of the Hamiltonian for a spin-1 Bose gas reads as

$$\hat{H} = \frac{c_2 n}{2} \sum_{m_1,m_2,m_3,m_4} \hat{\psi}^\dagger_{m_1}\hat{\psi}^\dagger_{m_2}\boldsymbol{F}_{m_1m_3}.\boldsymbol{F}_{m_2m_4}\hat{\psi}_{m_3}\hat{\psi}_{m_4} + \sum_{m_1,m_2} \hat{\psi}^\dagger_{m_1}[pF_z + qF_z^2]_{m_1,m_2}\hat{\psi}_{m_2} \tag{3.10}$$

where $n = \int d^3\boldsymbol{r}|\phi^4|/\int d^3\boldsymbol{r}|\phi^2| \propto N$ is the average density proportional to the number of atoms in the gas N. If we ignore quantum fluctuations, and take expectation values with respect to the mean values of the mode operators, we obtain the mean-field energy functional

$$E = \frac{c_2 n}{2}\langle\hat{\boldsymbol{F}}^2\rangle + p\langle\hat{F}_z\rangle + q\langle\hat{F}_z^2\rangle \tag{3.11}$$

This, we get the Hamiltonian of the spin-1 BEC as

$$H_{sp} = \frac{c_2}{2}n(\mathbf{r})\langle\hat{\mathbf{F}}\rangle^2 + p(\mathbf{r})\langle\hat{F}_z\rangle + q\langle\hat{F}_z^2\rangle$$

where F, F_z are the vector spin-1 operator and its z-projection, respectively,n is the particle density, c_2 the spin-dependent interaction coefficient, p is linear Zeeman energy and q is the energy difference $(E_{+1} + E_{-1} - E_0)/2$, where E_i is the energy of the atomic level for the spin $m_F = i$ component of F = 1. The spin-dependent interaction coefficient c_2 arises from spin-changing collisions that can convert two $m_F = 0$ atoms into an $m_F = \pm 1$ pair and vice-versa. It determines the nature of the ground state - antiferromagnetic for $c_2 > 0$

or ferromagnetic for $c_2 < 0$. In the absence of significant dipolar interaction term, such as in ^{23}Na, the above Hamiltonian is constrained by conservation of net angular momentum. The quadratic energy shift q is usually a function of external magnetic field B through the second-order Zeeman effect. However, it can also be tuned through application of microwave dressing field. The dressing field derives from the ac stark phenomenon which can shift the energy spectrum of an atomic system due to an oscillating electric field. This phenomenon is exploited to uncover polar to antiferromagnetic quantum phase transition in ^{23}Na spinor system.

3.5 Bogoliubov Theory

In the presence of a magnetic field, the energy of an alkali atom is shifted, primarily due to the electron magnetic moment. We take this effect into account up to the second order in the magnetic field. The linear and quadratic Zeeman energies of the hyperfine spin f = 1 state are given by $p = \mu_B B/2$ and $q = \mu_B^2 B^2/(4\Delta_{hf})$, respectively, where μ_B is the Bohr magneton and Δ_{hf} is the hyperfine splitting. The multicomponent Gross-Pitaevskii (GP) equations are given by

$$i\hbar\frac{\partial\psi_0}{\partial t} = \Big(-\frac{\hbar^2}{2M}\bigtriangledown^2 + V\Big)\psi_0 + c_0 n\psi_0 + \frac{c_1}{\sqrt{2}}\Big(F_+\psi_1 + F_-\psi_{-1}\Big) \tag{3.12}$$

$$i\hbar\frac{\partial\psi_{\pm1}}{\partial t} = \Big(-\frac{\hbar^2}{2M}\bigtriangledown^2 + V \pm p + q\Big)\psi_{\pm1} + c_0 n\psi_{\pm1} + c_1\Big(\frac{1}{\sqrt{2}}F_\mp\psi_0 \pm F_z\psi_{\pm1}\Big) \tag{3.13}$$

In order to gain a better understanding of the mechanism of the formation of the magnetic domains, we perform a Bogoliubov analysis of our system (41; 42; 43). For simplicity, we assume a homogeneous system with a density of n0, and set the wave function as $\psi = e^{-i\mu t/\hbar}(\mathbf{\Psi} + \phi)$ with $\mu = c_0 n_0$ and $\mathbf{\Psi} = (0, \sqrt{n_0}, 0)$ where the three components refer respectively to the amplitudes of the $m = 1, 0, -1$ components. Substituting this into the last equation and keeping only the linear terms with respect to ϕ, we obtain

$$i\hbar\frac{\partial\phi_0}{\partial t} = -\frac{\hbar^2}{2M}\bigtriangledown^2\phi_0 + c_0 n_0(\phi_0 + \phi_0^*) \tag{3.14}$$

$$i\hbar\frac{\partial\phi_{\pm1}}{\partial t} = \Big(-\frac{\hbar^2}{2M}\bigtriangledown^2 + V \pm p + q\Big)\phi_{\pm1} + c_0 n\phi_{\pm1} + c_1\Big(\frac{1}{\sqrt{2}}F_\mp\phi_0 \pm F_z\phi_{\pm1}\Big) \tag{3.15}$$

We can solve these equations by expanding ϕ as

$$\phi(\boldsymbol{r},t)=\sum\left(\boldsymbol{u_k}e^{i(\boldsymbol{k}.\boldsymbol{r}-\omega_k t)}+\boldsymbol{v_k^*}e^{-i(\boldsymbol{k}.\boldsymbol{r}-\omega_k t)}\right) \tag{3.16}$$

Equation has the same form as the equation without the magnetic field, and the eigenenergy is given by

$$\hbar\omega_k^0=\sqrt{\epsilon_k(\epsilon_k+2c_0n_0)} \tag{3.17}$$

where $\epsilon_k=\hbar^2k^2/(2M)$. The corresponding Bogoliubov eigenvectors $\boldsymbol{u_k^0}$ and $\boldsymbol{v_k^0}$ are both proportional to (0,1,0), which describe the density modulation in the m=0 component. It follows from the above equation that if $c_0<0$, the eigenfrequency ω_k^0 becomes pure imaginary for long wavelengths, and the system collapses. Equation has two eigenfrequencies

$$\hbar\omega_k^{\pm}=\pm p+\sqrt{(\epsilon_k+q)(\epsilon_k+q+2c_2n_0)} \tag{3.18}$$

and the corresponding Bogoliubov eigenvectors take the forms

$$\boldsymbol{u_k^+}\propto(1,0,0),\quad \boldsymbol{v_k^+}\propto(0,0,1) \tag{3.19}$$

and

$$\boldsymbol{u_k^-}\propto(0,0,1),\quad \boldsymbol{v_k^-}\propto(1,0,0) \tag{3.20}$$

These two modes describe the spin waves that have spin angular momenta $\pm h$, and the energies are shifted by the linear Zeeman energies $\pm p$. The quadratic Zeeman term only shifts the single-particle energy from ϵ_k to ϵ_k+q. From Eq. (10), we find that the eigenfrequencies $\omega_k^{\pm}$ becomes pure imaginary if $q<0$ or $2c_2n_0+q<0$. Since, $c_2<0$ and $q>0$ for the case with the spin-1 ^{87}Rb BEC, the dynamical instabilities in the spin wave occur in a high-density region. In such a case, the modes become most unstable when the imaginary part of $\omega_k^{\pm}$ becomes maximal, i.e., at wave vectors that meet the following requirement:

$$\epsilon_k=max(0,-c_2n_0-q) \tag{3.21}$$

3.6 Mean Field Ground state

In the Hamiltonian discussed in the last section, the spin-dependent interaction term is rotationally symmetric. For $c_2 > 0$, as for the F=1 spinor gas of ^{23}Na, this term favors the polar states, for which the $|\langle \hat{\boldsymbol{F}} \rangle| = 0$. These interactions are denoted as "anti-ferromagnetic", although there is no Neel order in the traditional sense. For $c_2 < 0$, which is valid for the case of F=1 ^{87}Rb, this term favors ferromagnetic states, for which $|\langle \hat{\boldsymbol{F}} \rangle| = 1$. The application of external fields, described by the linear and quadratic Zeeman energies p and q, respectively, breaks the rotational symmetry.

The signature of antiferromagnetic interactions is the immiscibility of the $|m_f = 0\rangle$ and $|m_f = -1\rangle$ (or $|m_f = +1\rangle$) states, as first reported in the pioneering experiments performed in Ketterle group (**?** 18; 19). The immiscibility of the spin components was used to create metastable states and study quantum tunnelling (18; 19). This immiscibility results form the relation $a_{ij} > \sqrt{a_{ii} a_{jj}}$ between the self- and cross-scattering s-wave scattering lengths for two equal-mass distinguishable atomic states labeled i and j. For the F=1 spinor system, $a_{-1-1} = a_{0,-1} = a_2$ and $a_{00} = (2a_2 + a_0)/3$. For antiferromagnetic interactions, $a_0 > a_2$ and the immiscibility condition holds; in the diagrams for fig 3.1, this immiscibility is reflected in the sharp transitions between the $|m_z = \pm 1\rangle$ and $|m_z = 0\rangle$ phases (for q>0). Along the p = 0 axis, the antiferromagnetic F = 1 spinor condensate favors a polar ground state.

3.7 Phase Diagram

Even though the levels shift independently in the presence of magnetic field, the linear energy shift can get cancelled due to spin conservation. Thus q plays an important role and the combination of c_2 and q realizes a rich phase diagram of possibilities. Various quantum phases and dynamics have been observed for both $c_2 > 0$ and $c_2 < 0$. Figure 3.1 shows the phase diagram for a spin-1 Bose-Einstein condensate with $c_2 > 0$. The phase boundary of the polar phase resembles a parabolic shape in the phase space. The SO(2) rotational symmetry gets broken in the antiferromagnetic region. The yellow boundaries indicate a second order phase transition. However, at the phase transition point near p=0, where a transition from polar to antiferromagnetic phase takes place, the transition is first order.

The experiments performed in this thesis are near the p=0 region.

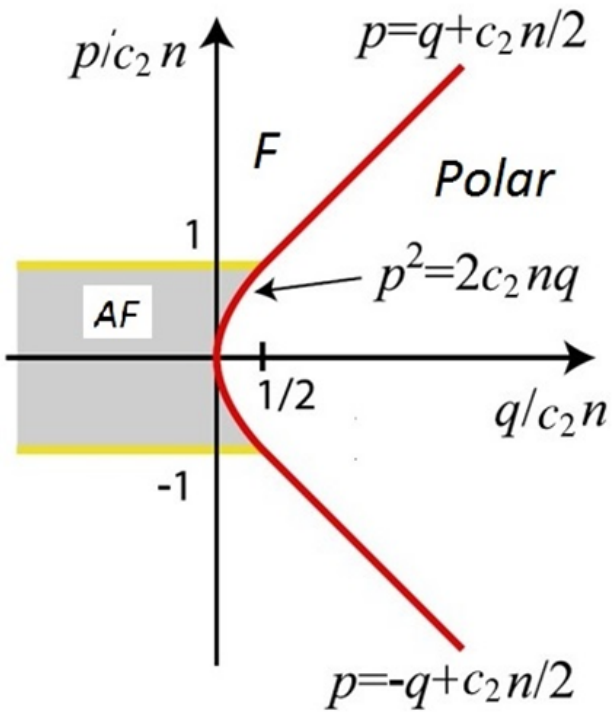

Figure 3.1: Phase diagrams of spin-1 Bose-Einstein condensates for $c_2 > 0$. AF denotes anti-ferromagnetic state. The SO(2) rotational symmetry about the magnetic field is broken in the shaded region. The yellow (light-colored) boundaries indicate second-order phase boundaries. The phase transition accessed in this thesis is at $p = 0$. Figure based on Kawaguchi et al. (44)

CHAPTER IV

ANTIFERROMAGNETIC QUANTUM PHASE TRANSITION

4.1 Introduction

Ultracold atomic physics has supplied us with a new family of fluids - degenerate Bose gases with a spin degree of freedom. Also known as spinor gases, these fluids lie at the intersection of magnetism and superfuidity. They have proven to be excellent testbeds to explore quantum phase coherence, long-range order and symmetry breaking. Moreover, these gases can be described from a simple theoretical framework, and since their properties may be readily manipulated and measured in experiments.

The relevance of such dynamics to topics such as quantum noise, quantum amplification, symmetry breaking and phase transitions has led to many studies of the spin mixing instability in both single-mode and spatially extended spinor Bose gases.

Underlying the interesting dynamics of spinor BECs are the collisional interactions of the atoms. In a spinor BEC, the interplay between different atomic spin orientations results in a small spin dependence of the collisional interaction energy. The spin dependence is small relative to the total interaction energy (e.g. $\approx 0.5\%$ in ^{87}Rb) and arises from the small difference in the s-wave scattering lengths of the allowed angular momentum channels (total spin F = 0; 2). This difference manifests itself as anti- or ferromagnetic properties for a spin-1 condensate, depending on the algebraic sign of the difference. The equilibrium state of the system is determined by the relative energies of the collective spinor energy and the per particle energy due to a finite magnetic field. For high magnetic fields the ground state is the $m_f = 0$ polar state having nematic ordering of the spins with the director aligned with the magnetic field. Lowering the magnetic field, the system undergoes a quantum phase transition where in the thermodynamic limit the ground state order parameter abruptly

changes at a critical magnetic field and the sign of the spinor interaction energy determines the preferred order parameter, ferromagnetic or anti-ferromagnetic for negative or positive spinor energy. For a ferromagnet, this critical field is given by $q = 2|c|$ where q is the quadratic Zeeman energy per atom and c is the mean-field spinor energy parameter to be defined later. For an anti-ferromagnet the critical field is q = 0.

One of the key consequences of the spin-dependent collisional interactions is that the spin components can coherently exchange population in a process known as spin-mixing. For example, two atoms with spin components $m_F = -1$ and $+1$ can collide and become two atoms with spin component $m_F = 0$ and vice-versa. This process is closely analogous to optical four-wave mixing, which is a third-order non-linear process involving four optical fields. This is central to much of the experimental and theoretical investigations of spin-1 condensates (and larger spin systems) and underlies most of the proposals for generating squeezing and entanglement in spinor condensates.

4.2 Methodology

Sodium BECs were created in an optical dipole trap created by single focused far-detuned 1064 nm laser beam as described in chapter 2. The atomic cloud had up to 3×10^6 sodium atoms and peak density was $n_0 = 5.4 \times 10^{14} cm^{-3}$. The axial trapping frequency was measured to be 8Hz which corresponded to Thomas-Fermi radii of $4\mu m$. The radial frequency was inferred to be 600Hz, which corresponded to the Thomas-Fermi radii of $270\mu m$. The condensate was initially prepared in the $m_F = -1$ state in a magnetic trap and transferred to an optical dipole trap as explained in earlier chapters. In order to create a pure $m_F = 0$ condensate in the optical dipole trap, the frequency of an RF magnetic field was adiabatically swept across the $m_F = 1$ and $m_F = 0$ transition at a bias magnetic field of 13 G (45). This bias field was then ramped to a final value of B= 97 mG in 30 ms, which was defined as the starting point (t = 0) of our experiment. At this magnetic field, the quadratic Zeeman shift is $q_B = h \times 2.5Hz$, which is far smaller than the spin-dependent interaction energy $c_2 n_0 = h \times 130Hz$. The spin healing length $\xi_s = \hbar/\sqrt{2Mc_2 n} = 1.3\mu m$. This length scale corresponds to the spinor interaction energy and was first defined in Stamper-Kurn thesis

(46). The spin healing length corresponds to a spin domain wall, and in this case is comparable to the the radial Thomas-Fermi radii of $4\mu m$. Thus the experiment was performed in a quasi-1D geometry, where only axial spin structures were expected.

4.3 Microwave Dressing Field

At the heart of our phase transition experiment is our ability to control the ground state of the spinor system using dressed fields. The fact that a strong radiation field can modify the atomic level structure has been well known in terms of effects such as the Bloch-Siegert shift or Autler-Townes doublet (47). In the phenomenon of dressed field states, the relative hyperfine energy levels are engineered using off-resonant radio frequency or microwave radiation. In this state, the bare atomic states get replaced by eigenstates of the total atom-plus-field system. The ability to control the spin dynamics in an ultracold system using microwave dressing field was first shown in the case of ^{87}Rb by Gerbier et al in 2006 (24). In our case the microwave field is relatively weak, such that the dressed states almost coincide with the bare atomic states and the level shifts can be calculated perturbatively. The dressed state energy shift for a hyperfine level in the presence of microwave dressing fields is given by

$$\delta E_m = \frac{\hbar \Omega^2}{4\delta} \tag{4.1}$$

where, Ω is Rabi frequency and δ is detuning from resonance. The energy levels can be shifted both up and down by controlling the polarity of detuning δ.

For weak magnetic fields, such as the one used in our case, the interaction with the zero-field eigenstates can be considered a perturbation. In this regime the energy levels split are given by

$$\Delta E_{|F,m_F\rangle} = \mu_B g_F m_F B \tag{4.2}$$

where μ_B is Bohr magneton, g_F is Lande factor and B is magnetic field. This splitting is linear and lies in anomalous Zeeman effect regime as shown in figure 4.1. The clock transition $|F = 1, m_F = 0\rangle \rightarrow |F = 2, m_F = 0\rangle$, however, does not show linear dependence on the magnetic field. The Breit-Rabi formula is used to determine the small-field shift

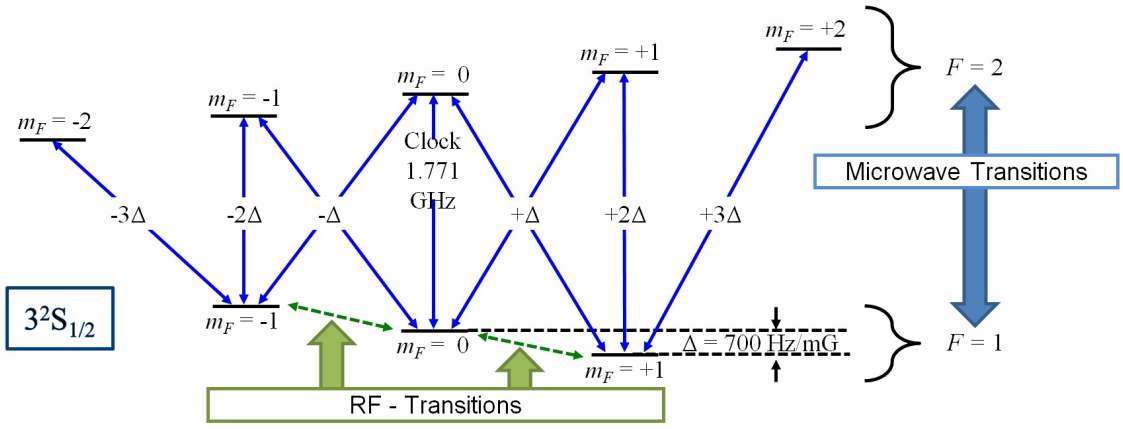

Figure 4.1: Structure of $3^3S_{1/2}$ state of ^{23}Na. Application of magnetic field lead to lifting of degeneracy of the Zeeman levels in F=1 and F=2 levels. An RF frequency sweep was used to transfer Na atoms from $|F = 1, m_F = -1\rangle$ state to $|F = 1, m_F = 0\rangle$ state. Atoms in F=1 state were imaged by exciting a small number of atoms to F=2 state using microwave pulses. An absorptive image of the atoms were subsequently taken in the F=2 level using the F=2 to F′=3 cycling transition of the D_2 line as described in chapter 2.

of the clock transition between the $m_F = 0$ sublevels of the two hyperfine ground states, which has no first-order Zeeman shift. This is given by

$$\delta\omega_{clock} = \frac{(g_J - g_I)^2\mu_B^2}{2\hbar\Delta E_{hfs}}B^2 \tag{4.3}$$

The microwave field was turned on at time $t = 0$. Figure 4.2 illustrates the microwave spectra associated with F=1 $\rightarrow$ F=2 transition. Turning on of microwave field took tens of microseconds and is shorter than any dynamical time scale relevant to the problem. The magnetic field value B was kept constant at 100 mG through the entire run, and the microwave power was swept between 0 and 7.5W. This tuned q from an initial value of q_B to a final value of $q = q_B + q_M = -18.5Hz$. At negative q, the dressing field created an instability in the initial $m_F = 0$ condensate. At each run, the condensate was held at a fixed value of q, and the hold time was varied. Thus, the temporal evolution of the system following the quench was studied.

The relative populations in the $m_F = 1; 0; -1$ states were determined by Stern- Gerlach time-of-flight images as illustrated in figure 4.3. In order to image the condensate, the trap was switched off and the atomic cloud was allowed to freely fall under gravity. After a time

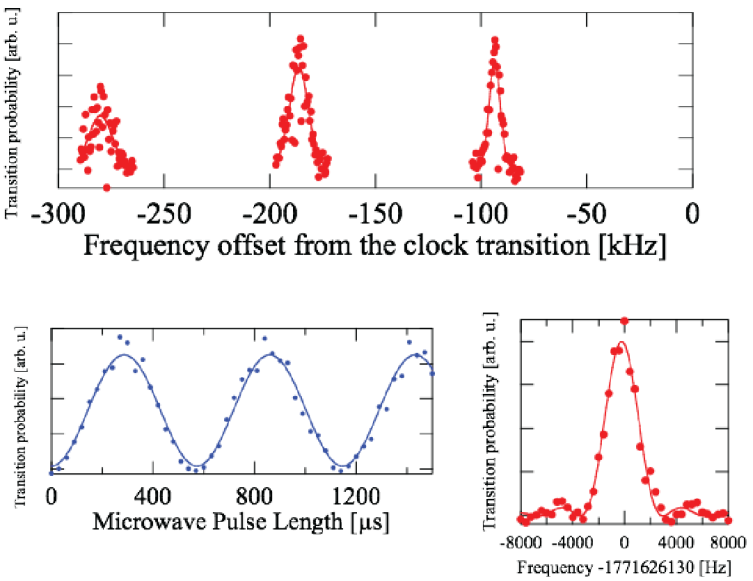

Figure 4.2: Microwave Spectra for F=1 to F=2 transitions a) Figure on top showing microwave transitions corresponding to $-\Delta$, -2Δ, and -3Δ where Δ is as shown in figure 4.1 b) Figure showing Rabi oscillations between the clock transition $|F = 1, m_F = 0\rangle \rightarrow |F = 2, m_F = 0\rangle$ c) Figure showing frequency spectrum for the clock transition corresponding to a rectangular microwave pulse.

of flight expansion of 3 - 3.5 ms, a Stern-Gerlach field gradient was pulsed on for a duration of 2 - 4.5 ms perpendicular to the axial direction of the condensate. This Stern-Gerlach field gradient separated the 3 spin components spatially. After a total time of flight of 25 ms, the atoms were optically pumped into the F=2 state and imaged on the $F = 2 \rightarrow F' = 3$ cycling transition ensuring an equal imaging sensitivity to each spin component.

The relative energy levels for three m_F levels are illustrated in figure 4.4. The quadratic energy shift q corresponds to the energy difference between $m_F = 0$ and $m_F = \pm 1$ energy levels. At low microwave power, the quadratic energy shift $q > 0$ and $m_F = 0$ is the ground state of the system. At $q = 0$, the two energy states become degenerate. The degeneracy gets lifted at $q < 0$, and $m_F = \pm 1$ is the new ground state of the system.

4.4 Results

Examples of the temporal evolution for $q = h \times -3.2$ Hz and $q = h \times -17.4$ Hz are shown in figs. 4.5(b) and 4.5(c), respectively. They indicate that a pure $m_F = 0$ condensate was unstable, evolving into a superposition of all 3 spinor components that preserved the overall

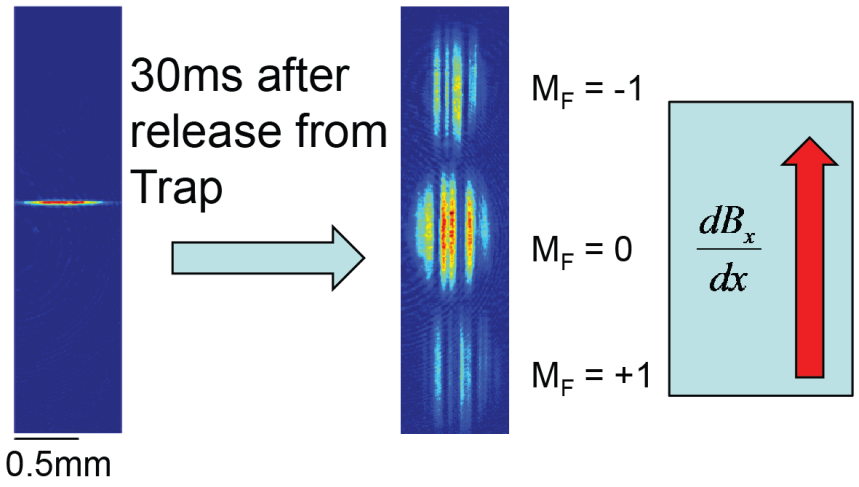

Figure 4.3: The relative populations in the $m_F = 1; 0; -1$ states were determined by Stern-Gerlach time-of-flight images. The trap was switched off and the atomic cloud was allowed to freely fall under gravity. After a time of flight expansion of 3 ms, a Stern-Gerlach field gradient was pulsed on for a duration of 2 ms perpendicular to the axial direction of the condensate. This separated the 3 spin components spatially. After a total time of flight of 25 ms, the atoms were optically pumped into the F=2 state and imaged on the $F = 2 \rightarrow F' = 3$ cycling transition as described in chapter 2.

zero net magnetization. In order to quantify the q dependence of the instability, data was fitted to a sigmoid function as shown in fig. 4.5 and the crossover time $T_{\frac{1}{2}}$ and the final saturation value $f_{0,min}$,where $f_0(T_{\frac{1}{2}}) = \frac{1}{2}(1 + f_{0,min})$, were evaluated. Here the measured instability rate was defined as $\Gamma(q) = 1/T_{1/2}$.

At zero microwave power, the quadratic energy shift was $q_B/(c_2 n_0) = 0.02$. Under these conditions, the gas was relatively stable against spin relaxation, i.e. the creation of $m_F = \pm 1$ pairs. This stability is a characteristic of quantum antiferromagnetism. For a homogeneous system and $0 < q < c_2 n$ the $m_F = 0$ state is stabilized against the creation of magnon excitations (spin waves) by an energy gap $\Delta = \sqrt{(\epsilon_k + q)(\epsilon_k + q + 2c_2 n)}$ where $\epsilon_k = \frac{\hbar^2 k^2}{2M}$. The $k = 0$ mode is the most unstable mode and for $q << c_2 n$, the energy gap $\sqrt{2qc_2 n} = h \times 25$ Hz for our parameters. As $q \rightarrow 0$, quantum fluctuations destabilize the pure $m_F = 0$ state: the fraction of atoms in the $m_F = \pm 1$ states should reach of order 1 within a time 1.5 seconds. This time scale is consistent with the slow rate of relaxation ($0.5 s^{-1}$) that we observed in our experiment (see Figure 4.5 a)). However, we cannot definitively

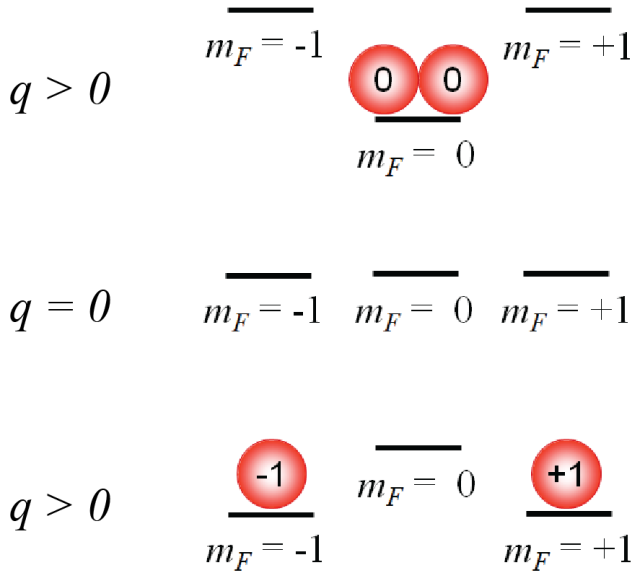

Figure 4.4: Relative energy level of the $|F = 1, m_F = 0\rangle$ and $|F = 1, m_F = \pm 1\rangle$ states under microwave dressing field. At low microwave power, quadratic energy $q > 0$ and $m_F = 0$ is the ground state of the system. At $q > 0$, the relative energy level inverts and $|F = 1, m_F = \pm 1\rangle$ is the ground state of the system.

rule out other mechanisms, including thermal fluctuations (our BEC had a thermal fraction of 40 percent) and imperfect transfer to the $m_F = 0$ state. For hold times longer than 2 seconds the cloud separated into two non-overlapping $m_F = \pm 1$ spin domains along the long axis of our trap, an indication that small residual magnetic field gradients might have been present.

For more negative q (figure 4.5c), however, the behavior was dramatically different as f_0 approached a final value of $f_{0,min} = 0.3$ within a time as little as 30 ms and remained roughly constant over 200 ms. We could not observe the gas for longer times due to losses caused by residual excitation to the $F = 2$ manifold at the microwave power and detuning used. Thus for the range of q explored in this work, the instability was observed to create a mixed state of all 3 components which appeared to be metastable on a timescale much longer than Γ^{-1}. When accounting for residual thermal atoms, the estimated condensate fraction $m_F = 0$ is slightly less than 0.3.

Figure 4.5 shows the final saturation value $f_{0,min(q)}$ plotted versus $\Gamma(q)$. These data provide further evidence for the two regimes mentioned earlier. Above a critical instability

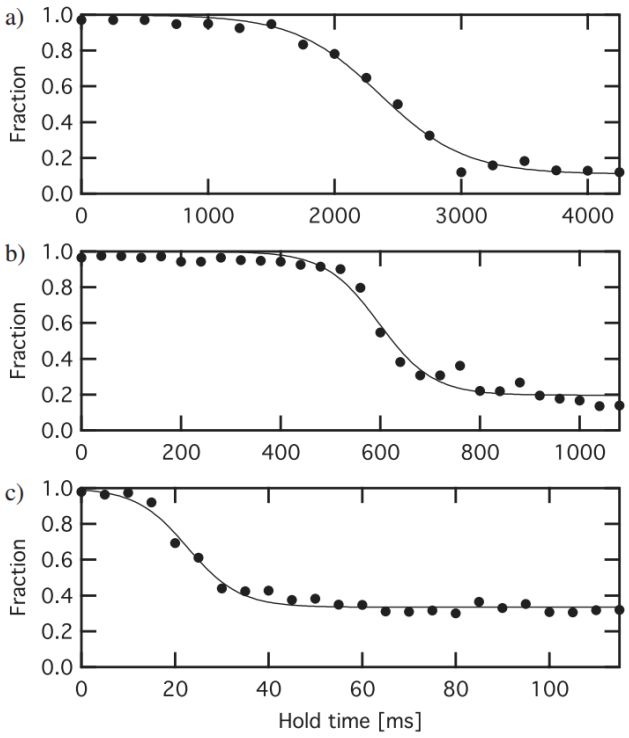

Figure 4.5: Quenching dynamics. For different final values of q,the $m_F = 0$ fraction (circles) is plotted versus time after the quench. The solid lines are fits of the $m_F = 0$ fraction to a Sigmoid function. In a) no microwave dressing field is applied. This data shows the relaxation in the absence of a quench ($q = h \times 2.5$ Hz). The equilibration to a pure $m_F = \pm 1$ cloud occurs after 2.1 s. In b) the gas is quenched to $q = h \times -3.2$ Hz,showing that the population decay is faster. In c) the gas is quenched to $q = h \times -17.4$ Hz and rapidly reaches a state containing all 3 spin components in roughly equal proportions

rate of $= 3\ s^{-1}$, the final fraction $f_{0,min}$ was between 0.2 and 0.3, and the $m_F = 0$ state maintained a significant presence in the cloud. With the exception of one data point, only for the very lowest instability rates $< 3s^{-1}$ was the steady state Bose-condensed spin distribution consistent with a pure $m_F = \pm 1$ spin mixture (open circles).

4.5 Quantum Rotor Model

The instability can be qualitatively understood in terms of the quantum rotor model. The spinor Hamiltonian can be mapped to a quantum rotor Hamiltonian

$$H = \frac{L^2}{2I} + V(\theta) \tag{4.4}$$

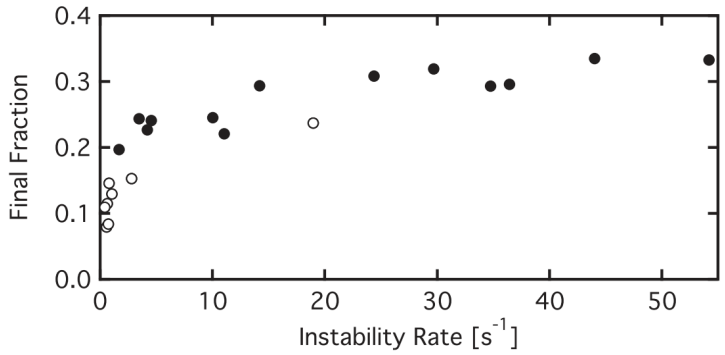

Figure 4.6: Final $m_F = 0$ fraction versus instability rate Γ. The open circles indicate data for which the final $m_F = 0$ distribution consisted purely of thermal atoms.

where L is the angular momentum of the rotor, $I = \frac{N\hbar^2}{g}$ is the moment of inertia, and $V(\theta) = q(N + \frac{3}{2})sin^2(2\theta) + \frac{q^2N}{8g}sin^2(2\theta)$ is the external potential. The quantum rotor model is valid in single mode approximation and cannot describe spin domain formation. Hence, the quantum rotor model cannot explain data for small $|q|$, for which spin segregation occurs. However, the model can be used to understood the behavior for short time scales following the quench for larger $|q|$, where a mixture of 3 components is observed to occur. A pure $m_F = 0$ state is represented by $\theta = 0$ in the quantum rotor model, while $0 < \theta < \pi$ represents a state where a fraction of the atoms are in $m_F = \pm 1$ state. The sudden quench transition from $q > 0$ to $q < 0$ causes V to change sign, resulting in rapid dispersion of a wavepacket initially highly localized in angle near $\theta = 0$. The resulting wavepacket dynamics are mostly classical in character and consist of a rapid dispersion in θ followed by sparse, periodic revivals at time t_{rev} (48) . For our parameters $t_{rev} \sim 350$ seconds, considerably longer than our observation time. For short times, as in figure 4.7, we observed only the rapid dispersion phase, and we interpret the measured value of ≈ 0.3 for each spin component to be the result of wavepacket dispersion that tends to equalize the spin populations.

4.6 Discussion

The measured instability rate Γ has been plotted versus the final quadratic energy $q = q_B + q_M$ in figure 4.7 for q ranging from +2.5 Hz to −18.5 Hz. The data shows a steep rise in the pair formation rate by a factor of nearly 100 as $\frac{q}{c_2 n_0}$ varied from +0.02 to 0.15, indicating

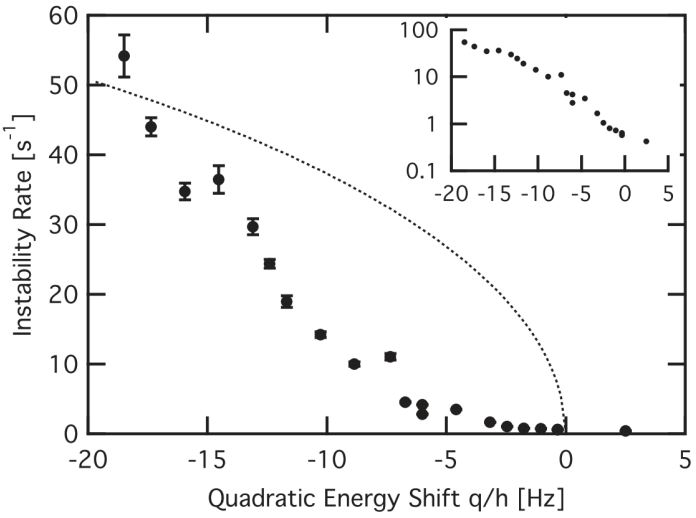

Figure 4.7: Quenching through the quantum phase transition. The formation rate of $m_F = \pm 1$ atom pairs is plotted versus the quadratic energy shift q (circles) determined by fitting the temporal evolution of the $m_F = 0$ fraction to a Sigmoid function. The error bars give the statistical uncertainty in the fit. The instability rate dramatically increases below the transition point at q = 0. Also shown (dotted line) is the predicted instability rate from Bogoliubov theory for a uniform gas. Inset shows the same data plotted on a semilog scale.

that we had crossed a phase boundary in the dynamical evolution of the system. Figure 4.7 also shows the predicted maximal instability rate for $-c_2 n_0 < q < 0$ from Bogoliubov theory for a uniform $m_F = 0$ gas with the same average density $\angle n\rangle$, $\Gamma_{unif} = \sqrt{|q|(q + 2c_2\langle n\rangle)}$. This corresponds to the formation of correlated pairs of atoms in a spatial mode with wavevector $k = 0$, i.e. a homogeneous rate of pair formation throughout the cloud [24]. The homogeneous theory is in considerable disagreement with our data, which could be attributed to the presence of uncompensated field gradients as discussed in chapter 6 of this thesis. Earlier work on pair formation dynamics in F = 2 spinor condensates highlighted resonant structures and the importance of the inhomogeneous density profile in determining the modes that were populated. No clear indication of resonances were visible in our data. Moreover, this theory does not account for possible spin exchange processes between the condensate and the residual thermal cloud, which could play a role in our observations.

4.7 Domain Formation

In order to gain an intuitive understanding of the spatial dynamics one can think of the inhomogeneous $m_F = 0$ condensate as a locally varying gain medium for the pair formation instability. For very short times after the quench, depletion of the gain can be neglected, and one may write the growth rate of $m_F = \pm 1$ atom pair number for $q < 0$ using a local density approximation as $\Gamma_{local} = \sqrt{|q|(q + 2c_2\langle n \rangle)}$, where $n(\overrightarrow{r})$ is the spatial density profile of the $m_F = 0$ cloud with the maximum gain occurring at the cloud center. In this regime, the inhomogeneous gain acts as a nonlinear spatial mode coupler that converts energy from long to short wavelengths, i.e. exhibits a tendency to nucleate small sized domains. These dynamics are not captured in the homogeneous theory, but appear in our data. For data sets with $q < h \times -7$ Hz, the $m_F = \pm 1$ atom distribution appeared initially as one or more small axial domains near the cloud center. As an example, figure 4.8a)-e) show Stern-Gerlach images at various times after the quench for $q = h \times 17.4$ Hz. These domains appeared to coalesce into a larger domain that grew in size with time until it became comparable to the axial Thomas-Fermi radius (see figure 4.8).

Once a substantial number of atom pairs have been created the $m_F = 0$ condensate can be locally depleted (see for example figure 4.8). Since the $m_F = \pm 1$ and $m_F = 0$ clouds are immiscible for $c_2 > 0$, this creates a potential well that traps the pairs but allows the domain to grow axially due to the continued effect of the instability (expansion along the radial direction costs a substantial kinetic energy due to the tighter confinement). Thus the long timescale evolution of the instability exhibits one-dimensional coarsening dynamics. We also observed smaller domain structures which could not be quantified clearly due to the presence of undamped $m_F = 0$ density fluctuations in the initial state caused by nonadiabaticity in the initial transfer to the optical trap.

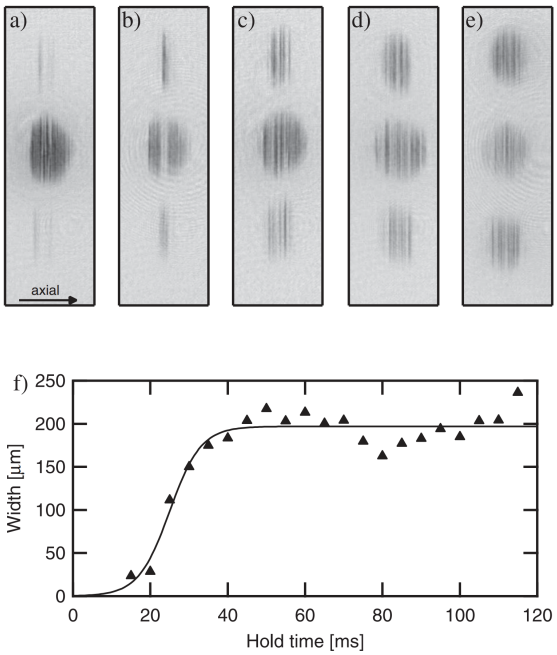

Figure 4.8: Spatial dynamics of the instability. Absorption images of the condensate taken at a time of flight (TOF) of 25 ms for a quench to q = 17.4 Hz for different hold times: a) 15 ms, b) 20 ms, c) 25 ms, d) 30 ms, and e) 150 ms. From top to bottom the images show the $m_F = 1$, $m_F = 0$, and $m_F = +1$ spin state distribution. The width of the images is 1 mm. In f) the width of the $m_F = 1$ component after a TOF = 25 ms, determined by a Gaussian fit, is plotted as a function of hold time (triangles). The fit to a sigmoid function (line) is included to guide the eye.

CHAPTER V

ANTIFERROMAGNETIC SPINOR CORRELATION

5.1 Introduction

Spin-1 condensates have higher degrees of freedom than a real or pseudo spin-1/2 systems. As a result, spin-1 systems have proven to be excellent systems to investigate complex quantum magnetic order. This is even more true in the case of out-of-equilibrium cases, where magnetic order can undergo growth and decay before reaching an equilibrium state. Exotic types of magnetic order and phases resulting from collective behavior of quantum spins are an important focus of many-body physics. Nematic or quadrupolar ordering of spins is one such example. This breaks rotational symmetry, but has no magnetic moment. This ordering can be similar to the ordering of molecules in nematic phases of liquid crystals (49). The spin-nematic phases have been investigated in a variety of condensed matter systems such as frustrated quantum magnets (50), and heavy-fermion (51) and iron-based superconductors (52). Spin-1 atomic Bose-Einstein condensates are a natural system to investigate spin-nematic quantum phases that feature well-understood underlying microscopic models, controllable interaction parameters, and flexible defect-free geometries.

In this chapter, we investigate out-of-equilibrium magnetic order exhibited by antiferromagnetic spinor sodium gas. In order to minimize the external perturbations, the magnetic field gradient have been cancelled in this case to a very small number. We characterize the spatiotemporal evolution through two particle correlations between atoms in each pair of spin states. This revealed dramatic differences between the dynamics of the spin correlations and those of the spin populations. We also study rich non-equilibrium behavior in the form of growth and decay of both nematic and magnetic spin waves. We begin with section 5.2 where we describe the experimental methodology used to study the two particle correlations. In section 5.3, we discuss the growth and decay of two particle correlations following the quench through the quantum phase transition. In section 5.4, we model our

results using truncated Wigner approximation. The experimental results show qualitative similarity with with our theoretical simulations. Finally, in section 5.5 we discuss the non-local dynamics and study the correlated density fluctuations as it spreads throughout the cloud.

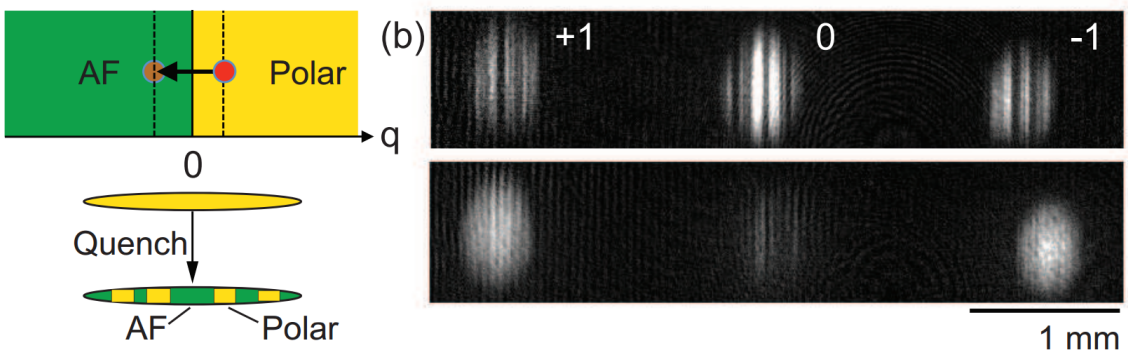

Figure 5.1: Probing quench dynamics in the vicinity of a quantum phase transition. (a) Microwave magnetic fields are used to instantly change the quadratic Zeeman shift independent of the static magnetic field. The value of q is changed from $q_1 > 0$ to $q_2 < 0$ through the quantum phase transition at $q = 0$. b) Time-of-flight Stern-Gerlach images show the spontaneous axial spin structures at a hold time of 48 ms (upper image) while by 2.5 s (lower image) the system has relaxed to an antiferromagnetic configuration free of domains. Residual fringes in the latter image are experimental artifacts due to the probe light.

5.2 Experimental Methodology

Bose-Einstein condensate was prepared in an optical dipole trap in the $m_F = 0$ state as described in detail in chapter 4. The axial magnetic field value was set to $B_z = 100$ mG, and the transverse magnetic field and axial field gradient were compensated to within 5 mG and 0.6 mG/cm respectively. The experimental set-up in this case is distinguished from the one described in chapter 4, by cancelling of magnetic field gradient. This allowed resolution of the spin ± 1 atoms to precise location enabling two partial spatiotemporal correlation study in the condensate. The peak density and the axial Thomas-Fermi radius were measured to an accuracy of 5% to be $n_0 = 5 \times 10^{14} cm^{-3}$ and $R_x = 340 \mu m$ respectively. From this, the spin-dependent interaction energy was determined to be $c_2 n_0 = h \times 120 Hz$.

The axial and radial trapping frequencies were $7Hz$ and $470Hz$, respectively, accurate to 10%. The radial Thomas-Fermi radius, $R_{perp} = 5\mu m$, was small enough such that only

axial spin domains could form. The energy available from the quench, $4Hz$, is smaller than the transverse excitation frequency which we estimate to be $50Hz$ from a 2-dimensional box model. The temperature was measured to be $400nK$, close to the chemical potential of $360nK$. We rapidly switched q from $q_i = h\times 2.8Hz > 0$ to a final value $q_f = h\times -4.2Hz < 0$ at $t = 0$. A quantum phase transition divides the polar ($m_F = 0$) ground state from an antiferromagnetic one ($m_F = \pm 1$ superposition) at $q = 0$, as shown in fig 5.1. The dynamical evolution from one to the other state is governed by the spin-dependent interaction term c_2. q was switched by turning on a far-off resonance microwave dressing field tuned to near the $F = 1 \rightarrow F' = 2$ ground state hyperfine resonance. The value of q_f was controlled through the ac Stark shift by adjusting the microwave power. Since q_i, $|q_f| << c_2 n_0$, the gas remained very close to the phase transition point at all times. Nonetheless, the change triggered a rapid instability in the $m_F = 0$ condensate. Through spin exchange collisional interactions we observed that the $m_F = 1$ population fraction $f_{\pm}$ increased rapidly starting at $t = 20$ms [see fig. 5.4(b)]. This was accompanied by oscillations and a slower period of relaxation over > 100ms toward an apparent equilibrium. We observed a 30% atom loss over 100ms due to off resonant microwave excitation.

After holding the gas for a time t, the initial spin density fluctuations were amplified, and ultimately, macroscopic, one-dimensional spatial domains were observed to have formed [see figure 5.1]. We then diagnosed the axial spin distribution using a TOF SG sequence consisting of 2ms TOF, 4ms pulsed SG field, and 24ms additional TOF to separate the three spin states, followed by a 50s absorption imaging pulse on the $F = 2 \rightarrow F' = 3$ transition of the D2 line. Because of the extreme 70 : 1 aspect ratio, the TOF axial distribution remained very close to its in situ value. Each image was Fourier filtered to remove spurious interference fringes with wavelength between 60-62 micron created by the probe light, and summed over the radial direction to obtain one-dimensional atom density distributions. We took the center of these distributions ($x = 0$) to be the maximum of the average density profile for 30 runs at each hold time t, after smoothing by a 200 micron moving average filter.

Figure 5.2 shows measured spin density profiles, $n_0(x)$ and $n_{-1}(x)$, for a single shot

of the experiment at a hold time of 68ms. Domains as small as $13\mu m$ half width at half maximum can be seen. This is 4% of the Thomas-Fermi radius, and is comparable to our imaging resolution, $d = 10\mu m$. Domains smaller than d would have expanded to a size d, and thus cannot be distinguished by the time-of-flight method from larger scale features. The energetics of the quench, however, suggest that domains no smaller than 5 micron are likely to appear.

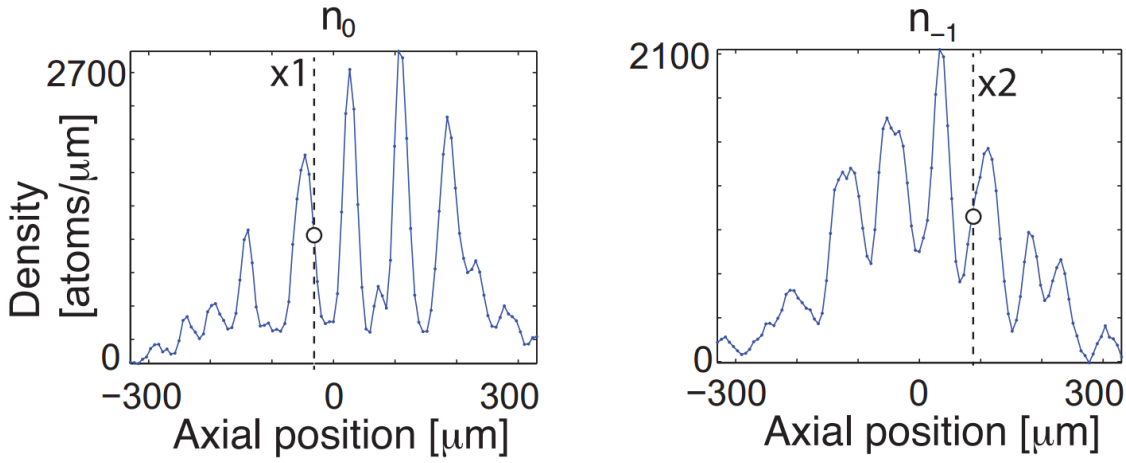

Figure 5.2: (Color online.) Sample profiles $n_0(x)$ and $n_1(x)$ measured on a single shot at $t = 68$ ms.

5.3 Observations and Discussion

In order to determine if domain formation was stochastic in nature, multiple images of the condensate was taken for a given q_{final} and hold time t. The average of these images was evaluated for different hold time and q_{final} to determine if there was any pattern behind the domain formation. The average did not show any structure indicating that the domain formation was stochastic in nature.

In order to study the stochasticity of domain formation then, the two-particle correlations were evaluated. The quench was repeated for 30 runs of the experiment for a given hold time and q_{final}. The density fluctuations n of a spin pair i,j, a two-point covariance function was computed as

$$S_{i,j}(x_1, x_2, t) = \langle \Delta\hat{n}_i(x_1, t)\Delta\hat{n}_j(x_2, t)\rangle \tag{5.1}$$

where $\langle..\rangle$ refer to ensemble averages of fluctuations about the sample mean. Averages over a smaller sample size was observed to yield similar results. The data was divided into two physical effects. Local correlation function was computed where $x_1 = x_2$, and the nonlocal effects were computed as $(x_1 \neq x_2)$. We discuss both of these results in turn below.

Figure 5.3(a) shows the measured time evolution of the local pair correlation function, $R_{i,j} = \int (dx < \Delta\hat{n}_i(x_1,t), \Delta\hat{j}(x_2,t))$. The total atom number fluctuations was subtracted from the data. Hence, the graph represents the spin fluctuations on top of the density fluctuations. For short times, $t < 35$ ms, all three spin states exhibit correlations whose absolute value rises from zero to a maximum value. This is a result of the local spin mixing process where two spin 0 atoms form a spin +1 and a spin -1 atom following the quench. This spin mixing process predicts that the ratio $R_{1,-1}/R_{-1,-1} = 1.0$ and $R_{0,-1}/R_{-1,-1} = -2.0$. Our measured peak values of the ratios are 0.9 and 2:0, respectively. Thus although the system is outside the single-mode regime (53), our data indicates that spin mixing generates nearly the maximum local correlations that are possible.

In the $t > 35$ ms timeline, the data was observed to diverge from one another. The diagonal correlations, $R_{-1,-1}$, appear to reach a steady state of 50% of their peak value. This is expect as the result of saturation of the parametric gain due to the finite number of $m_F = 0$ atoms, which causes fluctuations in the amplified modes to be suppressed. They are not, however, reduced to zero, since the same spin state must always be correlated with itself at the same location. By contrast, the off-diagonal data, $R_{-1,+1}$ was observed to decay sharply. The $R_{0,-1}$ curve has been scaled by the factor -1/2 to allow for comparison of all 3 curves, and exhibit an intermediate behavior between $R_{-1,-1}$ and $R_{+1,-1.}$.

The initial, positive correlation between ± 1 atoms is indicative of nematic spin wave excitations, which are small oscillations in the order parameter $N_{zz} = n_{+1}(x,t) + n_{-1}(x,t) - 2n_0(x,t)$. This excitation is expected in an antiferromagnetic spinor condensate as they display a nematic order.

The distinct regions in the condensate are expected to communicate with one another through the propagation of spin waves, as time evolves.. The decay of $R_{+1,-1}$ can therefore be viewed as a destructive interference between waves originating from different points in

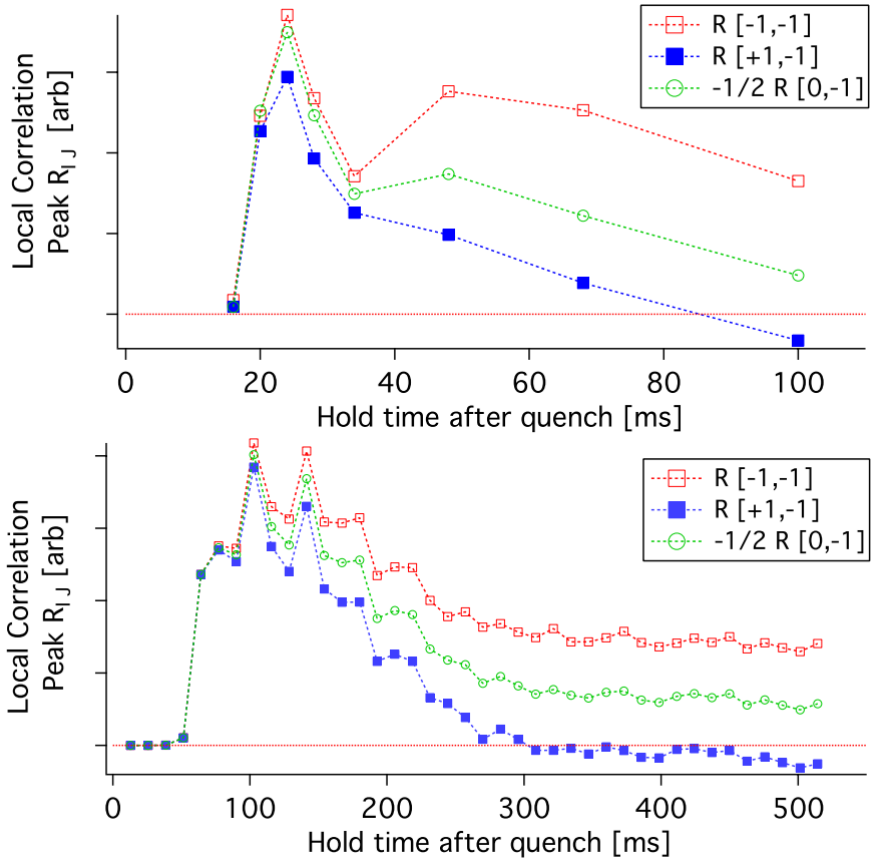

Figure 5.3: Correlation of atom pairs after the quench at $t = 0$. (a) Measured local density correlations $R_{ij}(t) = \int dx \langle \Delta\hat{n}_i(x,t)\Delta\hat{n}_j(x,t)$ for spin states $(i,j) = (1,1)$ and $(+1,1)$ versus time. Also shown is the $(0,1)$ correlation scaled by a factor $\frac{1}{2}$ as described in the text. (b) Correlation functions determined from numerical simulations. The horizontal dashed line marks zero correlation.

space. Interference effects have also been recently reported in quenched scalar superfluids, leading to oscillations in the density-density correlation function.

Accompanying this decay of $R_{+1,-1}$ is a growth of magnetic spin wave excitations, whose order parameter is $M_z(x,t) = n_{+1}(x,t) - n_{-1}(x,t)$. The local magnetization variance is $var[M_z(x,t)] = S_{+1,-1}(x,t) + S_{-1,-1}(x,t) - 2S_{-1,+1}(x,t)$ which becomes nonzero for imperfect correlation between the two spins, $S_{+1,-1}(x,t) < S_{-1,-1}(x,t), S_{-1,+1}(x,t)$ we observed experimentally. Our data in 5.3 show that $R_{+1,-1}$ reaches zero at 85 ms, after which the two spins even become negatively correlated.

5.4 Theoretical Simulations

In order to gain a theoretical understanding, the three spin states were simulated through coupled spinor Gross-Pitaevskii equations. Initially the BEC is made of $m_F = 0$ component. This was simulated by performing density simulation and the initial wavefunction for the $m_F = 0$ component was obtained numerically. The quantum noise in the $m_F = \pm 1$ state was simulated as classical noise according to the truncated Wigner approximation(54; 55; 56). The idea of the method is to generate an ensemble of classical fields which samples the Wigner function of the initial thermal density operator, and to evolve each field with the Gross-Pitaevskii equation (GPE). Like other existing approximate methods, such as the time-dependent Bogoliubov approach, it allows us to go beyond the commonly used Gross-Pitaevskii equation, in which the interactions between the condensate and the noncondensed atoms are neglected.

The Gross-Pitaevskii formulation is essentially a classical treatment, very useful, but missing a great many of the properties that proper quantum systems possess. When you try and calculate the dynamics of interacting systems, this can become a problem. The Truncated Wigner approximation addresses several of these issues. First, the indeterminate nature of states. Because you can't say for certain that there are exactly X particles in a system at any given time, as the GP formulation does, the TWA samples states immediately around the average measured value and evolves each of these, taking a combination of the resultant trajectory to calculate the expectation value. This is useful in situations such as

those observed when the particles in a BEC will decohere over time. TWA demonstrates this very nicely (though still fails to predict a number of phenomena, as always with approximations) The TWA can be extended to include spontaneous jumps in the state and other purely quantum phenomena for which the GPA has nothing to say. As usual, this accuracy comes at the expense of ease of calculation. The corrections particularly scale at horrifying rates for anyone attempting to model them numerically.

Similar to the experiment, thirty simulations were performed for each hold time and q_{final}, in order to compute the expectation value of quantum mechanical observables as statistical averages over different random initial conditions. Vacuum modes with wavelength less than the size of the spin domains are not expected to contribute to the spin instability. Therefore, a cutoff energy of $c_2 n_0$ was imposed. This resulted in 700 virtual particles, while the condensate contained 5×10^6 particles, similar to the experimental conditions. The results were observed to be relatively insensitive to this cutoff, as is also expected for an exponential amplification process. For example, magnifying the noise by a factor of 10 changed the time at which the ± 1 fraction $= 0.5$ by only 20%.

Figure 5.4b shows the numerically obtained correlation functions, which show good qualitative agreement with the experimentally observed trends. Similar to the experimental data, $R_{+1,-1}$ has dropped below zero in the simulation after 300 ms. The overall dynamics were faster in the experiment by approximately this factor, 300/85=3.5, which we cannot presently account for. Possible effects include residual ± 1 population in the initial state caused by thermal or technical fluctuations that would speed up the instability. In addition, atom loss (in our case due to off resonant microwave excitation) can cause decoherence (57).

The simulations revealed that even in the absence of thermal or technical noise, vacuum fluctuations can induce a decay of correlations.The initial vacuum noise for the two bosonic fields, ϕ_{+1} and ϕ_{-1}, are expected to be uncorrelated, for any particular realization of the experiment. And, the spin mixing instability can amplify tiny differences in initial conditions. As a result of which, the final wavefunctions $\phi_{\pm 1}(t = t_F)$ are expected to differ macroscopically i.e. by much more than just the initial vacuum noise. The truncated wigner

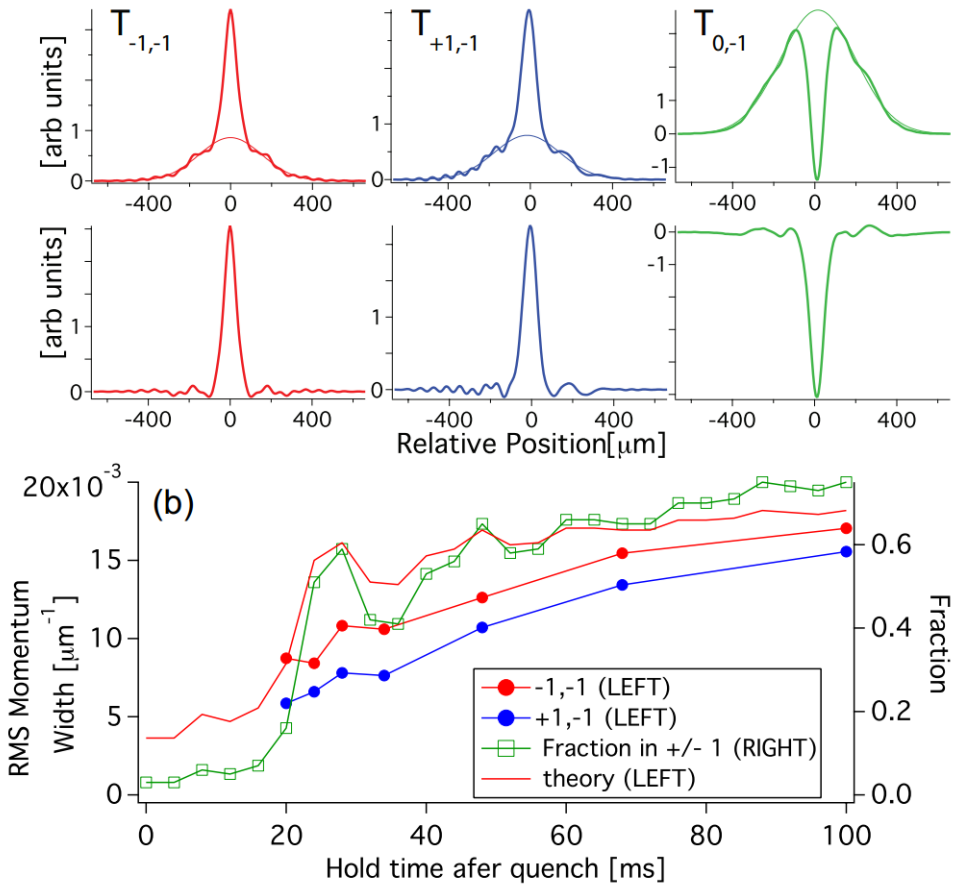

Figure 5.4: (Color online.) Nonlocal correlations and spin domain dynamics. (a) Top row shows $T_{i,j}(\delta) = \int S_{i,j}(x, x+\delta)dx$ for various spin pairs and relative position δ. Bottom row shows the same data with the background caused by atom number variations subtracted. (b) Dynamics of the fraction of atoms in ± 1 (green squares, right axis), the RMS momentum width determined from the Fourier transform of $T_{1,1}$ and $T_{1,+1}$ (red and blue circles, respectively, left axis) and from a theoretical prediction (solid red line, left axis).

simulation of an identical initial condition $\phi_{\pm 1}$ (, which is an extremely rare physical situation (negligible probability) resulted in identical time evolution and no decay consistent with the symmetry of the GP equations.

5.5 Non Local Dynamics

We conclude by quantifying the nonlocal dynamics. Figure 5.4 shows a one-dimensional reduction of the covariance map S_{ij} in terms of relative coordinate , $T_{i,j}(\delta, t) = \int < \Delta n_i(x,t)\Delta n_j(x+\delta,t) > dx$, and for spin pairs $(-1,-1)$, $(+1,-1)$, and $(0,-1)$, at $t = 20$ ms after the quench. A narrow peak of either polarity is observed in all cases near $\delta = 0$. A smooth, positive background lies underneath it which is expected from the shot to shot atom number variations. This also lead to correlated density fluctuations throughout the cloud. The outer wings of the data showed good fit with the Gaussian distribution. By subtracting the fit with the actual data, the intrinsic fluctuations were obtained. This is plotted underneath. The data shows a sharp, local correlation peak surrounded by oscillations. The height of the peak was determined by an additional Gaussian fit, and constitutes the data of fig 5.3.

The oscillations signify a dynamically evolving nonlocal order induced by the rapid quench, which we characterized by computing the Fourier transforms, $T_{+1,-1}(k)$. These showed an increase in high spatial frequency components with time after the quench. Figure 5.4(b) shows this trend as a growth in the second moment of the Fourier transforms. Higher order effects in the SG expansion are responsible for the slight magnification of k_{rms} for the $(-1,-1)$ relative to $(+1,-1)$.

While a rapid quench is expected to lead to coarsening of the domains on long time scales (8; 58) our data show the opposite trend within the time window 100 ms. This suggests that it might be an intermediate phase of evolution that precedes coarsening. In fact, energy conservation requires the kinetic energy to grow with the $m_F = 1$ populations, since they reduce the quadratic Zeeman energy. Using $\hbar^2 k^2/2M$ from the correlation functions as an estimate of the mean kinetic energy. This formula is plotted as a solid line fig.5.4(b) using our measurements, and shows the same trend as our data. It consistently lies above

our measurements, most likely due to the fact that we do not account for variations in the phase of the order parameter nor the interaction energy contained in the finite width domain boundaries.

CHAPTER VI

LINEAR ZEEMAN CORRECTION

6.1 Introduction

Phase transition are an enormously revealing many-body events in nature because of their singular behavior. Near a phase transition system properties change extremely rapidly, such that in the thermodynamic limit the transition point becomes a mathematical singularity. Yet all systems are finite and heterogeneous, because of which the true singularity is always suppressed in some way in the real world. In the domain of superfluids, the spectacular lambda point of liquid helium is smeared out by the earth's gravitation, requiring precision comparisons of experiment and theory to be performed in space (12). For quantum gases of ultracold atoms the problem is even more severe, as the density variations are intrinsic, and must be accounted for in order to achieve quantitative agreement with a statistical description of the system (13)(14). Measuring the detailed behavior near a phase transition is important for revealing critical phenomena and universality, both of which are actively sought with these systems.

Quantum phase transitions are especially amenable to discovery and observation using trapped gases of ultracold atoms. In the simplest description, such a transition contains two competing terms which may be tuned relative to each other, with a critical point in parameter space that lies in a region where both terms contribute significantly. A classic example is the superfluid-Mott Insulator transition in an optical lattice, where the ratio of interaction strength to tunneling, U/J, determines the transition point. By tuning U relative to J, one approaches the critical point, where the system ground state changes discontinuously (see (2) for a pedagogical description). Both U and J, however, are inhomogeneously distributed in space, resulting in a shell structure of different phases (59) and broadening of the transition point. Thus it is widely believed that all, or most of the phase transitions encountered in ultracold atomic systems necessarily suffer this same type

of problem.

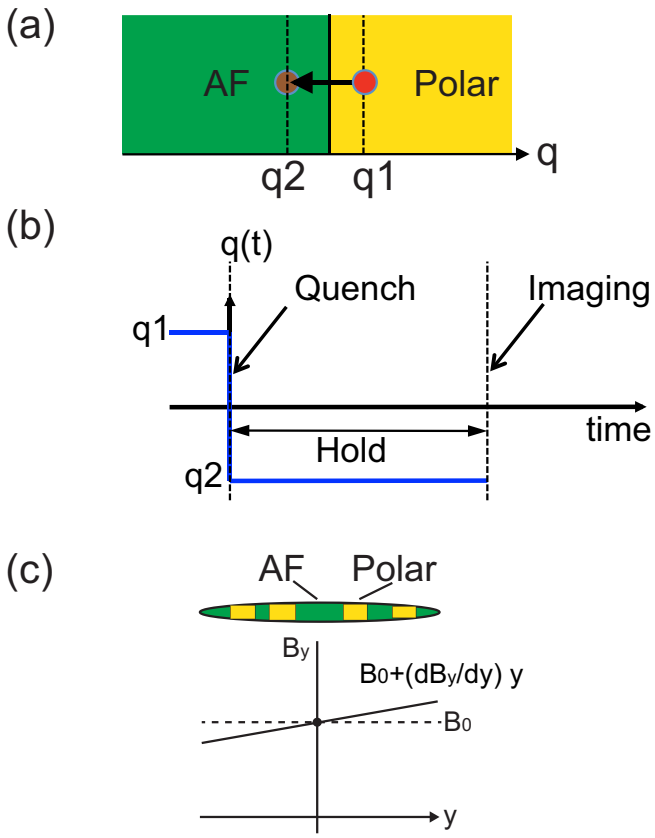

Figure 6.1: (Color Online). Probing quench dynamics in the vicinity of a quantum phase transition. (a) Microwave magnetic fields are used to instantly change the quadratic Zeeman shift independent of the static magnetic field. The value of q is changed from $q_1 > 0$ to $q_2 < 0$ through the quantum phase transition at $q = 0$. (b) Timing diagram of the experiment. (c) Static magnetic field, which is unchanged during the experiment, consists of both a bias field B_0 pointing along the long axis of the condensate as well as a magnetic field gradient.

This chapter discusses a remarkable exception that occurs in a spinor Bose-Einstein condensate. The transition we examine is between polar and anti-ferromagnetic spin states in an antiferromagnetic spin-1 BEC (see figure 6.1). It is not smeared out by density inhomogeneities, as the critical point does not depend upon density at all. Rather, the energy difference between the two competing states, which in turn is controlled by external fields through the quadratic Zeeman effect, sets the phase boundary. As a first-order quantum phase transition, it offers a unique perspective, as intrinsic inhomogeneity does not smear out the singular behavior discussed earlier.

In this work we follow upon earlier observations (60; 61) to make precise measurements of this phase transition. We compare our predictions with Bogoliubov theory as well as numerical simulations, finding good agreement in some, though not all, cases. In particular, the theory provides strong evidence for the spatially localized state observed in our early work (60), for which the inhomogeneous density profile plays an important role. It also quantitatively accounts for the magnitude of the instability rate, shedding light on discrepancies that were noted earlier (60).

A central theme of our work is the use of *dynamics* to probe the phase transition through instabilities generated by a rapid quench. Simply by changing the quench parameters, we are able to map out the phase boundary. We do not need to probe the ground state of the system or wait for it to reach equilibrium, as many early works on spinor gases have done (16; 22). This greatly simplifies the experimental protocol, as the dynamics may be observed in the 10-100 ms, rather than 1-10 second range. We show that the rapid variation of the instability near the transition point can allow for a precise determination of its location.

6.2 Hamiltonian with Linear Zeeman Correction

Our starting point is the spin-dependent mean-field Hamiltonian for spin $F = 1$ Bose-Einstein condensates (see (62) and references therein):

$$H_{sp} = \frac{c_2}{2} n(\mathbf{r}) \langle \hat{\mathbf{F}} \rangle^2 + p(\mathbf{r}) \langle \hat{F}_z \rangle + q \langle \hat{F}_z^2 \rangle$$

Here we are only interested in the dynamics within the low-energy spin sector (Hz energy range) following a quench of q from positive to negative values (see figure 6.1a). We have removed the spin-independent terms from the Hamiltonian, which are assumed to be a constant. $\hat{\mathbf{F}}, \hat{F}_z$ are the vector spin-1 operator and its z-projection, respectively and n is the particle density.

The Hamiltonian written above is defined by the competition between the intrinsic magnetic interactions and the coupling to the external magnetic field. The spin-dependent interaction coefficient c_2 arises from spin-changing collisions that can convert two $m_F = 0$ atoms into an $m_F = \pm 1$ pair and vice-versa, a process constrained by the conservation of

angular momentum The intrinsic interactions are antiferromagnetic for $c_2 > 0$ or ferromagnetic for $c_2 < 0$. In this work we consider a sodium BEC, for which $c_2 > 0$.

In our experiment, both the bias magnetic field as well as its spatial variation must be accounted for in the description of the quantum phase transition (see figure 6.1b). The latter occurs due to stray field inhomogeneities in our apparatus, as well as to field gradients that are deliberately applied. Therefore, we have written the external field coupling to include both linear (p) and quadratic (q) Zeeman shifts. In the above equation, $p(\mathbf{r}) = \mu B_0 + \mu \nabla B \cdot \mathbf{r}$ and $q = \tilde{q} B_0^2$. B_0 is the magnetic field at the trap center, $\tilde{q} = 277\text{Hz/Gauss}^2$ is the strength of the quadratic dependence for sodium atoms, and the magnetic moment μ is $\frac{1}{2}\times$ the Bohr magneton μ_B.

If the external field is completely homogeneous, i.e., $p(\mathbf{r}) = \mu B_0$ is a constant, then the z-component of the spin commutes with the Hamiltonian. This conservation law holds true not just at the mean field level, but at the many-body level, within the approximation that the two-body interactions conserve spin. The weak dipolar interaction, neglected in this treatment, violates this conservation law. Hence, a gauge transformation allows this term to be removed. Thus we may take $p = 0$, whence only the quadratic Zeeman term is present. For an antiferromagnetic spinor BEC constrained to have zero net magnetization, the ground state for $q > 0$ is a polar condensate consisting of a single component–the $m_F = 0$ spin projection that minimizes $\langle \hat{F}_z^2 \rangle$. For $q < 0$ the ground state maximizes the same quantity through a superposition of two components $m_F = \pm 1$, a so-called antiferromagnetic phase (44). The symmetry properties of the ground state therefore change discontinuously at $q = 0$, defining a zero temperature quantum phase transition (44; 60).

For positive q, i.e., away from the transition region, the influence of both linear and quadratic Zeeman shifts on the equilibrium properties of one-dimensional antiferromagnetic spinor condensates has been studied in detail by the Ketterle group (16; 19). Our present work is distinguished from those results in two critical ways. For one, we focus not on the *equilibrium* structures that arise from minimizing the energy, but on *dynamics* while crossing through the transition point. Our earlier studies of these dynamics have followed in detail both the populations (60) as well as the spontaneous creation of non-equilibrium spin

structures (61). Secondly, we have explored these dynamics by varying the *linear* Zeeman term, p, through a spatially inhomogeneous magnetic field. We find, contrary to intuition and to earlier observations of equilibrium properties in the positive q region (16), that this field gradient suppresses the tendency for the $m_F = 0$ condensate to phase separate into an $m_F = \pm 1$ mixture. This suppression can be explained, however, by analyzing the unstable eigenmodes that are populated by the quench and uncovering, theoretically, their dependence upon p. As in our earlier work, we use static magnetic fields to control p, and deploy a microwave magnetic field to vary the quadratic Zeeman shift q via AC Stark shifts (24).

6.3 Experimental Results

6.3.1 Method

Optically confined Bose-Einstein condensates in the $m_F = 0$ state were prepared in a static magnetic field of $B_x = 100$ mG in a manner described in our earlier work (60). Transverse magnetic field and axial field gradient were compensated to within 5 mG and 0.6 mG/cm, respectively. The peak density $n_0 = 5 \times 10^{14}\text{cm}^{-3}$ and axial Thomas-Fermi radius $R_x = 340$ μm were measured to an accuracy of 5%, from which we determined the spin-dependent interaction energy $c_2 n_0 = h \times 120$ Hz. The axial and radial trapping frequencies were 7 and 470 Hz, respectively, accurate to 10%. The radial Thomas-Fermi radius, $R_\perp = 5$ μm, was small enough such that only axial spin domains could form [1]. The measured temperature was 400 nK, close to the chemical potential of 360 nK.

We rapidly switched q from $q_i = h \times +2.8$ Hz > 0 to a final value $q_f = h \times -4.2$ Hz < 0 at $t = 0$. Following a variable hold time, we switched off the trap and used time-of-flight Stern-Gerlach (TOF-SG) observations to record the one-dimensional spatiotemporal pattern formation in each of the 3 spin components, $n_i(x); i = 0, \pm 1$, with a resolution of 10 μm. For the current work we focus on the total population in each of the spin states, $N_i = \int n_i(x) dx$, as well as the population fractions $f_i = N_i / \sum_j N_j$.

[1] The energy available from the quench, $h \times 4$ Hz, is smaller than the transverse excitation frequency which we estimate to be $h \times 50$ Hz from a 2-dimensional box model.

6.3.2 Linear Zeeman shifts and Field Gradients

Bias fields were generated using three pairs of Helmholtz coils wrapped around the vacuum chamber. To compensate magnetic field gradients, we used an anti-Helmholtz coil pair to generate field gradients of up to 160 mG/cm. Background field gradients along the y-direction were observed to be in the neighborhood of 80 mG/cm, which could be cancelled easily by the coils.

For a cloud comprised only of $m_F = \pm 1$ atoms, the linear Zeeman energy gained by moving an atom of either spin state axially to the edge of the cloud is defined to be a quantity

$$p \equiv g_F \mu_B B' R_{TF}$$

. At this location it has lost the antiferromagnetic interaction energy $U = c_2 n_0$. Setting these two energies equal to one another, we achieve a critical magnetic field gradient

$$\left(\frac{\partial B}{\partial y}\right)_{crit} = \frac{U}{g_F \mu_B R_{TF}} = 4.6 \frac{\text{mG}}{\text{cm}}$$

using the peak value for n_0 and the axial Thomas-Fermi radius of 370μm.

To cancel the field gradient, we tuned the current through these coils in order to maximize the lifetime, for $q > 0$, of the $m_F = 0$ component against spin relaxation into ± 1 pairs, observing that the latter spin states were completely miscible under these conditions (16), as expected from the above formula. Our tuning was limited to ± 0.3 mG/cm by the finite current resolution of the power supply controls, a technical barrier which can be overcome in the future in a straightforward manner to achieve finer control. Within our current experimental resolution, the residual linear Zeeman energy p after cancellation of stray magnetic field gradients was no more than ± 7 % of the spin-dependent interaction energy U.

6.3.3 Precise Measurement of the Phase Transition near $q = 0$

Figure 6.2 shows our principal experimental observation, which is the extreme sensitivity of the instability rate to quadratic Zeeman shift near the phase boundary, allowing for a precise determination of the latter. This behavior was observed for magnetic fields aligned

parallel to the long axis of the cigar-shaped BEC. We measured a stark difference for fields aligned transverse to this axis. In this case, according to our earlier observations noted in chapter 4 (data reproduced from (60) in figure 6.2 as symbol 'Z'), a significant discrepancy was noticed between the experimentally observed instability rates and those predicted by Bogoliubov theory, particularly for data taken very close to the phase transition (60). The experimental data suggested a smooth turn-on of the instability rate rather than a sharp transition point.

In figure 6.2a,b we examine this effect in greater detail. We reproduced this difference for magnetic fields along the orthogonal transverse X direction. By contrast, along the Y-direction, after experimentally reducing the stray magnetic field gradients as described earlier, we observed much better agreement with theory. We observed a factor of up to 10 larger instability rate at small q for B_y compared with B_x and B_z , which resulted in a dramatic sharpening of the phase transition. This data was observed for 3 different magnetic fields $B_y = 100, 145$ and 170 mG, where the microwave power was adjusted accordingly to cover the same range of total quadratic Zeeman shift. In all 3 cases the data collapsed onto a single curve, as observed in figure 6.2b. Thus the precision of our measurement was sufficient to distinguish a very small shift of the phase transition point from $q = 0$ to $q = +0.5 \pm 0.2$ Hz. For larger static fields of 200 mG, the difference between transverse and longitudinal instability rates was less appreciable, for reasons that are not presently clear.

The precise determination of phase transition has been achieved by a combination of precise magnetic field control as well as a transition itself whose value depends *only* on external parameters rather than on the particle density. The latter case results in a smearing of the transition point due to density inhomogeneities, or a shell structure in the case of the Mott Insulator-Superfluid transition (59). The data taken with field gradient shows good agreement with a calculation of the instability rate for $B' = 0$ using numerical solution of the Bogoliubov equations, as detailed in a following section.

While the data in figure 6.2 appear to have a universal character, we do not yet have a complete explanation for the dependence upon static field orientation. In a mean-field theory of the spinor BEC, the absolute orientation of the static magnetic field, which defines

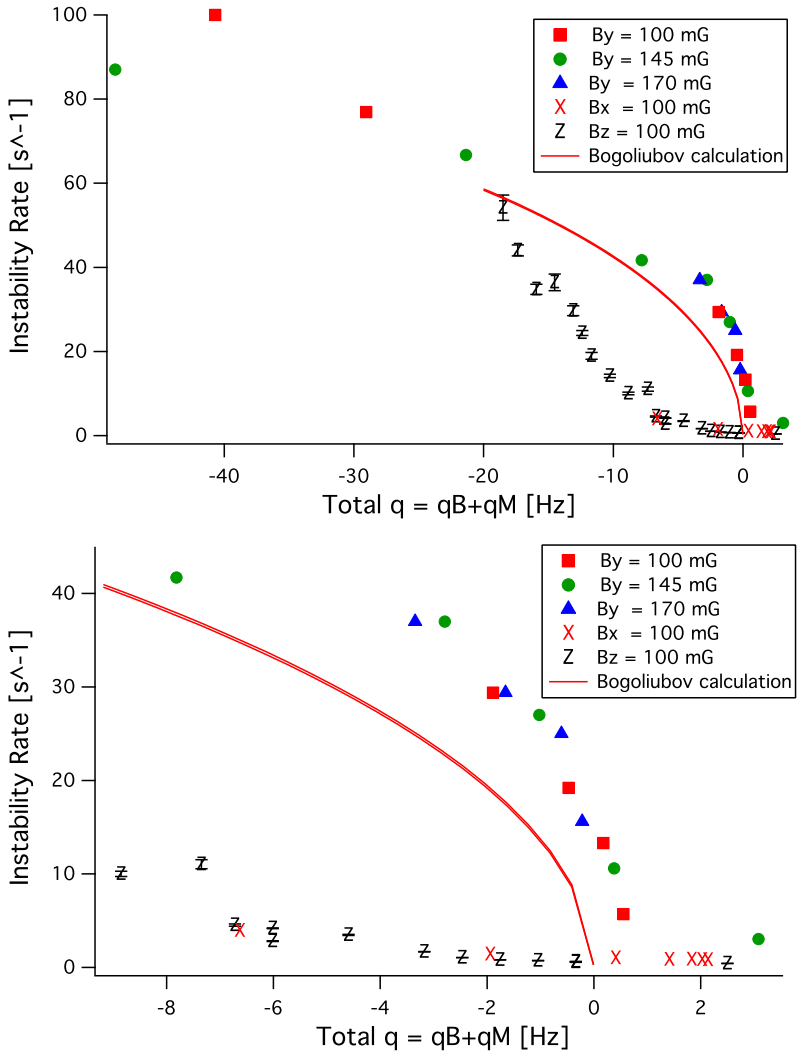

Figure 6.2: Dramatic sharpening of the phase transition for fields aligned with the axis of the condensate (Y-direction, where the magnetic field gradient has been deliberately cancelled to less than 0.6 mG/cm, or $p/U < \pm 0.07$. Shown is the instability rate versus quadratic Zeeman shift for static magnetic field $B \parallel \hat{y}$, i.e., aligned along the cigar (solid symbols), and for $B \perp \hat{y}$, aligned along the two orthogonal transverse directions Z and X, respectively. Z-data is reprinted from (60).

the quantization axis for the atoms' spin state, should not influence the physics in any way. Only the field magnitude, $B = |\vec{B}|$ appears in the quadratic and linear Zeeman terms in the Hamiltonian. However, inhomogeneities in the field magnitude might be different for fields that are oriented along different directions. We show later that a spatial gradient of the linear Zeeman term does in fact suppress the instability rate of a quasi-one dimensional antiferromagnetic spinor BEC by a large factor of order 10 for experimentally accessible applied field gradients. Since the gradient of B_y was explicitly compensated in figure 6.2, while those of the transverse fields $B_{x,z}$ were not, this effect by itself might explain the observed differences, and a departure from mean-field theory would not need to be considered.

To understand this point in further detail, we note that for a one-dimensional system we only need to consider variations in magnetic field along the y direction. Thus for fields that are mostly pointing in the y-direction,

$$B = |\vec{B}| \approx B_0 + \frac{\partial B_y}{\partial y} y$$

and by applying an external field gradient $-\frac{\partial B_y}{\partial y}$ we could cancel the field inhomogeneity to first order. For a bias field pointing mostly along z, the only term that is relevant in the same order is the variation of that field along y:

$$B = |\vec{B}| \approx B_0 + \frac{\partial B_z}{\partial y} y$$

since all other gradient terms $\partial B_{y,x}/\partial y$ add in quadrature and should be suppressed. A similar argument applies to B_x. Transverse field inhomogeneities of this type could neither be easily characterized nor cancelled using our current setup [2]. However, they do appear to play some role in the problem, since for long times $t > 1$ second, as observed earlier (60), the cloud separated into two distinct domains of $m_F = \pm 1$, consistent with a gradient in the linear Zeeman term. In the absence of a field gradient these two spin states would be miscible with one another.

Another possible factor could be that the spinor condensate, whose Thomas-Fermi radii are $350 \times 5 \times 5\mu$m, is not truly one-dimensional, and transverse spin excitations might be

[2]This requires the installation of coils at an angle with respect to the principal $\hat{x}, \hat{y}, \hat{z}$ directions of our apparatus

responsible for the instability. These would certainly be sensitive to other magnetic field gradient terms such as $\partial B_z/\partial z$ and $\partial B_x/\partial x$. This explanation is inviting, moreover, since the spin-dependent healing length $\xi_{sp} = 1.5\mu$m is still smaller than the transverse radius of $R_\perp = 5\mu$m. However, a simple calculation shows that transverse excitations are not relevant for our data since they are simply too energetic. If we consider the transverse confinement to be a two-dimensional cylindrically symmetric box potential, the eigenenergies of a free particle with radial and azimuthal quantum numbers n, l are determined from the zeros of the Bessel function $J_l(\beta_{n,l}) = 0$:

$$\epsilon_{n,l} = \frac{\hbar^2}{2MR_\perp^2}\beta_{n,l}^2$$

Such a model was used to analyze a similar instability in $F = 2$ condensates of ^{87}Rb, where the quadratic Zeeman energy was resonant with transverse excitations for positive, rather than negative q (63; 64). For our system, the lowest three box energies are $\epsilon_{1,0}, \epsilon_{1,1}, \epsilon_{1,2} = h \times 50, 131$, and 232 Hz, respectively, and are comparable to the spin-dependent energy U. In Bogoliubov theory we expect the eigenvalue of a collective excitation to become unstable only when $q < -\epsilon_{n,l}$ (60; 63; 44). Our experimental data covers a different region $h \times -50\text{Hz} < q$, including large instability rates for $h \times -2$ Hz $< q < 0$. Thus transverse instabilities cannot be responsible for the dynamical behavior of the system close to the phase transition point. On the other hand, the energy of the lowest *axial* mode of the box potential is smaller by a factor which is approximately the square of the cloud aspect ratio, $(R_y/R_\perp)^2 = 5 \times 10^{-3}$, and is

$$\epsilon_{0,ax} = \frac{\pi^2\hbar^2}{2MR_y^2} = h \times 0.004\text{Hz}$$

a number that is much smaller than our resolution of the quadratic Zeeman shift ≈ 0.1 Hz.

An alternative and very intriguing explanation is a genuine orientation dependence of the instability upon the bias field. This would signal physics beyond a mean-field description of the spinor BEC, an exciting development. For example, dipolar interactions have an anisotropy in space and can influence the spin relaxation rate for sufficiently anisotropic trapping potentials (65). The similarity of the data in figure 6.2 for both X and Z field suggests this as a possibility, although the effect in (65) is unfortunately too weak to explain

the factor of 10 suppression observed. Without further evidence we hold this explanation in abeyance.

6.3.4 Effect of magnetic field gradient on phase transition

To more fully understand the role of magnetic field gradients, we applied fields oriented along Y, a direction where the field homogeneity could be ensured up to second order using one pair of Helmholtz and one pair of anti-Helmholtz coils. Figure 6.3 shows the experimentally observed suppression of the instability caused by an external magnetic field gradient. Similar to our earlier work, we show the time evolution of the $m_F = \pm 1$ populations following a quench at $t = 0$ (60; 61). Data were taken at a quadratic Zeeman shift of -4.8 Hz. In the presence of an inhomogeneous magnetic field, these populations took much longer to develop than in the case where the field was uniform. We define the rate of instability $\Gamma = 1/t_{1/2}$, where $t_{1/2}$ is time taken for the fraction in ± 1 to reach 0.5. We observe that for a homogeneous field, $t_{1/2} = 20$ ms while in the presence of a gradient it was slowed down by a factor of 20, to 400 ms.

Figure 6.4 shows instability rate with field gradient in the range of 0 to 10 Hz/m. It confirms that the maximum rate occurs near $B' = 0$, and falls off as field gradient increases. In all cases, the variation of quadratic Zeeman shift across the condensate was less than 0.3 Hz and could not contribute to any significant change in the rate of instability. Indeed, we believe the explanation for our data lies in the variation of the *linear* Zeeman effect, as we explain below.

The Ketterle group showed that the symmetry between $m_F = \pm 1$ states is broken by the linear Zeeman effect (16; 19). Therefore, while co-locating the two spin states minimizes the antiferromagnetic energy $c = c_2\bar{n}/2$, separating the two clouds on opposite ends of the trap minimizes the linear Zeeman energy p. Including both effects, they showed that for sufficiently strong field gradients the ground state consists of a central $m_F = 0$ region flanked by $m_F = \pm 1$ mixtures at the cloud edges. For $q > 0$, therefore, the stability of the polar state, $m_F = 0$, was *reduced* by the presence of a field gradient, an effect they observed directly.

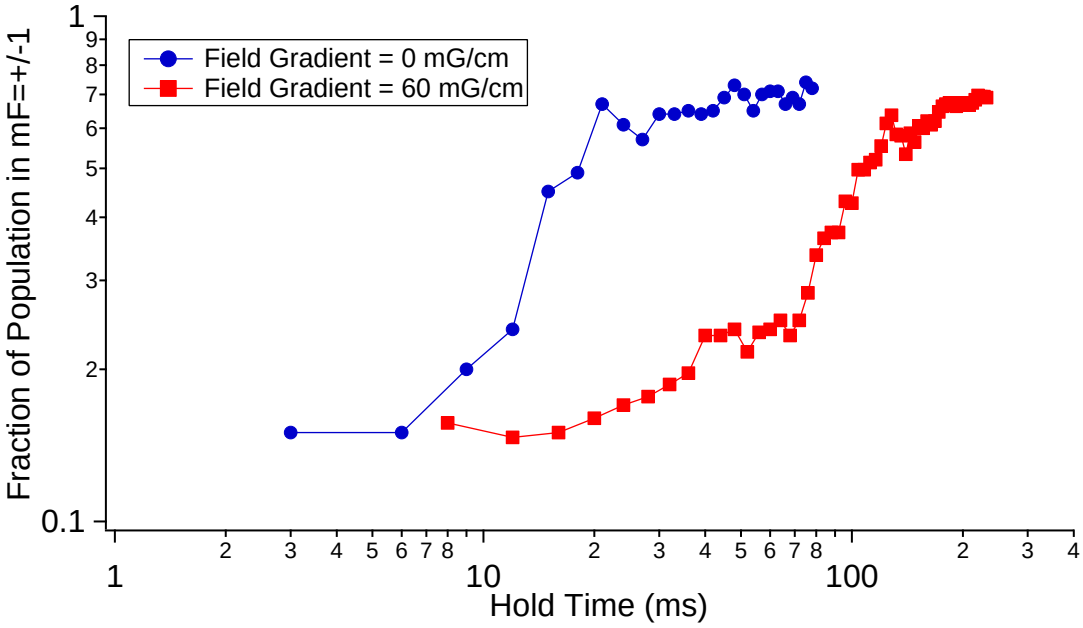

Figure 6.3: (Color Online). Field gradient slows down instability. Shown is the time evolution of the $m_F = \pm 1$ populations following a sudden quench of the polar $m_F = 0$ state from $q > 0$ to $q < 0$. Blue circles are data taken with $B' = 0$ mG/cm, while red squares are taken with $B' = 100$ mG/cm. Axes are chosen to be logarithmic in order to clearly show both data sets on the same plot.

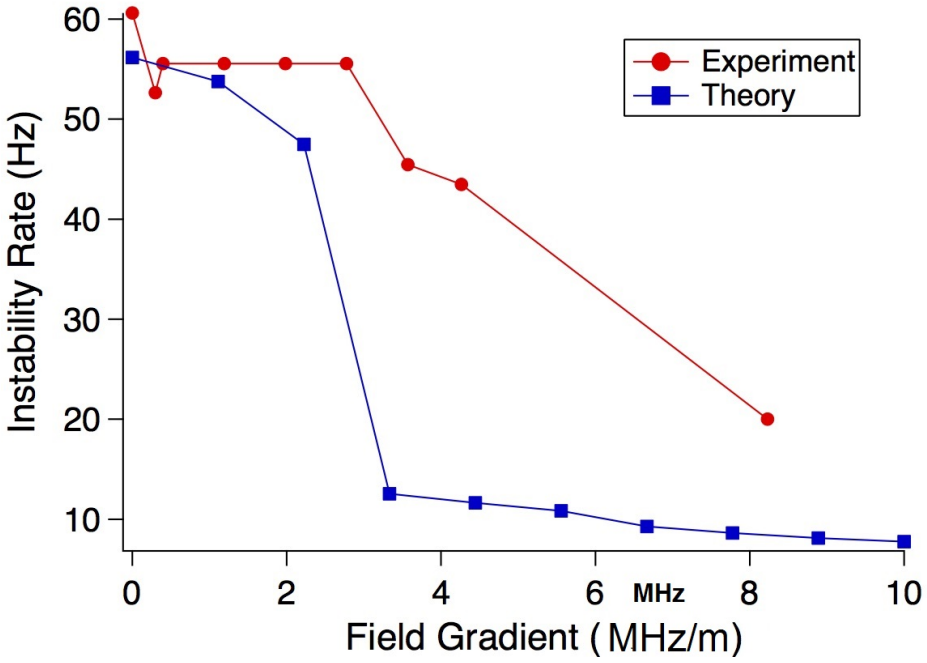

Figure 6.4: Effect of field gradient on instability rate. Shown is effect of field gradient on instability rate following a sudden quench from $q > 0$ to $q < 0$ in presence of varying magnetic field gradients. The final q was set to -4.8 Hz

By contrast, we observe in our work that for $q < 0$, the field gradient *increases* the relative stability of the polar state. This regime of quadratic Zeeman shift can only be accessed using microwave fields, and was unobserved by Ketterle's group. Our result appears to be counterintuitive since the linear term would be expected to favor a mixed state, as Ketterle's group showed. However, it can be explained by considering the *mechanism* of instability rather than the ground state phase diagram. For $q < 0$ small deviations from the polar state are parametrically amplified at a rate proportional to $c_2 n_0(x)$, a rate that is highest at the center of the $m_F = 0$ Thomas-Fermi distribution at $x = 0$. In the absence of a field gradient the maximally unstable mode is spatially localized near $x = 0$. At finite B' the unstable modes shift to a finite location $x = \pm r$ from the center, where $0 < r < R_{TF}$, in order to gain linear Zeeman energy. As B' increases, so does r, and since $n_0(r)/n_0(0) < 1$, the rate of instability decreases monotonically, as observed experimentally in figure 6.4.

The homogeneous theory is in considerable disagreement with our data, which could be attributed to finite size and geometry of our trap. Moreover, the background instability is not expected to be the same for varying values of field gradient, which would induce a departure with our theoretical simulations. This theory does not account for possible spin exchange between the condensate and the residual thermal coud, which could play a role in our observations.

6.4 Bogoliubov Theory

Our purpose in this section is to understand how the dynamical instability arises. Our effort closely parallels that of other experimental observations of spinor instabilities, with important differences. For example, Bogoliubov theory was applied to a finite $q > 0$ instability of ferromagnetic $F = 1$ ^{87}Rb spinor BEC (23), as well as to the $q = 0$ instability (64) and other instabilities (66) of antiferromagnetic $F = 2$ spinor BEC. Broadly speaking, these works have identified instabilities arising either through bulk modes with a finite wavevector, as in (23; 66), or a specific mode or set of modes that are resonantly excited at specific values of the quadratic Zeeman tuning parameter (64). Our studies, by contrast, explore an intermediate regime. A bulk analysis assuming spatial homogeneity fails to capture essential

features of our observations. However, neither is our experiment dominated by the discrete mode structure of the trap, as the relevant modes are too closely spaced for us to resolve. Instead, in our specific experimental geometry, the inhomogeneous density profile plays an important role in defining the instability and imparting to it rich features. We uncover these features by solving the Bogoliubov equations directly in coordinate space.

Bogoliubov theory was first applied to multicomponent (spinor) BEC separately by Ho (67) and Ohmi and Machida (68). Following their approach and others (44), one linearizes the spinor Gross-Pitaevskii (GP) equations (or the corresponding Heisenberg equations of motion for the field operators) about an initial state that is classical. In our case and several of the examples above, this is a state ψ_0 consisting of all atoms in the $m_F = 0$ sublevel, with only small corrections $\delta\psi_{\pm 1}$ describing the populations in $m_F = +1$ and -1. Due to the small ratio c_2/c_0, we assume that the spin instabilities do not couple strongly to density fluctuations, and thus we can neglect fluctuations in the $m_F = 0$ state. The resulting spinor wavefunction may be written as

$$\Psi = \Psi_0 + \delta\Psi = \begin{pmatrix} 0 \\ \psi_0 \\ 0 \end{pmatrix} + \begin{pmatrix} \delta\psi_{+1} \\ 0 \\ \delta\psi_{-1} \end{pmatrix}$$

and the resulting linearized spinor GP equation for $m = \pm 1$ is (69):

$$\begin{aligned} i\hbar\frac{\partial\psi_m}{\partial t} = &\left(-\frac{\hbar^2}{2M}\nabla^2 - p(x)m + qm^2\right)\psi_m \\ &+U(x)\left(\psi_m + \psi^*_{-m}\right) \end{aligned} \tag{6.1}$$

In the above we have simplified the notation to $\psi_m \equiv \delta\psi_m$, and assumed a one-dimensional description with axial coordinate x, so that $U(x) = c_2 n_0(x) = c_2|\psi_0(x)|^2$. In Eqn. (6.1) $p(x) = \mu B_0 + \mu B' x$ and $q = \tilde{q}B_0^2$ are the linear and quadratic Zeeman shifts, respectively. B_0 is the static externally applied field, $\tilde{q} = 277\text{Hz/Gauss}^2$, and the magnetic moment μ is $\frac{1}{2}$ the Bohr magneton μ_B.

Expanding the wavefunctions in a basis of spin excitations, with spatial mode index k and frequency ω_k:

$$\psi_m(x,t) = \sum_k u_{k,m}(x)e^{-i\omega_k t} + v^*_{k,m}(x)e^{+i\omega_k t} \tag{6.2}$$

Note that since the above is actually two equations, one each for $m = \pm 1$, there will be two spin modes associated with each spatial mode k. Putting Eqn. (6.2) into Eqn. (6.1) and equating terms with equal time-dependence, we get the Bogoliubov-de Gennes equations:

$$\begin{aligned} Eu &= \left(-\frac{\hbar^2}{2M}\nabla^2 + q - p(x) + U \right) u + Uv \\ -Ev &= \left(-\frac{\hbar^2}{2M}\nabla^2 + q + p(x) + U \right) v + Uu \end{aligned} \tag{6.3}$$

and

$$\begin{pmatrix} u_{k,1} = u \\ v_{k,-1} = v \\ E \end{pmatrix} \text{ and } \begin{pmatrix} u_{k,-1} = v \\ v_{k,1} = u \\ -E \end{pmatrix}$$

with $E \equiv E_k$, are the solutions for the two spin modes. These are simply the positive and negative energy pairs of the Bogoliubov equations (13). Our numerical algorithm simultaneously finds both spin wave modes with one diagonalization of Eqns. (6.3).

As a consequence of the instantaneous change in q, one or more collective modes in Eqn. (6.2) has an energy eigenvalue E_k which crosses into the complex plane. This triggers an exponential growth in the population of those modes, which are linear combinations of the spin states ± 1. Thus the populations $\psi_m^\dagger \psi_m$, for $m = \pm 1$, also grow exponentially with time, similar to a parametric amplifier (70). Although we have not written down the Bogoliubov expansion in terms of the field operators ψ_m, it is straightforward to do so, and all quantum effects and correlations can be calculated in a straightforward manner (44).

Before turning to solutions to the equations, we point out some differences between the coordinate and momentum representations. For uniform systems, Bogoliubov theory is best described in momentum space, using plane wave modes. One can then write the annihilation operator for a boson with momentum $\mathbf{k}$ in terms of corresponding operators for quasiparticles with momenta $\mathbf{k}$ and $-\mathbf{k}$. The Bogoliubov transformation contains within it, therefore, a direct correlation between quasi-particles of opposite momenta. This correlation is similar to that obtained in the Bogoliubov diagonalization of the Hamiltonian of a single component weakly interacting Bose gas (71).

In our experiment, where the $m_F = 0$ condensate has a Thomas-Fermi spatial density

profile, an expansion in momentum eigenstates is not useful. Instead, we have followed the approach of Ruprecht et al. in the analysis of collective excitations of a scalar BEC in a trap (72). In that case, the Thomas-Fermi density profile led to collective mode functions that were spatially varying, and which represented modes located inside of or near the Thomas-Fermi surface.

We will find the same to be true of the collective spin modes for a spinor BEC under harmonic confinement. An alternate way to view these modes is in terms of standing wave solutions $u_{k,m}(x), v_{k,m}(x)$ for the small excitations ± 1 that are created by the boundaries of the $m_F = 0$ cloud (see figure 6.5A for an example). Thus, rather than momentum correlations, as expected for a uniform system, we will have *spatial* correlations for particles of opposite spin $m = \pm 1$. The correlations only exist, however, within the domains defined by those modes. Spatial correlations and their dynamics throughout the quench were the subject of an earlier work by our group (61), while the current work focuses on spatial mode characterization at the onset of the instability.

6.4.1 Uniform density

We first solve these equations for a uniform magnetic field, i.e., $B' = 0$, before turning to the inhomogeneous case. Then $p(x) = \mu B_0$, which can be easily removed from the equations by a gauge transformation, since the spin projection is a conserved quantity. Thus the homogeneous field case is simply one where $p = 0$. For the data presented in this paper we exclusively study the regime very close to the phase transition, i.e., $-U \ll q < 0$.

The case of a uniform $m_F = 0$ density, $U =$ constant, is a useful point of reference since the solution can be analytically obtained. The energy spectrum in this case is

$$E_k = \sqrt{(\epsilon_k + q)(\epsilon_k + q + 2U)} \tag{6.4}$$

where $\epsilon_k = \hbar^2 k^2/(2M)$, $k = \pi/L \times n$, $n = 1, 2, 3, ...$, for excitations in a box of length $L = 2R_{TF}$, where R_{TF} is the axial Thomas-Fermi radius. The Bogoliubov eigenfunctions are box modes

$$\phi_n = \sqrt{\frac{2}{L}} \sin\left[\frac{n\pi}{L}(x + L/2)\right] \tag{6.5}$$

for $|x| < L/2$. For our parameters the ground state energy of the box $\epsilon_1 \sim 0.05$ Hz is negligible compared with our experimental resolution, so we can assume a quasi-continuous spectrum. Thus in the thermodynamic limit, for $q > 0$ all eigenvalues are real, while for $q < 0$ at least one eigenvalue becomes imaginary, defining an unstable mode. For short times after the quench, the amplitude of this unstable modes grows exponentially in time with a rate $\Gamma = |\mathrm{Im}(E_k)|/\hbar$. The *maximally unstable mode* is defined to be the one whose imaginary component is the largest, i.e., $\Gamma = \Gamma_{max}$. For $-U < q < 0$, maximizing Γ yields the mode

$$\phi_1 = \sqrt{\frac{2}{L}} \sin\left[\frac{\pi}{L}(x + L/2)\right] \tag{6.6}$$

It has a wavevector $k_{max} = \pi/L$, i.e. a wavelength twice the Thomas-Fermi length of the condensate. Neglecting the zero point energy, the corresponding instability rate is

$$\Gamma_{max} \approx |\sqrt{q(q+2U)}|/\hbar$$

6.4.2 Thomas-Fermi density profile

To solve the Bogoliubov Eqns. (6.3) in the inhomogeneous case, we expand u, v in the box basis (Eqn . (6.5)), which for $p = 0$, yields the matrix equation

$$\begin{pmatrix} H^0_{\mu\nu} & U_{\mu\nu} \\ -U_{\mu\nu} & -H^0_{\mu\nu} \end{pmatrix} \begin{pmatrix} u_\nu \\ v_\nu \end{pmatrix} = E \begin{pmatrix} u_\nu \\ v_\nu \end{pmatrix}$$

where the basis size was held to N elements, u_ν, v_ν are the box basis coefficients for $\nu = 1, 2, 3, ...N$, and a summation over ν is implied in the matrix product. In this basis, the matrix elements of the operators in Eqn. (6.3) are $H^0_{\mu\nu} = (\epsilon_\mu + q)\delta_{\mu\nu}$ and $U_{\mu\nu} = U_0 \int_{-L/2}^{L/2} \phi_\mu(1 - x^2/L^2)\phi_\nu dx$. The box eigenenergies are $\epsilon_\mu = \mu^2\epsilon_1$.

The numerical problem consisted of diagonalizing a square matrix of order $2N$, with N pairs of eigenvalues $E, -E$ corresponding to the pair of spin modes discussed earlier. For each value of q and given the values of ϵ_1, U_0, the eigenvalues and eigenvectors were found numerically using MATLAB. The routines were tested against the exact solutions, Eqns. (6.4) and (6.5), by fixing the density to be a constant. Typically, the ground state energy was found to converge to 10^{-5} using 150 basis elements. Unless otherwise stated, the parameters used were $U_0 = 96$ Hz and $\epsilon_1 = 0.0047$ Hz.

6.4.2.1 Unstable Modes

We first consider the case $q < 0$, where one or more eigenvalues were complex. The solutions E_n were sorted by the magnitude of their imaginary component, with $n = 1$ mode having the largest imaginary component, $n = 2$ the second largest, and so on. Figure 6.5A shows the numerically obtained solutions with $q = -4.2$ Hz, for the maximally unstable eigenvector, $n = 1$, as well as that of a less unstable eigenvector, $n = 6$. The boundaries of the plot are the Thomas-Fermi surface, $x = \pm R_{TF} = \pm 350\mu$m. The most striking feature is that the maximally unstable mode is localized near the center of the cloud, with a wavefunction resembling a Gaussian profile. This is to be contrasted with Eqn. 6.6. For larger n the number of nodes increased, as did the spatial domain over which the mode function was non-zero.

We can define the rms width of the spin domain described by these modes as

$$x_{rms} = \sqrt{\frac{\int |u(x)|^2 x^2 dx}{\int |u(x)|^2 dx}}$$

where the upper and lower limits of integration are the Thomas-Fermi surface, $\pm R_{TF}$, respectively. For the $n = 1$ mode, $x_{rms} = 0.05 R_{TF}$, nearly four times smaller than the homogeneous case, Eqn. 6.6, whose rms width is $0.18 R_{TF}$. Thus the inhomogeneous density profile had a profound effect on the instability, causing the nucleation of localized spin domains.

This tendency can also be envisioned by applying a local density approximation to the rate Eqn. (6.4), which reflects the inhomogeneous gain profile for the spin-exchange process. Since the $m_F = 0$ state is dynamically unstable for $q < 0$, excitations develop at a rate that depends upon the *local* value of its density, $c_2 n_0(x)$. Thus the spin domains become localized near the cloud center, where this rate is highest.

Another, equivalent way to view this is through consideration of how the instability amplifies spin noise, which can be represented in any basis. Using plane waves with momentum $\mathbf{p}$, for example, and if the system contained noise that was uniformly distributed at all spatial frequencies up to $p_{max}/\hbar = 2\pi/\xi_{sp}$, where $\xi_{sp} = 1.5\mu$m is the spin healing length, it would begin in a delocalized state where the average amplitude was roughly the

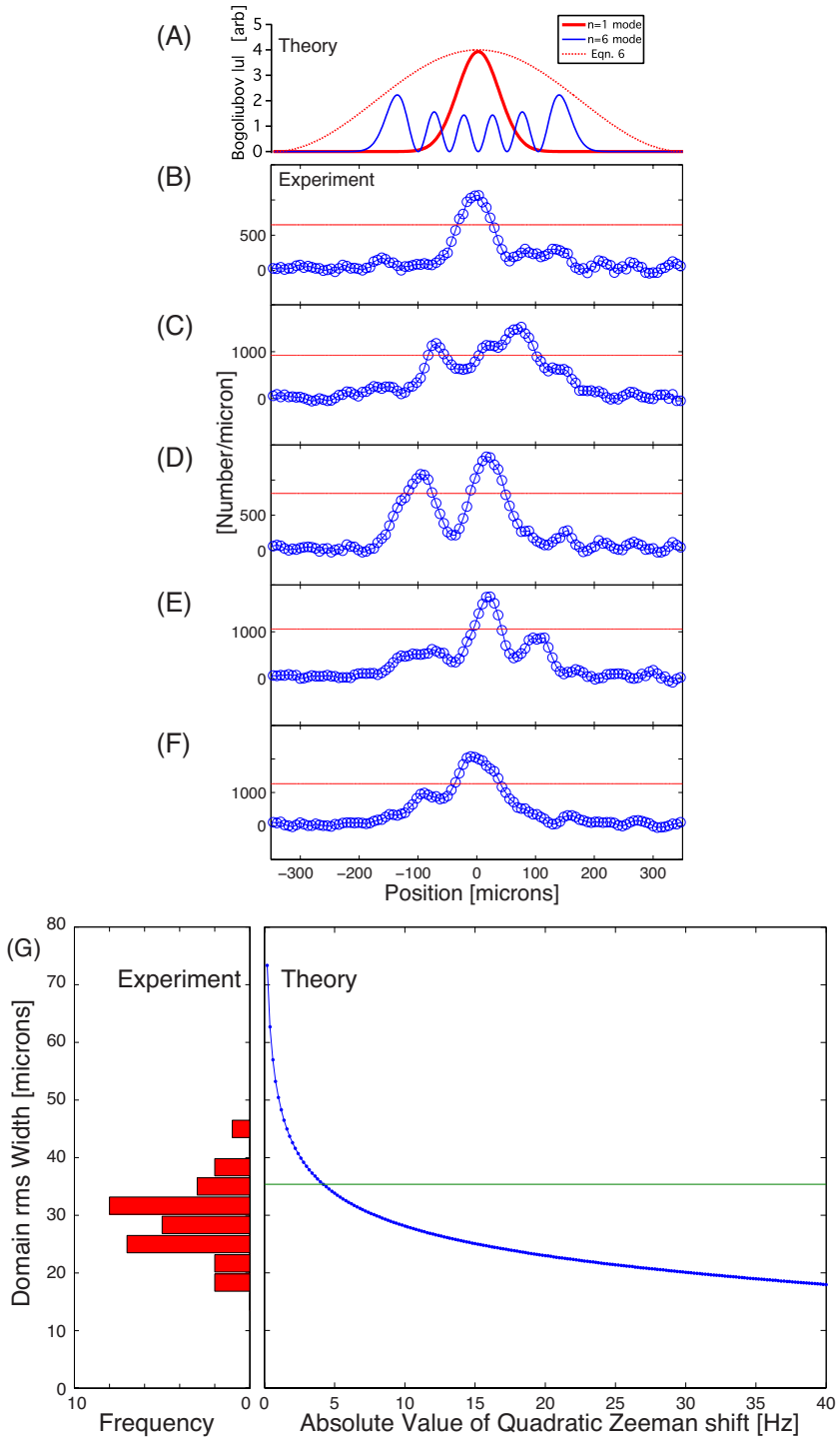

Figure 6.5: (Color Online). Unstable Modes and their spatial profiles. (A) Bogoliubov solutions for $U = 96$ Hz and $q = -4.2$ Hz. Shown are the probability distributions of the maximally unstable mode ($n = 1$, no nodes), a less unstable mode ($n = 6$, 5 nodes), and Eqn. (6.6). (B-F) Representative experimental observations of domains nucleated by the instability at $t = 20$ ms after the quench. Solid lines are the threshold used to determine rms domain sizes. (G) (right) Calculated rms width of the maximally unstable eigenvector versus distance to the phase transition point $-q$. (left) Histogram of the observed domains for 30 runs of the experiment at $q = -4.2$ Hz shows an average domain size that is smaller than that of the lowest mode, suggesting the involvement of higher lying modes $n > 1$.

same everywhere. This picture is consistent with the Truncated Wigner Approximation, as we discuss later. As time develops, only the particular superposition of momentum eigenstates that reproduces the state $u_1(x) \equiv u_{MAX}(x)$ shown in figure 6.5A would be amplified significantly, and the spin distribution would evolve into something that is spatially localized.

Indeed, our experimental data show that the instability creates spin structures that are spatially localized near the center of the Thomas-Fermi region (60). Figure 6.5, panels (B-G) shows experimentally measured mode profiles at the onset of the instability, $t = 20$ ms, when the mean population in the ± 1 states was 16%. We show 5 separate instances of the experimental quench sequence that are representative of the variations observed. Shot to shot fluctuations reflected the stochastic dynamics associated with the instability, where one or more domains were observed near the cloud center. By observing peaks in the data, we could determine the rms size of domains associated with those peaks. We accomplished this by measuring the spatial coordinates at which the data, which measures the particle density $\propto |u|^2$, crossed a threshold value $= e^{-1/2}$ of the peak value, as would be expected for a Gaussian function $u(x) = u_0 e^{-\frac{x^2}{4x_{rms}^2}}$. The threshold is shown as a solid line in the plots. These domains appear qualitatively similar to the maximally unstable mode profile in panel (A), but it is clear that higher order modes are required in order to explain the formation of multiple domains and the narrowest structures that are observed. At this value of q roughly 30 modes have an imaginary component, and thus single-mode dynamics do not tell the whole story.

Figure 6.5(G) explores the multi-mode nature of the instability by comparing the domain widths quantitatively. On the right panel we have computed the rms width of the maximally unstable mode, $u_{MAX}(x)$, versus the final quadratic Zeeman shift q (data are plotted versus $-q$). On the left panel we show a histogram of the observed rms sizes of the domains for 30 runs of the experiment at $q = -4.2$ Hz. There is a good correspondence between the range of domain sizes observed ($15 - 45\mu$m) and $x_{rms} = 35\mu$m for $u = u_{MAX}$, which is the horizontal line on the right panel. Our conclusion is that higher modes must play a role, and would shift the measured distribution to smaller values than the rms width of

u_{MAX}, since unstable modes with $n > 1$ contain higher spatial frequencies. The tail in the distribution at higher domain sizes is likely to be caused by mistaken identification of multiple overlapping domains as a single, larger domain, an example of which is shown in panel (C).

We can separate the temporal dynamics into two phases. First, there is a growth phase, during which the population fraction in ± 1, $f_{\pm 1}$, increases with time, but always remains small compared to that of the $m_F = 0$ state, f_0. Bogoliubov theory can be used to study the growth phase dynamics. The second, dynamical phase, occurs when all 3 components, f_{+1}, f_{-1}, f_0, have the same order of magnitude, and interact strongly with one another. The dynamical phase is not captured by the Bogoliubov theory, but can be observed experimentally.

The upper panel of figure 6.6 shows this crossover from growth to dynamical phases. For this figure we have taken an ensemble *average* of density profiles, which suppresses the stochastic variations and allows us to observe the broader trends in the dynamics. Experimental data was averaged over 3 shots, and two curves are shown at each time step (time increases from the bottom of the graph to the top). The blue curve is the experimental data normalized to its peak value at each time step, with each curve displaced by 1 for clarity. A 25 point moving average filter applied to the same data is shown in red. This filter removes both technical artifacts (residual optical interference fringes seen most clearly in the lowest trace) as well as much of the domain structure, revealing the broader features of the data. For short times, when the Bogoliubov theory is still applicable, the density profile grows from the center of the cloud, forming a localized hump at a time when $f_{pm} \approx 0.1$. As time increases, the fraction in $m_F = 0$ (not shown) becomes depleted in the same region of space, forming a localized dip. For $f > 0.16$ the system rapidly evolves into the dynamical phase, where the non-equilibrium behavior is best described by a complex interplay between humps and dips in two interpenetrating quantum fluids, $m_F = 0$ and $m_F = \pm 1$. For longer times the ± 1 clouds separate as well, forming a three component fluid that is locally magnetized (61). For $f_{\pm} > 0.5$, the distribution's center of mass appears to become negative; however, this is an artifact caused by center-of-mass motion of the entire

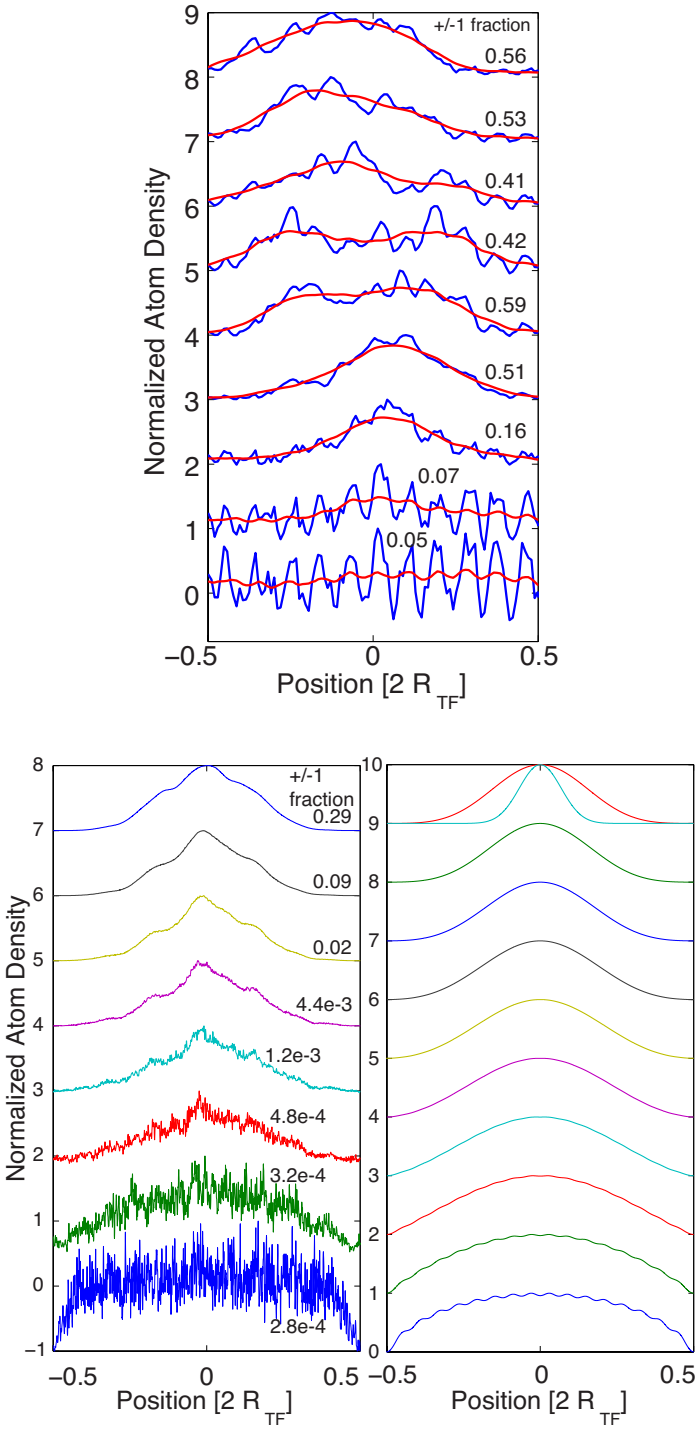

Figure 6.6: (Color Online). Average density profiles. Upper panel shows, from bottom to top, experimental traces for the $m_F = -1$ state averaged over 3 shots, for times $t = 12$ to 44 ms after the quench in 4 ms intervals. Corresponding fraction of atoms in the ± 1 is written above each curve. Average density profiles from numerical simulations are shown on lower left. Bogoliubov theory, Eqn. (6.2) is shown on lower right, for times $t/\tau_{MAX} = 1, 2, ...10$, with the maximally unstable eigenvector, $|u_{MAX}|^2$, shown in the uppermost graph for comparison. Here $\tau_{MAX} = 1/\mathrm{Im}(E_{MAX})$ is the time scale associated with u_{MAX}. In all 3 panes, each curve has been normalized to its peak value and displaced for clarity of presentation.

condensate.

The lower panel of figure 6.6 shows theoretical simulations of the dynamics during the growth phase. On the right pane is shown the prediction for the ensemble averaged density profile from Bogoliubov theory, eqn. (6.2), using only the modes that have a complex eigenvalue E_k. The curves have been normalized in the same manner as for the experiment.

On the left we show the result of numerical simulations of the 3 coupled spinor Gross-Pitaevskii (GP) equations seeded with noise according to the Truncated Wigner Approximation, or TWA (61). The TWA simulations are expected to be valid for both short and long times, as long as the initial condition is a classical state (54; 55; 56; 73). To implement these simulations, as discussed in (61), we assumed a BEC initially at zero temperature and obtained the initial wavefunction for the $m_F = 0$ component numerically. Vacuum noise in the $m_F = \pm 1$ states was simulated as classical noise, and we computed the average density, $\langle \psi_m^\dagger \psi_m \rangle$, as an ensemble average over 30 separate simulations using different random initial conditions. Vacuum modes with wavelength less than ξ_{spin} are not expected to contribute to the spin instability. Therefore, we imposed a cutoff energy of $c_2 n_0$, which resulted in $N_v \simeq$700 virtual particles, while the condensate contained 5×10^6 particles, similar to the experimental conditions. To study the early time behavior in the simulations it was also essential to subtract a constant from the average density $= N_v/(2R_{TF})$ equivalent to the sum of all virtual particles added, which was done according to the Weyl representations of the field operators (55).

Both Bogoliubov and full numerical theories agree with one another during the growth phase of the dynamics. Moreover, the theory confirms the local density picture discussed earlier, where a uniform distribution eventually becomes localized near the cloud center. For the Bogoliubov results the time dependence of mode k is $e^{\Gamma_k t}$, where $\Gamma_k = \mathrm{Im(E_k)}$ is the imaginary part of the eigenvalue. Near $t = 0$ this factor is ≈ 1 for all modes, resulting in a uniform density profile that vanishes only near the Thomas-Fermi radius. This phase of the dynamics is difficult to observe experimentally, as the number of atoms in $m_F = \pm 1$ is very low. At later times the maximally unstable mode, Γ_{MAX}, begins to dominate, and the curves begin to peak around this mode function, u_{MAX}. Even at a time $t = 10/\Gamma_{MAX}$,

however, the uppermost plot shows that the convergence to u_{MAX} is not yet complete. The experimental data shows the formation of the localized structure, but not its precursor, the uniform phase, which is hidden in experimental noise. The uniform phase is, however, captured by the TWA simulations (see the lowest traces of the left panel).

An interesting artifact in the simulations can also be observed in figure 6.6, one which illustrates some of the limitations of the Bogoliubov analysis. The TWA initial condition was taken to be a sum of Bogoliubov eigenmodes prior to the quench (see the next section for details of these modes), with random coefficients. Since these modes are defined on $x \in [-R_{TF}, +R_{TF}]$, their amplitude goes exactly to zero at the Thomas-Fermi radius. However, the numerical simulations are not restricted to the Thomas-Fermi volume, but capture the full details of the cloud's surface structure, even for $|x| > R_{TF}$. Thus at short times in the simulation, the repulsive interaction between atoms redistributed the $m_F = \pm 1$ density from inside to outside of R_{TF} such that as x approached $\pm R_{TF}$ from within the cloud, the Weyl correction was no longer accurate and yielded a negative density, seen in the lowest traces. Therefore, at short times the $m_F = \pm 1$ density should be even more uniform than the simulation suggests. This artifact had no bearing on the simulation at longer times, since the Weyl correction, which counts only the vacuum fluctuations, was insignificant in comparison with the number of real particles. Nonetheless, it illustrates the difficulty in describing the details of the dynamics near the Thomas-Fermi surface.

Finally, an agreement between all 3 density profiles–the experimental data, TWA simulations, and Bogoliubov theory–was found at a time approaching the crossover from growth phase to dynamical phase. This data is shown in figure 6.7. The experiment and TWA curves were taken at a time when the ± 1 fractions were similar, having reached $f_{\pm 1} = 0.16$ and 0.17, respectively. This allowed us to circumvent a factor of 4 difference observed in the absolute timescale for the quench dynamics between the two, as noted in (61). These data contain residual oscillations due to imperfect averaging. The Bogoliubov theory was taken at a time $t = 10\tau_{MAX}$. All 3 curves are narrower than the Thomas-Fermi density profile, which is shown for comparison, but broader than the maximally unstable eigenmode u_{MAX}.

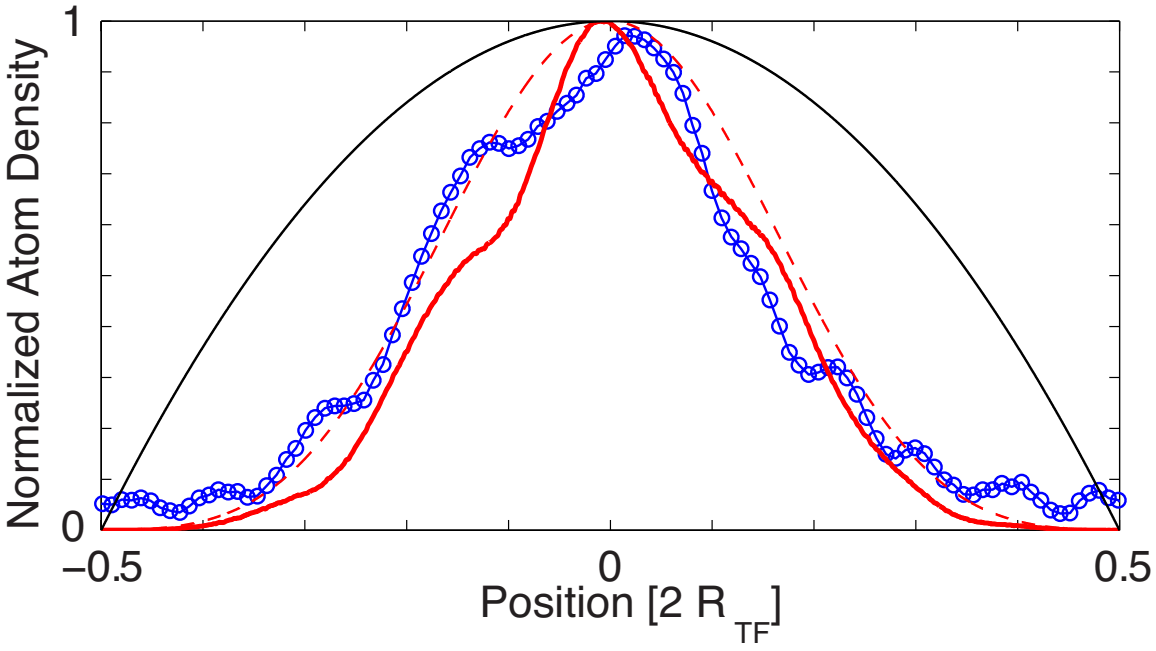

Figure 6.7: (Color Online). Agreement between experiment and theory. Average densities measured in the experiment (open circles), simulation (thick red line), and Bogoliubov theory (dashed line). Distributions were narrower than the Thomas-Fermi density profile (thin black line).

We observed that the convergence of the Bogoliubov theory to u_{MAX} was not complete until a time $t \approx 100\Gamma_{MAX}$ in the experiment. By this time the $m_F = 0$ cloud would have been significantly depleted, violating the Bogoliubov approximation. This provides further confirmation that our experiment is in a multi-mode regime even during its growth phase, when Bogoliubov theory is valid.

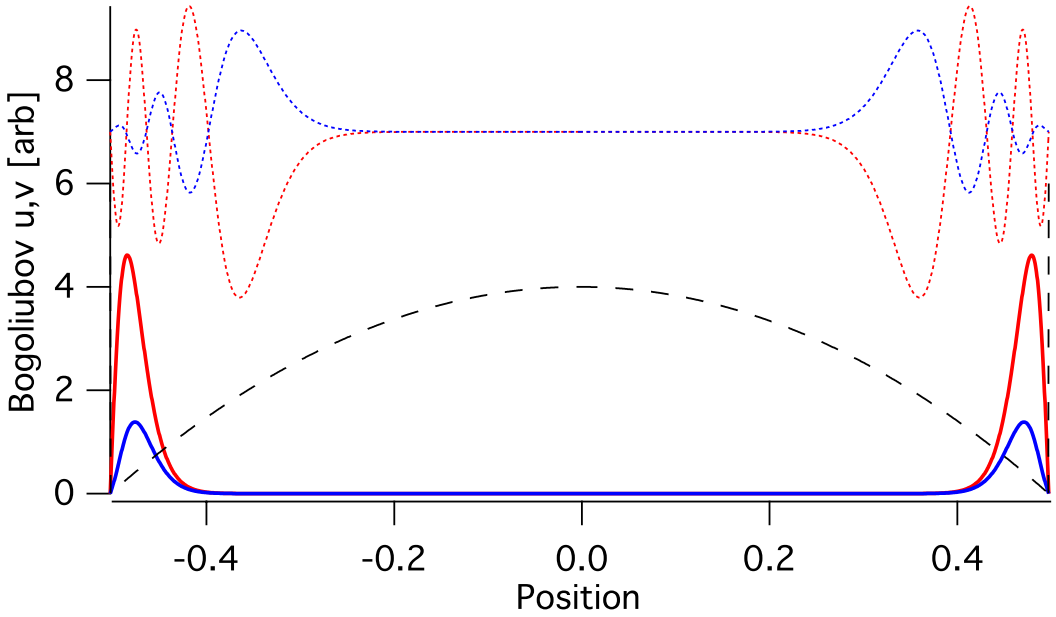

Figure 6.8: (Color Online). Stable modes for the Thomas-Fermi density profile, whose repulsive potential is shown as a black dashed line. Upper graph shows stable Bogoliubov functions $u(x)$ (red) and $v(x)$ (blue) for $q = +5$ Hz, $U = 96$ Hz. Shown is the mode with lowest energy ($n = 1$, solid lines) and a higher excitation mode ($n = 9$, dotted lines). The latter are offset for clarity.

6.4.2.2 Stable Modes

For $q > 0$ the Bogoliubov theory yields the collective excitation spectrum of the stable $m_F = 0$ ground state. Here the eigenvalues are all real and positive, and n is a mode index by which they are sorted in increasing order. Similar to the unstable modes discussed in the previous section these modes also depart from the homogeneous Bogoliubov solutions, equation (6.5). Their spatial profile also depends upon q in a manner that is determined numerically.

The upper panel of figure 6.8 shows the numerically obtained mode functions, $u_1(x)$ and

$v_1(x)$, for the lowest energy eigenvalue E_1, at a quadratic Zeeman shift of $q = +5$ Hz. These functions are sharply localized near the Thomas-Fermi boundary at $x/L_{TF} = \pm 1/2$, in stark contrast with the homogeneous modes that are delocalized throughout the Thomas-Fermi region. For increasing n the modes penetrate further into the cloud–for comparison,the $n = 9$ mode, with even parity, is shown. Modes with odd parity have higher energy than those with even parity; however, for low n the difference in energy was observed to be negligible. In this case, since the wavefunctions are localized near the edge of the cloud, both even and odd states have nearly the same overlap with the density profile $U(x)$. Thus Eqns. (6.3) result in a "parity doublet" of eigenvalues for low n, an effect that we discuss later.

We can understand the mode structure for $q > 0$ in terms of the total potential appearing in the Bogoliubov equations:

$$U(x) = c_2 n_0(x) = c_2 n_0 \left(1 - \frac{x^2}{R^2}\right)$$

where n_0 is the density averaged over the 2 radial directions of the optical trap. Beyond the Thomas-Fermi radius we can set $U(x) = \infty$, since the harmonic potential increases very rapidly in comparison with the energy scale $c_2 n_0$. Figure 6.5 shows $U(x)$ as a dashed line. It resembles the box potential obtained in the homogeneous case, but with an additional bump at $x = 0$ that shifts the excitations away from the cloud center and toward the Thomas-Fermi boundary. This repulsion arises due to antiferromagnetism–for $c_2 > 0$ the spin $m_F = 0$ and spin $|m_F| = 1$ quantum fluids repel one another. Since the excitations are ± 1 atom pairs, their minimum energy configuration is a localized state at the edge of the cloud.

Crossing the phase transition results in a transformation from stable to unstable behavior of the eigenmode. This effect is explored in figure 6.9 for the lowest energy state. Only within a tiny region near the critical point, $q = -0.005$ Hz, with a width of 0.1 Hz, does the mode function become delocalized. By contrast, in the homogeneous case the mode $\sin \pi(x + L/2)/L$ remains the same on both sides of the phase transition, and is always maximum at $x = 0$.

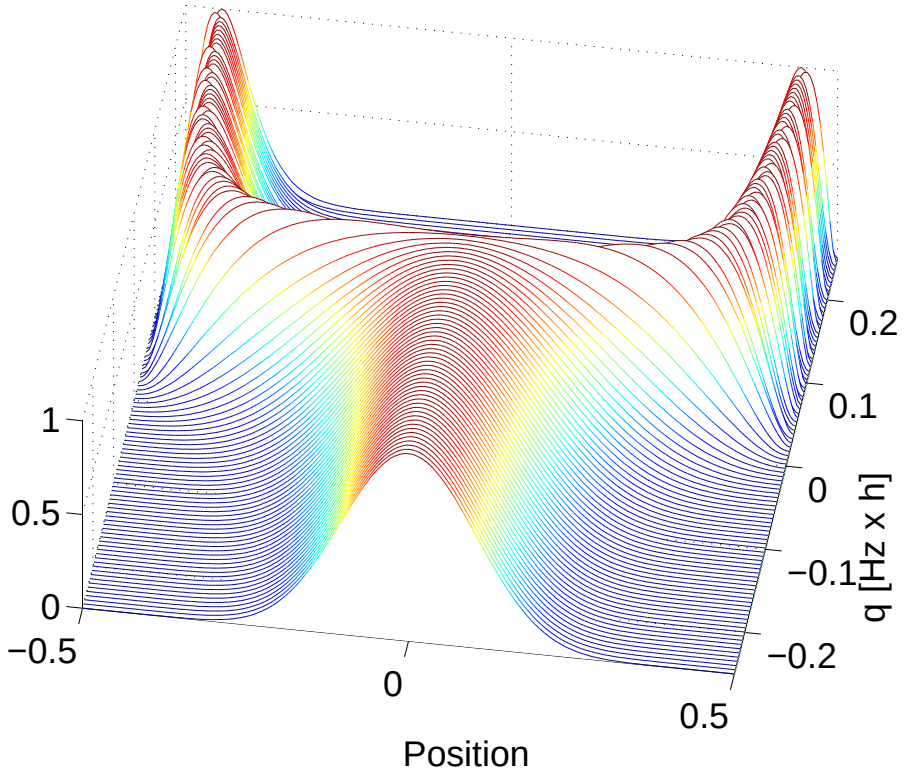

Figure 6.9: (Color Online). Transformation of the wavefunction caused by the instability. Shown is the numerically obtained function $|u(x)|^2$ for the lowest energy eigenvalue for 100 values of q near the phase transition point, $q_{crit} = -0.005$ Hz. The deviation of q_{crit} from 0 occurs due to the discreteness of the eigenvalues. The data are scaled to the peak value of $|u(x)|^2$ at each q for clarity of presentation. For positive q the excitation is localized at the Thomas-Fermi boundary of the $m_F = 0$ cloud, while for negative q it is localized in the cloud center. The transition from the boundary to the center of the cloud occurs very suddenly as q is changed–note that the entire span of q is only 0.4 Hz in the figure.

6.4.2.3 Eigenvalue Spectrum

The left panel of figure 6.10 shows the eigenvalue spectrum computed for $p = 0$, for $q = +5, 0$ and -5 Hz, corresponding to stable, critically stable and unstable regimes. The eigenvalue spectrum in the case of a homogeneous density gas at the same peak value of n_0 is plotted on the right panel for comparison. In both cases we have plotted the square of the energy eigenvalue, E^2, rather the eigenvalue E itself, since according to the Bogoliubov equations this quantity is always real for $p = 0$.

For positive q the graph shows that the lowest eigenvalue (the mode with index $n = 1$)

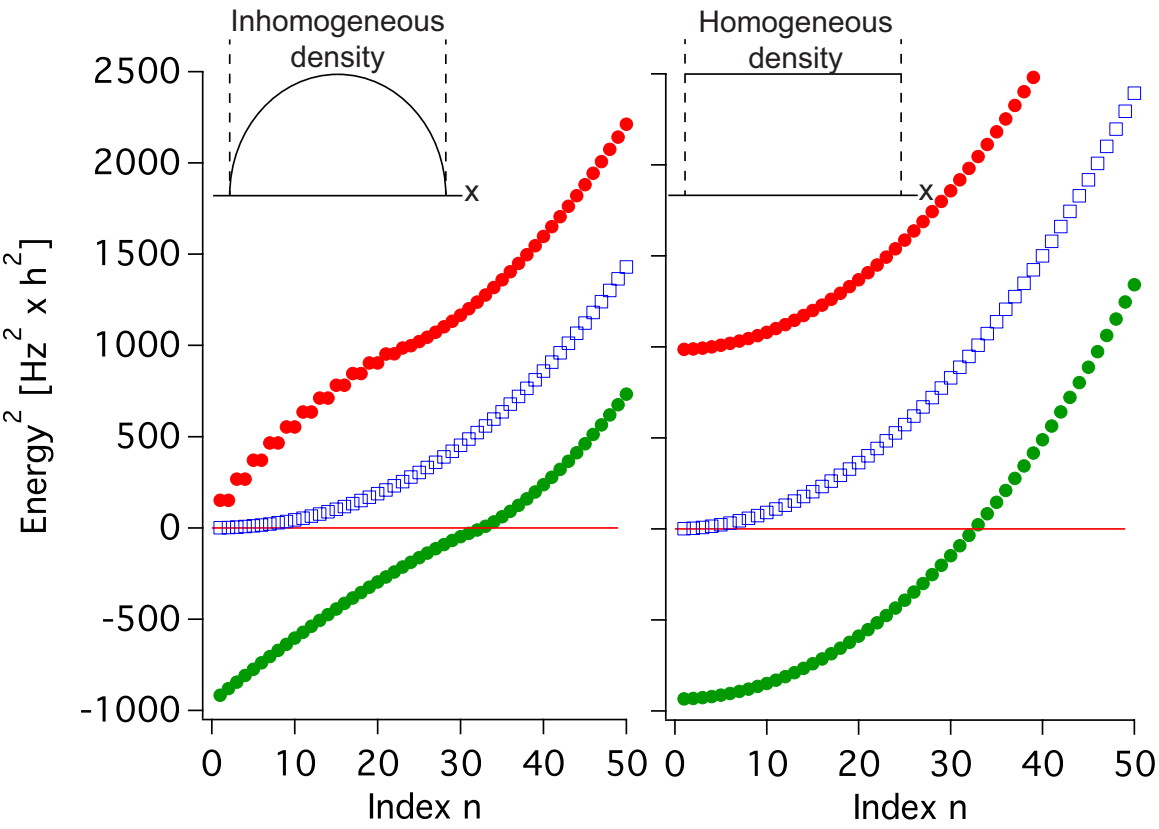

Figure 6.10: (Color Online). Numerically obtained Bogoliubov excitation energy spectrum. Shown is the *square* of the numerically obtained eigenvalues $E_n; n = 1, 2, 3, ...$ for (a) inhomogeneous density profile and (b) homogeneous density. Eigenvalues are plotted for q = + 5 Hz (upper,red), q = 0 (middle,blue) and q = - 5 Hz (lower,green). $E^2 < 0$ indicates an imaginary eigenvalue indicative of an instability. Notice that the number of imaginary eigenvalues increases as q becomes smaller.

is finite for both inhomogeneous and homogeneous densities, and thus the system always has an energy gap. For a homogeneous system this gap is given by

$$E_1 = \sqrt{(\epsilon + q)(\epsilon + q + 2U)}$$

where ϵ is the lowest box mode. For the parameters used, $E_1 = h \times 23$Hz. For the inhomogeneous case the numerical data show that the energy gap is reduced by a factor of ~ 3, to $h \times 8$Hz. As noted earlier, this mode is localized at the cloud edge, where it experiences a reduced overlap with the $m_F = 0$ spin states and therefore a smaller repulsive interaction energy.

For low n the dispersion relation–the variation of E with n–is considerably different

for low n in the two cases. For low n one can clearly see in the graph that each energy eigenvalue appears doubly degenerate. This is the "parity doublet" mentioned earlier, where symmetric and anti-symmetric wavefunctions both experience a negligible overlap with the inhomogeneous density profile. Note that there is no doublet in the homogeneous case. For higher lying modes, a transition can be seen in the dispersion relation from $E \sim n^{1/2}$ to $E \sim n$ behavior, where the wavefunction on the left half and right half of the cloud begin to overlap. This occurs when the total energy becomes comparable to the height of the "bump" $c_2 n_0(0) = 96$ Hz . For the parameters shown, this occurs at $n \sim 25$. For high n, and corresponding energies much larger than $2U$, the magnon excitations become comprised primarily of free particles for both homogeneous and inhomogeneous cases.

As q becomes smaller, the entire spectrum of E^2 shifts to smaller values, until the lowest eigenvalue reaches zero at a point very close (within ϵ) of $q = 0$, which defines the boundary of the unstable region. However, as we have plotted E^2 rather than E, the transition from stable to unstable regimes becomes a more smooth and continuous one, with the number of imaginary eigenvalues ($E^2 < 0$) increasing as q decreases. For example, at $q = -5$ Hz 32 eigenvalues have become imaginary, while for $n \geq 33$ they still remain real. Due to the tiny value of ϵ, it plays no role, and the phase transition occurs at the same point for both inhomogeneous and inhomogeneous cases.

Finally, we have also plotted $\mathrm{Im}(E)$ versus q earlier, in figure 6.2, for the maximally unstable eigenvector u_1, v_1. As this mode is localized near the cloud center, where the $m_F = 0$ density is maximal, the atoms experience a spin exchange collision rate that is virtually indistinguishable from that of a homogeneous system at the same *peak* density. Thus both homogeneous and inhomogeneous eigenvalues are very similar, and both show good agreement with our experimental data.

CHAPTER VII

CONCLUSION

The primary study of this thesis has been out-of-equilibrium dynamics near quantum phase transition in a spin-1 condensate. This investigation builds upon the success of previous studies on spinor physics [10,15,16,17,28,29,37]. The major contribution of this thesis has been accessing antiferromagnetic quantum phase transition in F=1 sodium condensate as well as developing the crucial theoretical understanding of the dynamics close to the phase transition point. The spinor Bose-Einstein condensates possess a vector order parameter with additional degrees of freedom. By changing external fields dynamically, we have observed and quantified a host of non-equilibrium phenomena, including spin domain formation and aggregation, spin-nematic waves and others. Understanding dynamics close to the quantum phase transition has required a review of several theoretical models of spin-mixing as well as extending these existing models. The modeling of spin-mixing in the presence of a finite magnetic field gradient has crucial to extending our understanding of dynamics near the phase transition. The relevance of such dynamics to topics such as quantum noise, quantum amplication, symmetry breaking and phase transitions has led to this study of the spin mixing instability in both single-mode and spatially extended sodium spinor Bose gas.

7.1 Antiferromagnetic Quantum Phase Transition

The ability to control the ground state of the spinor system using microwave dressing fields is central to this work. The quadratic energy shift q is usually a function of external magnetic field B through the second-order Zeeman effect. However, it can also be tuned through application of oscillating electromagnetic field. For instance, a quadratic energy shift for the $F = 1$ spinor gas is obtained using the ac Zeeman effect from a microwave drive tuned near the $|F = 1; m_f = 0\rangle \rightarrow |F = 2; m_f = 0\rangle$ hyperfine transition. By deterministically

controlling the oscillating electromagnetic field, we switch the ground state of the many-body system from spin 0 atoms to spin ± 1 atoms. The relative hyperfine energy levels are engineered using off-resonant radiofrequency or microwave radiation. In this state, the bare atomic states get replaced by eigenstates of the total atom-plus-field system. In our case the microwave field is relatively weak, such that the dressed states almost coincide with the bare atomic states and the level shifts can be calculated perturbatively. We have exploited this phenomenon to uncover polar to antiferromagnetic quantum phase transition in $F = 1$ ^{23}Na spinor Bose-Einstein condensates.

For the $F = 1$ ^{23}Na condensate, the spin-dependent interaction coefficient c_2 determines spin-changing collisions that can convert two $m_F = 0$ atoms into an $m_F = \pm 1$ pair and vice-versa. It determines the nature of the ground state - antiferromagnetic for $c_2 > 0$ or ferromagnetic for $c_2 < 0$. A key consequences of the spin-dependent collisional interactions is that the spin components can coherently exchange population in a process called spin-mixing. Two atoms with spin components $m_F = 1$ and $+1$ can collide and become two atoms with spin component $m_F = 0$ and vice-versa.

We trigger the spin mixing by instantaneouly quenching the system across the quantum phase transition from polar state to antiferromagnetic state. Following the quench, the pure mF = 0 condensate became unstable, evolving into a superposition of all 3 spinor components that preserved the overall zero net magnetization. The temporal evolution of the relative spinor populations following the quench was studied.

At positive q, the gas was relatively stable against spin relaxation, i.e. the creation of $m_F = \pm 1$ pairs. This stability is a characteristic of quantum antiferromagnetism. For a homogeneous system and $0 < q < c_2 n$ the $m_F = 0$ state is stabilized against the creation of magnon excitation (spin waves) by an energy gap which is a function of both q and wavevector k. The $k = 0$ mode was the most unstable mode. As $q \to 0$, the quantum fluctuations destabilized the pure spin 0 condensate. The calculations using Bogoliubov theory predict that the fraction of atoms should reach order 1 within 1.5 seconds. This is similar to what we saw in the experiment, indicating a good match of the exprimental results with theory. However, other mechanisms including themal fluctuations could not be

definitely ruled out. For the range of q explored in this work, the instability was observed to create a mixed state of all 3 components which appeared to be metastable on a timescale much longer than Γ^{-1}.

We map our results to the quantum rotor model. A pure $m_F = 0$ state is represented by $\theta = 0$ in the quantum rotor model, while $0 < \theta < n$ represents a state where a fraction of the atoms are in $m_F = \pm 1$ state. The sudden quench transition from $q > 0$ to $q < 0$ causes V to change sign, resulting in rapid dispersion of a wavepacket initially highly localized in angle near $\theta = 0$. The resulting wavepacket dynamics are mostly classical in character and consist of a rapid dispersion in followed by sparse, periodic revivals at time t_rev. The quantum rotor model is valid in single mode approximation and cannot describe spin domain formation. Hence, the quantum rotor model cannot explain data for small $|q|$, for which spin segregation occurs. However, the model was used to understood the behavior for short time scales following the quench for larger $|q|$, where a mixture of 3 components is observed to occur.

The instability rate close the quantum phase transition point was modeled using Bogoliubov theory. The maximum instability for $-c_2 n_0 < q < 0$ is predicted to correspond to the $k = 0$ wavevector i.e. a homogeneous rate of pair formation throughout the cloud. The homogeneous theory is in considerable disagreement with our data, which could be attributed to the finite size and 1-D geometry of our trap.

In order to understand the domain formation using Bogoliubov theory, we describe the growth rate of $m_F = \pm 1$ atom pair number for $q < 0$ using local density approximaion. In this model, the maximum gain is expeced to occur at the cloud center. In this regime,the inhomogeneous gain acts as a nonlinear spatial mode coupler that converts energy from long to short wavelengths, i.e. exhibits a tendency to nucleate small sized domains. These dynamics are not captured in the homogeneous theory, but appear in our data. For data sets with $q < h \times 7Hz$, the $m_F = 1$ atom distribution appeared initially as one or more small axial domains near the cloud center. Domains coalesce into a larger domain that grew in size with time until it became comparable to the axial Thomas-Fermi radius. Once a substantial number of atom pairs have been created the $m_F = 0$ condensate can be locally

depleted. Since the $m_F = 1$ and $m_F = 0$ clouds are immiscible for $c_2 > 0$, this creates a potential well that traps the pairs but allows the domain to grow axially due to the continued effect of the instability (expansion along the radial direction costs a substantial kinetic energy due to the tighter confinement). Thus the long timescale evolution of the instability exhibits one-dimensional coarsening dynamics. We also observed smaller domain structures which could not be quantified clearly due to the presence of undamped $m_F = 0$ density fluctuations in the initial state caused by nonadiabaticity in the initial transfer to the optical trap.

7.2 Spinor Correlations

Following the studies of population dynamics near the transition point, we investigate the spatiotemporal evolution through two particle correlations between atoms in each pair of spin states. The experimental set-up in this case is distinguished from the one described earlier, by cancelling of magnetic field gradient. This allowed resolution of the spin 1 atoms to precise location enabling two partial spatiotemporal correlation study in the condensate. Our investigations revealed dramatic differences between the dynamics of the spin correlations and those of the spin populations. In order to determine if domain formation was stochastic in nature, multiple images of the condensate was taken for a given q_{final} and hold time t. The average of these images was evaluated for different hold time and q_{final} to determine if there was any pattern behind the domain formation. The average did not show any structure indicating that the domain formation was stochastic in nature.

We also studied rich non-equilibrium behavior in the form of growth and decay of both nematic and magnetic spin waves. Following the quench the distinct regions in the condensate are expected to communicate with one another through the propagation of spin waves, as time evolves. The decay of local correlation between spin +1 and -1 indicated a destructive interference between waves originating from different points in space. Interference effects have also been recently reported in quenched scalar superfuids, leading to oscillations in the density-density correlation function. The initial spin density uctuations were amplified, and ultimately, macroscopic, one-dimensional spatial domains were

observed to have formed. In order to gain a theoretical understanding, the three spin states were simulated through coupled spinor Gross-Pitaevskii equations. The vacuum noise in the $m_F = 1$ state was simulated as classical noise according to the truncated Wigner approximation. The idea of the method is to generate an ensemble of classical fields which samples the Wigner function of the initial thermal density operator, and to evolve each field with the Gross-Pitaevskii equation (GPE). Like other existing approximate methods, such as the time-dependent Bogoliubov approach, it allows us to go beyond the commonly used Gross-Pitaevskii equation, in which the interactions between the condensate and the noncondensed atoms are neglected. The experimental results show qualitative similarity with with our theoretical simulations. The simulations revealed that even in the absence of thermal or technical noise, vacuum fluctuations can induce a decay of correlations.

7.3 Linear Zeeman Correction

A key feature of this work is inclusion of magnetic field inhomogeneities that smooth the phase transition. Once these were removed, we observed a dramatic sharpening of the transition point, which could then be resolved within a quadratic Zeeman shift of only 1-2Hz. We find contrary to intuition and to earlier observations of equilibrium properties in the positive q region, that the field gradient suppresses the tendency for the $m_F = 0$ condensate to phase separate into an $m_F = -1$ mixture. This suppression can be explained, however, by analyzing the unstable eigenmodes that are populated by the quench and uncovering, theoretically, their dependence upon p.

A central theme of our work is the use of dynamics to probe the phase transition through instabilties generated by a rapid quench. Simply by changing the quench parameters, we are able to map out the phase boundary. We do not need to probe the ground state of the system or wait for the equilibrium, as many early works on spinor gases have done. This greatly simplifies the experimental protocol, as the dynamics may be observed in the 10-100 ms, rather than 1-10 second range. We show that the rapid variation of the instability near the transition point can allow for a precise determination of the location.

7.4 Future Explorations

The experimental results described in this thesis all begin with a non-equilibrium spin dynamics triggered by quenching an unmagnetized spin-1 system through a quantum phase transition. This thesis has extended our theoretical understanding by investigating the spinor Hamiltonian as well as different models used to understand this system. The future work will focus on characterizing the spin waves, as well as exploring the phase coherence between the dynamically created $m_F = \pm 1$ spin components in relation to topological defect formation.

Bibliography

[1] M. Fisher, "Scaling, universality and renormalization group theory,", in *Critical Phenomena*, edited by F. Hahne volume 186 of *Lecture Notes in Physics* pp. 1–139 Springer Berlin Heidelberg 1983.

[2] S. Sachdev, *Quantum phase transitions* (Cambridge University Press, Cambridge ; New York, 1999).

[3] T. W. B. Kibble, "Topology of cosmic domains and strings," *Journal of Physics A: Mathematical and General* **9**, 1387 (1976).

[4] W. H. Zurek, "Cosmological experiments in condensed matter systems," *Phys. Rep.* **276**, 177 (1996).

[5] A. Vilenkin and E. P. S. Shellard, *Cosmic strings and other topological defects*Cambridge monographs on mathematical physics (Cambridge University Press, Cambridge, 1994).

[6] K. Rajagopal and F. Wilczek, "Emergence of Coherent Long-Wavelength Oscillations after a Quench - Application to Qcd," *Nucl Phys B* **404**, 577 (1993).

[7] B. Berdnikov and K. Rajagopal, "Slowing out of equilibrium near the QCD critical point," *Phys Rev D* **61**, 105017 (2000).

[8] A. Bray, "Theory of phase-ordering kinetics," *Advances in Physics* **43**, 357 (1994).

[9] A. Polkovnikov, K. Sengupta, A. Silva, and M. Vengalattore, "Colloquium: Nonequilibrium dynamics of closed interacting quantum systems," *Reviews of Modern Physics* **83**, 863 (2011).

[10] A. Lamacraft and J. Moore, "Potential Insights into Non-equilibrium Behavior from Atomic Physics,", in *Ultracold Bosonic and Fermionic Gases (Contemporary Concepts of Condensed Matter Science)*, edited by K. Levin, A. Fetter, and D. M. Stamper-Kurn Elsevier 2012.

[11] P. Calabrese and J. Cardy, "Time dependence of correlation functions following a quantum quench," *Physical Review Letters* **96**, 136801 (2006).

[12] J. A. Lipa, J. A. Nissen, D. A. Stricker, D. R. Swanson, and T. C. P. Chui, "Specific heat of liquid helium in zero gravity very near the lambda point," *Physical Review B* **68**, 174518 (2003).

[13] L. Pitaevskii and S. Stringari, *Bose-Einstein condensation*International Series of Monographs on Physics (Clarendon Press, Oxford, 2003).

[14] M. J. H. Ku, A. T. Sommer, L. W. Cheuk, and M. W. Zwierlein, "Revealing the Superfluid Lambda Transition in the Universal Thermodynamics of a Unitary Fermi Gas," *Science* **335**, 563 (2012).

[15] D. M. Stamper-Kurn, M. R. Andrews, A. P. Chikkatur, S. Inouye, H.-J. Miesner, J. Stenger, and W. Ketterle, "Optical confinement of a Bose-Einstein condensate," *Physical Review Letters* **80**, 2027 (1998).

[16] J. Stenger, S. Inouye, D. M. Stamper-Kurn, H.-J. Miesner, A. P. Chikkatur, and W. Ketterle, "Spin domains in ground-state Bose-Einstein condensates," *Nature* **396**, 345 (1998).

[17] S. Inouye, M. R. Andrews, J. Stenger, H.-J. Miesner, D. M. Stamper-Kurn, and W. Ketterle, "Observation of Feshbach resonances in a Bose-Einstein condensate," *Nature* **392**, 151 (1998).

[18] H.-J. Miesner, D. M. Stamper-Kurn, J. Stenger, S. Inouye, A. P. Chikkatur, and W. Ketterle, "Observation of metastable states in spinor Bose-Einstein condensates," *Physical Review Letters* **82**, 2228 (1999).

[19] D. M. Stamper-Kurn, H.-J. Miesner, A. P. Chikkatur, S. Inouye, J. Stenger, and W. Ketterle, "Quantum tunneling across spin domains in a Bose-Einstein condensate," *Physical Review Letters* **83**, 661 (1999).

[20] J. Kronjäger, C. Becker, M. Brinkmann, R. Walser, P. Navez, K. Bongs, and K. Sengstock, "Evolution of a spinor condensate: Coherent dynamics, dephasing, and revivals," *Phys. Rev. A* **72**, 063619 (2005).

[21] J. Kronjäger, C. Becker, P. Navez, K. Bongs, and K. Sengstock, "Magnetically Tuned Spin Dynamics Resonance," *Phys. Rev. Lett.* **97**, 110404 (2006).

[22] A. T. Black, E. Gomez, L. D. Turner, S. Jung, and P. D. Lett, "Spinor Dynamics in an Antiferromagnetic Spin-1 Condensate," *Physical Review Letters* **99**, 070403 (2007).

[23] L. E. Sadler, J. M. , S. R. Leslie, M. Vengalattore, and D. M. Stamper-Kurn, "Spontaneous symmetry breaking in a quenched ferromagnetic spinor Bose-Einstein condensate," *Nature* **443**, 312 (2006).

[24] F. Gerbier, A. Widera, S. Fölling, O. Mandel, and I. Bloch, "Resonant control of spin dynamics in ultracold quantum gases by microwave dressing," *Phys. Rev. A* **73**, 041602 (2006).

[25] S. R. Leslie, J. Guzman, M. Vengalattore, J. D. Sau, M. L. Cohen, and D. M. Stamper-Kurn, "Amplification of fluctuations in a spinor Bose-Einstein condensate," *Physical Review A* **79**, 043631 (2009).

[26] M. H. Anderson, J. R. Ensher, M. R. Matthews, C. E. Wieman, and E. A. Cornell, "Observation of Bose-Einstein Condensation in a Dilute Atomic Vapor," *Science* **269**, 198 (1995).

[27] K. B. Davis, M. O. Mewes, M. R. Andrews, N. J. van Druten, D. S. Durfee, D. M. Kurn, and W. Ketterle, "Bose-Einstein Condensation in a Gas of Sodium Atoms," *Phys. Rev. Lett.* **75**, 3969 (1995).

[28] C. C. Bradley, C. A. Sackett, J. J. Tollett, and R. G. Hulet, "Evidence of Bose-Einstein Condensation in an Atomic Gas with Attractive Interactions," *Phys. Rev. Lett.* **75**, 1687 (1995).

[29] C. C. Bradley, C. A. Sackett, and R. G. Hulet, "Bose-Einstein Condensation of Lithium: Observation of Limited Condensate Number," *Phys. Rev. Lett.* **78**, 985 (1997).

[30] D. S. Naik, *Bose-Einstein Condensation: Building the Testbeds to Study Superfluidity*, PhD thesis Georgia Institute of Technology 2006.

[31] D. S. Naik and C. Raman, "Optically plugged quadrupole trap for Bose-Einstein condensates," *Phys. Rev. A* **71**, 033617 (2005).

[32] D. S. Naik, S. R. Muniz, and C. Raman, "Metastable Bose-Einstein condensate in a linear potential," *Phys. Rev. A* **72**, 051606 (2005).

[33] D. A. Steck, "Sodium 23 D Line Data," (2003).

[34] W. Ketterle, K. B. Davis, M. A. Joffe, A. Martin, and D. E. Pritchard, "High-Densities of Cold Atoms in a Dark Spontaneous-Force Optical Trap," *Physical Review Letters* **70**, 2253 (1993).

[35] A. Keshet and W. Ketterle, "A distributed, graphical user interface based, computer control system for atomic physics experiments," *Review of Scientific Instruments* **84**, (2013).

[36] T.-L. Ho, "Spinor Bose Condensates in Optical Traps," *Phys. Rev. Lett.* **81**, 742 (1998).

[37] T. Ohmi and K. Machida, "Bose-Einstein Condensation with Internal Degrees of Freedom in Alkali Atom Gases," *Journal of the Physical Society of Japan* **67**, 1822 (1998).

[38] D. Belkic, *Principles of Quantum Scattering Theory* (Institute of Physics Publishing, Bristol and Philadelphia, 2004).

[39] L. Landau and E. Lifshits, *Quantum Mechanics: Non-relativistic Theory*Butterworth Heinemann (Butterworth-Heinemann, 1977).

[40] C. J. Foot, *Atomic Physics (Oxford Master Series in Atomic, Optical and Laser Physics)*, 1 ed. (Oxford University Press, USA, 2005).

[41] Y. Kawaguchi and M. Ueda, "Symmetry classification of spinor Bose-Einstein condensates," *Phys. Rev. A* **84**, 053616 (2011).

[42] M. Koashi and M. Ueda, "Exact Eigenstates and Magnetic Response of Spin-1 and Spin-2 Bose-Einstein Condensates," *Phys. Rev. Lett.* **84**, 1066 (2000).

[43] W. Zhang, S. Yi, and L. You, "Mean field ground state of a spin-1 condensate in a magnetic field," *New Journal of Physics* **5**, 77 (2003).

[44] Y. Kawaguchi and M. Ueda, "Spinor Bose-Einstein condensates," *Physics Reports* **520**, 253 (2012).

[45] M.-O. Mewes, M. R. Andrews, D. M. Kurn, D. S. Durfee, C. G. Townsend, and W. Ketterle, "Output Coupler for Bose-Einstein Condensed Atoms," *Phys. Rev. Lett.* **78**, 582 (1997).

[46] D. M. Stamper-Kurn, *Peeking and poking at a new quantum fluid: Studies of gaseous Bose-Einstein condensates in magnetic and optical traps*, Ph.d. thesis MIT 1999.

[47] C. Cohen-Tannoudji, J. Dupont-Roc, and G. Grynberg, "Atom-Photon Interactions," (1992).

[48] H. Stapelfeldt and T. Seideman, "Colloquium: Aligning molecules with strong laser pulses," *Reviews of Modern Physics* **75**, 543 (2003).

[49] P.-G. de Gennes and J. Prost, *The Physics of Liquid Crystals* (Clarendon Press, 1995).

[50] H. H. Chen and P. M. Levy, "Quadrupole Phase Transitions in Magnetic Solids," *Phys. Rev. Lett.* **27**, 1383 (1971).

[51] S. Fujimoto, "Spin Nematic State as a Candidate of the Hidden Order Phase of URu_2Si_2," *Phys. Rev. Lett.* **106**, 196407 (2011).

[52] L. W. Harriger, H. Q. Luo, M. S. Liu, C. Frost, J. P. Hu, M. R. Norman, and P. Dai, "Nematic spin fluid in the tetragonal phase of $BaFe_2As_2$," *Phys. Rev. B* **84**, 054544 (2011).

[53] D. Stamper-Kurn and U. M., *eprint:arXiv.org/abs/1205.1888* (2012).

[54] P. Blakie, A. Bradley, M. Davis, R. Ballagh, and C. Gardiner, "Dynamics and statistical mechanics of ultra-cold Bose gases using c-field techniques," *Advances in Physics* **57**, 363 (2008).

[55] A. Polkovnikov, "Phase space representation of quantum dynamics," *Ann Phys-New York* **325**, 1790 (2010).

[56] J. D. Sau, S. R. Leslie, D. M. Stamper-Kurn, and M. L. Cohen, "Theory of domain formation in inhomogeneous ferromagnetic dipolar condensates within the truncated Wigner approximation," *Physical Review A* **80**, 023622 (2009).

[57] E. M. Bookjans, C. D. Hamley, and M. S. Chapman, "Strong Quantum Spin Correlations Observed in Atomic Spin Mixing," *Physical Review Letters* **107**, 210406 (2011).

[58] P. C. Hohenberg and B. I. Halperin, "Theory of Dynamic Critical Phenomena," *Reviews of Modern Physics* **49**, 435 (1977).

[59] D. Jaksch, C. Bruder, J. I. Cirac, C. W. Gardiner, and P. Zoller, "Cold Bosonic Atoms in Optical Lattices," *Physical Review Letters* **81**, 3108 (1998).

[60] E. M. Bookjans, A. Vinit, and C. Raman, "Quantum Phase Transition in an Antiferromagnetic Spinor Bose-Einstein Condensate," *Physical Review Letters* **107**, 195306 (2011).

[61] A. Vinit, E. M. Bookjans, C. A. R. S de Melo, and C. Raman, "Antiferromagnetic Spatial Ordering in a Quenched One-Dimensional Spinor Gas," *Physical Review Letters* **110**, 165301 (2013).

[62] D. M. Stamper-Kurn and M. Ueda, "Spinor Bose gases: Explorations of symmetries, magnetism and quantum dynamics," *eprint:arXiv.org/abs/1205.1888* (2012).

[63] C. Klempt, O. Topic, G. Gebreyesus, M. Scherer, T. Henninger, P. Hyllus, W. Ertmer, L. Santos, and J. J. Arlt, "Multiresonant Spinor Dynamics in a Bose-Einstein Condensate," *Physical Review Letters* **103**, 195302 (2009).

[64] M. Scherer, B. Lucke, G. Gebreyesus, O. Topic, F. Deuretzbacher, W. Ertmer, L. Santos, J. J. Arlt, and C. Klempt, "Spontaneous Breaking of Spatial and Spin Symmetry in Spinor Condensates," *Physical Review Letters* **105**, 135302 (2010).

[65] F. Deuretzbacher, G. Gebreyesus, O. Topic, M. Scherer, B. Lucke, W. Ertmer, J. Arlt, C. Klempt, and L. Santos, "Parametric amplification of matter waves in dipolar spinor Bose-Einstein condensates," *Physical Review A* **82**, 053608 (2010).

[66] J. Kronjager, C. Becker, P. Soltan-Panahi, K. Bongs, and K. Sengstock, "Spontaneous Pattern Formation in an Antiferromagnetic Quantum Gas," *Physical Review Letters* **105**, 090402 (2010).

[67] T.-L. Ho, "Spinor Bose Condensates in Optical Traps," *Physical Review Letters* **81**, 742 (1998).

[68] T. Ohmi and K. Machida, "Bose-Einstein condensation with internal degrees of freedom in alkali atom gases," *J. Phys. Soc. Jap.* **67**, 1822 (1998).

[69] H. Saito and M. Ueda, "Spontaneous magnetization and structure formation in a spin-1 ferromagnetic Bose-Einstein condensate," *Physical Review A* **72**, 023610 (2005).

[70] D. F. Walls and G. J. Milburn, *Quantum optics*, 2nd ed. (Springer, Berlin, 2008), 2007936291 D.F. Walls, Gerard J. Milburn. ill. ; 25 cm.

[71] C. J. Pethick and H. Smith, *Bose-Einstein Condensation in Dilute Gases* (Cambridge University Press, Cambridge, 2002).

[72] P. A. Ruprecht, M. Edwards, K. Burnett, and C. W. Clark, "Probing the linear and nonlinear excitations of Bose-condensed neutral atoms in a trap," *Physical Review A* **54**, 4178 (1996).

[73] R. Barnett, A. Polkovnikov, and M. Vengalattore, "Prethermalization in quenched spinor condensates," *Physical Review A* **84**, 023606 (2011).